



HAL
open science

Drops, beads and filaments of gels under extreme deformations

Srishti Arora

► **To cite this version:**

Srishti Arora. Drops, beads and filaments of gels under extreme deformations. Soft Condensed Matter [cond-mat.soft]. Université Montpellier, 2017. English. NNT: . tel-01699078v1

HAL Id: tel-01699078

<https://hal.science/tel-01699078v1>

Submitted on 2 Feb 2018 (v1), last revised 23 Oct 2018 (v2)

HAL is a multi-disciplinary open access archive for the deposit and dissemination of scientific research documents, whether they are published or not. The documents may come from teaching and research institutions in France or abroad, or from public or private research centers.

L'archive ouverte pluridisciplinaire **HAL**, est destinée au dépôt et à la diffusion de documents scientifiques de niveau recherche, publiés ou non, émanant des établissements d'enseignement et de recherche français ou étrangers, des laboratoires publics ou privés.



THÈSE

Pour obtenir le grade de
Docteur

Délivré par l'**Université de Montpellier**

Préparée au sein de l'école doctorale Information structure systèmes
Et de l'unité de recherche Laboratoire Charles Coulomb

Spécialité : **Physique**

Présentée par **Srishti ARORA**

**Gouttes, perles et filaments de gel sous
déformations extrêmes**

Soutenue le 09/05/2017 devant le jury composé de

M. Christophe Clanet	Directeur de Recherche, CNRS	Président
M. Sébastien Manneville	Professeur, ENS Lyon	Rapporteur
M. Christian Ligoure	Professeur, Université de Montpellier	Directeur de thèse
Mme Elise Lorenceau	Directrice de Recherche, CNRS	Rapporteuse
Mme Laurence Ramos	Directrice de Recherche, CNRS	Co-directrice de thèse
M. Dimitris Vlassopoulos	Professeur, IESL-FORTH	Examineur



This thesis is dedicated to my parents and gurus.
For their love, continual support and encouragement

Acknowledgement

This thesis is a depiction of a journey well-traveled with the people who have contributed to my professional and personal growth. This would be the best platform to express my gratitude towards them.

First and Foremost, I want to thank my supervisors, Laurence Ramos and Christian Ligoure for accepting my application for the PhD three years ago. They have provided guidance at key moments during my research work while allowing me to work independently, a majority of times. I will always remember the interaction period of ours where sometimes we jumped out of excitement on discovering some phenomenal experimental results and sometimes moments of despair to explain the results quantitatively. I am very thankful to them for enriching scientific discussions that have provided the foundation of this thesis, their confidence in me and the patience they have shown during these years especially at the time of writing this thesis.

I would like to thank rapporteurs of my thesis Sébastien Manneville and Elise Lorenceau and to the members of the jury, Christophe Clanet and Dimitris Vlassopoulos for their thorough reading of my manuscript and pertinent remarks. It was my honor to present my work. I want to thank in particular Sébastien Manneville for following my research work during my PhD by participating each year in comité de suivi de thèse. Our discussions together with Laurence and Christian have certainly influenced my thesis.

I want to thank Ole Hassager, Dimitris Vlassopoulos, Ameer Louhichi and Aamir Shabbir for research collaboration which provided me the opportunity to learn and understand the subject in a more comprehensive manner.

I must thank the funding body Marie Curie Initial Training Network SUPOLEN (Supramolecular assembly of polymeric structures: a novel route to enhance soft materials properties) under the European Union Seventh Framework (Grant No. 607937) for my experimental research, collaborations and scientific exchange.

I am thankful to Serge Mora for our scientific discussions together with Laurence and Christian and especially for forwarding my PhD application to Christian three years ago. I want to thank Lucyna Firlej for helping with all the questions pertaining to the PhD program and being part of comité de suivi de thèse.

I came to this lab with absolute zero knowledge of French language and as a complete stranger but even then people of Laboratoire Charles Coulomb made my stay much easier than what I had expected. I would like to thank every member of Laboratoire Charles Coulomb who has contributed directly or indirectly to this work. I want to specially thank Adoration, Tina, Jean-Christophe, Stéphanie, and Béatrice for helping me with all the administrative formalities and always welcoming with a big smile and special thanks to Adoration for making my life on administrative fronts much easier and plus for lot of "bonbons et Chocolats".

I want to thank Raymond and Philippe for all the help pertinent to experiments. I want to thank in particular Jean-Marc Fromental and Ty Phou for helping me in the design of

experimental set-ups. They always encouraged me and provided a cordial environment to work. Thank you, Ty, for patiently answering my dumb chemistry questions.

Thanks to all the permanent members of Matière Molle team: Antonio, Gladys, Luca, Christophe, Amélie, Martin, Anne-Caroline, Julian, Laura, Matthieu, Pascale, Maurizio, Michel, and Daniel. The sweat moments were when I had to present my work in the internal seminars but it always ended up in fruitful discussions.

I would like to thank the non-permanent members of the Matière Molle team who have been a part of this 3-year odyssey in Montpellier. I want to thank Delphine who shared the office with me when I joined the lab for helping me with initial adjustments and also for always motivating me in all aspects of life. I want to thank Clara exclusively for being a dear angel. You not only helped me in my initial days of settling down in Montpellier but also helped a lot in the beginning of my research trek and have provided insightful thoughts throughout. I want to thank Rym for being a sweetheart and always there with a big smile and hug. I want to thank my special Italian squad for super Pizza treats and outings. Thanks in particular to Dafne for being there to help in translating my incredible French and for baking delicious cakes, Luca for teaching me some very interesting Italian words, Domenico for being accessible for quick scientific questions, Dario for always boosting my spirits to work and thank you, Dario, for joining "Drop Team" and Stefano for all the fun filled travel across Europe and especially for Food invites. Thanks for signaling me "wake-up" whenever I day-dreamed.

The two prime people with whom I share my office, Adrian and Yassine. Thank you for giving me often a dose of motivation, for sharing good laughs and making the environment of office always welcoming. Thanks for coping with my poor pronunciation of limited French vocabulary. Thank you, Adrian, especially for boosting my spirits before every important presentation and for keeping my morale high. Thanks Yassine for writing your thesis at the same time. It helped a lot to keep up with my determination to write. Thank you for always helping me in need.

I want to thank Celine, Cyrille, Laura, Yanick, Haifa, Maissa, Xiaolu, Valentine and Mohsen plus people who have joined the lab not so long ago, Stefano, Anthony, Angelo, Alexandre, Justine, Alexey, Benjamin, Camillo, Thibaut and Fanny for being a part of this beautiful journey of mine.

I would like to thank my SUPOLEN colleagues for being an amazing team. I enjoyed the scientific courses we did together, fine dining and lot of adventures.

I want to thank some professors back in India: Shobhana Narasimhan and Sevi Murugavel for always believing in me and supporting me in my research path and in particular to Rajesh Ganapathy along with his students Manasa and Shreyas for introducing me to the world of Soft Matter.

Finally, I would like to thank my family especially my parents for providing me more than just my genomic matter. They have always supported me in all quests. I want to thank Nayna and Siddharth for always staying a phone call away in need. I want to thank my extended family: Amit, Anjali, Chandan, Darshana, Dweepan, Preeti, Renu and Shivani for encouraging me and backing up my decisions of life. I want to thank Sumanta for endless support, love and always being there on my side.

Contents

Introduction	1
1 Motivation and State of Art	5
1.1 Freely expanding sheets	5
1.1.1 Impact dynamics of liquid drops	5
1.1.2 Impact of soft elastic beads	12
1.1.3 Impact of non-Newtonian drops	12
1.1.4 Objectives : Part I	13
1.2 Fracture in viscoelastic fluids	13
1.2.1 Fractures in shear cells	13
1.2.2 Fracture in Hele-Shaw cells	15
1.2.3 Fractures in extensional geometry	15
1.2.4 Objectives : Part II	18
2 Materials and Methods	19
2.1 Experimental systems	19
2.1.1 Self-assembled transient networks	19
2.1.2 Elastic beads	23
2.1.3 Newtonian fluids	26
2.2 Rheological methods	27
2.2.1 Shear rheological measurements	28
2.2.2 Extensional rheology measurements and imaging	32
2.2.3 Measurement of the elastic modulus of elastic beads	34
2.3 Experimental set-ups	36
2.3.1 Drop impact on a small target	36
2.3.2 Drop impact using an inverse Leidenfrost effect	38
2.4 Image analysis	40
3 Interplay between Viscosity and Elasticity in Freely Expanding Liquid Sheets	45
3.1 Experimental samples and techniques	46
3.2 Linear viscoelasticity	46
3.3 Dynamics of viscous and viscoelastic sheets	49
3.3.1 Dynamics of liquid sheets: $De \ll 1$	49
3.3.2 Dynamics of liquid sheet: $De \approx 1$ and $De \gg 1$	58
3.4 Conclusion	62

4	Unified Description of the Resilient Behavior of Elastic Beads and Liquid Drops on Impacting Surfaces	65
4.1	Experimental samples and techniques	65
4.2	Dynamics of elastic and liquid sheets	66
4.2.1	Experimental observations	66
4.2.2	Quantitative analysis	68
4.3	Conclusion	78
5	Impact of Viscoelastic Drops on Solid Surfaces	81
5.1	Experimental samples and techniques	82
5.2	Expansion of viscoelastic and Newtonian viscous sheets	82
5.2.1	Impact of viscoelastic drops using inverse Leidenfrost effect	82
5.2.2	Impact of viscoelastic drops on a small solid target	85
5.2.3	Impact of Newtonian viscous drops on a small solid target	89
5.3	Instabilities and cracks in viscoelastic sheets	91
5.4	Conclusion	97
6	Brittle Fracture of Polymer Transient Networks	101
6.1	Experimental samples and techniques	101
6.2	Linear viscoelasticity	102
6.3	Modes of rupture of the filaments	105
6.3.1	State diagram	105
6.3.2	Non-linear extensional rheology	105
6.3.3	Crack imaging	108
6.3.4	Crack opening profiles	110
6.4	Discussion	110
6.5	Conclusion	113
	General Conclusions and Perspectives	115
A	Chemical Compounds	121
B	Extensional Viscous Dissipation During the Expansion of a Liquid Sheet	123
C	An Alternative Model for the Maximal Spread Factor?	125
	Bibliography	129

Introduction

Gels consist of three-dimensional networks that span the whole volume of a liquid medium. The internal network structure results from permanent or transient bonds. In the first case the gels behave as soft solids whereas in the second case, they behave as viscoelastic fluids. Gels, because of their softness, are easy to deform hugely and eventually to fail by mechanical means.

The main objective of this thesis is to rationalize the respective roles of capillary, viscous and elastic forces in the dynamics and failure of gels submitted to equibiaxial or uniaxial deformations. Equibiaxial deformations will be realized by impacting drops or beads of gels on a solid surface and uniaxial deformation by stretching filament of gels.

The way in which a liquid drop or an elastic bead deforms during its impact on a solid surface is a ubiquitous fascinating phenomenon of daily life. It has eluded explanation for the past 20 years when high-speed video technology began to allow time-resolved observations [Josserand 2016]. Owing to the numerous environmental and industrial applications, the impact of liquid drops on solid surfaces has been studied extensively since the pioneering work of Worthington [Worthington 1908] till now [Yarin 2006, Josserand 2016]. The impact may result in the drop spreading over the solid surface, receding, splashing, rebounding, depending on the surface and interfacial tension, the roughness, and wettability of the solid surface, the drop size, the impact velocity, the properties of the liquid (its density, viscosity, viscoelasticity). However, there have been fewer studies on soft elastic beads and non-Newtonian drops and the dynamics of the impact of solid beads and liquid drops apparently share nothing in common.

Here we investigate freely expanding sheets formed by ultra-soft spherical gel beads with various elastic modulus, liquid droplets of varying surface tensions and zero shear viscosities, and viscoelastic fluids (simple Maxwell fluids) of various rheological characteristics. The sheets are produced by impacting a drop or bead on a small solid target and on a silicon wafer covered with a thin layer of liquid nitrogen. These experimental set-ups significantly suppress the interaction between the drop or bead and the solid surface. In order to tentatively unify the impact dynamics of solid, liquid or viscoelastic pearls, we will focus on two important outcomes of drop or bead impact on a solid substrate: the maximum diameter and how long the impacting object remains in contact with the solid during the shock.

On the other hand, fracture phenomenon in complex fluids are much less documented than in solids but has attracted a lot of interest in the soft matter community. The behavior of viscoelastic samples is more complex than solid ones as one may expect viscous dissipation to be enhanced and eventually dominate, yielding the sample to flow instead of break. However, when submitted to deformation rates larger than the inverse of their

slowest relaxation times, viscoelastic fluids can break as solids do, as evidenced in several works with associative polymer networks [Ligoure 2013, Huang 2017]. From a conceptual point of view, the extension of the theoretical models for the fracture of solids to viscoelastic liquids, and the definition of brittleness and ductility of solids for viscoelastic liquids are not trivial. Filament stretching rheometry [McKinley 2002] appears as an exquisite tool to investigate the fracture of viscoelastic fluids, since it allows a sample to be submitted to a prescribed and constant extensional rate. Filament stretching rheometry was successfully used to measure the tensile stress of associative polymer networks and worm-like micelles before fracture [Rothstein 2003, Bhardwaj 2007, Tripathi 2006]. A substantial improvement has been recently achieved by coupling filament stretching rheometry to a fast imaging of the filament allowing not only to visualize but also to quantify the crack nucleation and propagation [Huang 2016a]. We use filament stretching rheometry coupled to fast imaging to investigate the fracture processes of self-assembled transient networks to investigate the crucial role of non-linear viscoelasticity in the fracture of transient networks.

The manuscript is divided into six chapters, presented as follows:

Chapter 1 is a bibliographic chapter that presents the state of the art on the topics. We describe experimental techniques used to impose an external deformation. The chapter is broadly divided into two sections: the first section details the dynamics of freely expanding sheets produced by liquid drops, soft elastic beads and non-Newtonian drops on impacting different kinds of surfaces. The second section aims to describe the fracture of viscoelastic fluids especially of transient networks in different experimental configurations, with a particular emphasis on uniaxial extensional geometry.

Chapter 2 is dedicated to the description of the different experimental systems that are used in this work. We describe the rheological methods used to characterize the samples and the experimental set-ups that have been developed during the course of this thesis to study the impact dynamics of drops and beads. We finally describe the methods used to analyze the images that are obtained from the fast camera.

Chapter 3 describes the dynamics of freely expanding sheets prepared with viscous and viscoelastic fluids. The sheets are produced by impacting on a small solid target. We present the linear rheology of the self-transient networks. We then describe and quantify how sheets made of viscous and viscoelastic materials expand depending in particular on the ratio between the intrinsic relaxation time of the viscoelastic samples and the typical experimental time. We provide a model for the dynamics of viscous sheets and show that shear dissipation occurs on the surface of the small target. We finally discuss the results for viscoelastic samples.

Chapter 4 focuses on the dynamics of a freely expanding sheet formed by soft elastic beads and liquid drops. The sheets are produced by impacting on a solid substrate covered with thin layer liquid nitrogen. We first give a brief account on the used experimental samples and techniques. We provide qualitative and quantitative descriptions of the

maximum expansion and dynamics of expansion of soft elastic beads and liquid drops. We then present a universal scaling law to rationalize the maximum expansion, the contact time and the dynamics of the sheets, which can be understood in terms of simple harmonic motion without viscous dissipation.

Chapter 5 aims to characterize and understand the expansion of viscoelastic drops and Newtonian drops when they impact a small solid target or a solid surface covered with a layer of liquid nitrogen. We show that the same scaling law for maximum expansion derived in the previous chapter is valid for viscoelastic samples in the absence of viscous dissipation. In the case of viscous liquids and viscoelastic fluids, we introduce and measure an effective impact velocity to quantitatively account for the maximum expansion of the expanding sheet. We finally characterize in detail the instabilities and cracks observed in viscoelastic sheets.

Chapter 6 is dedicated to study the uniaxial extensional deformation of reversible double transient polymer networks. After a brief description of the experimental samples and methods, we present the shear and extensional rheology of the polymer networks. The modes of extensional deformation up to a maximum strain are then described. We focus on the cracks that occur when the samples are strained at a sufficiently high strain rate and characterize their opening profiles and propagation velocity. Finally, we discuss the correlation between the extensional rheology and the crack opening profiles, in light of the literature and of the specificity of our samples.

We present at the end general conclusions and perspectives of our work.

Motivation and State of Art

Contents

1.1	Freely expanding sheets	5
1.1.1	Impact dynamics of liquid drops	5
1.1.2	Impact of soft elastic beads	12
1.1.3	Impact of non-Newtonian drops	12
1.1.4	Objectives : Part I	13
1.2	Fracture in viscoelastic fluids	13
1.2.1	Fractures in shear cells	13
1.2.2	Fracture in Hele-Shaw cells	15
1.2.3	Fractures in extensional geometry	15
1.2.4	Objectives : Part II	18

In this chapter, we describe some experimental techniques that have been used in the literature to impose extensional deformations. In the first part, we focus on freely expanding sheets produced by the impact of Newtonian and non-Newtonian liquid drops, and soft elastic beads on different kinds of solid surfaces. We mainly restrict our review to the maximal spread factor of the sheets. In the second part, we describe different experimental configurations used to study the behavior of complex fluids, especially transient networks, undergoing large deformations, and focus primarily on uniaxial extensional deformations of viscoelastic fluids.

1.1 Freely expanding sheets

In this part, we describe different experimental set-ups that have been employed to study the impact dynamics of the sheet.

1.1.1 Impact dynamics of liquid drops

The dynamics of drop impact is a century old problem, which is still evolving in understanding thanks to the technological advances in the high-speed video technology

that allows time resolved observations [Thoroddsen 2008]. A.M. Worthington was one of the first pioneers to study drop and solid ball impacts on deep liquid pools with his investigations published in the book "A study of splashes" [Worthington 1908]. There are many environmental and industrial applications including spray coating, pesticide application, ink-jet printing, bioarray design and so on. The outcome of the impact of a drop onto a surface can be influenced by many factors, for instance, the nature of the surface, the size of the drop, the physical properties of the liquid (density, surface tension, viscosity, viscoelasticity), the impact velocity and the surrounding gas. Upon hitting a solid surface, a drop can splash, partially or fully rebound, or remain on the surface and spread [Rioboo 2001].

The impact dynamics of Newtonian fluids on a solid substrate has been recently reviewed by C. Josserand *et al* [Josserand 2016] and earlier works have also been covered in a review by A.L. Yarin [Yarin 2006] who discusses the impact of liquid drops on solid and liquid surfaces.

1.1.1a Impact of drops on solid surfaces

When a drop impacts a solid surface, the inertial forces cause the drop to expand radially. During the expansion, the kinetic energy is partially converted into surface energy. Once it reaches the maximum expansion the stored surface energy causes the expanded sheet to retract back to the primal state. Two important dimensionless parameters are used to describe the drop impact which balance the inertia with viscous forces, the Reynolds number, $Re = v_o d_o \rho / \eta_0$ and inertia with capillary forces, the Weber number $We = \rho d_o v_o^2 / \gamma$. Here v_o is the impact velocity, d_o is the drop diameter, ρ is the density of the liquid, η_0 is the dynamical viscosity and γ is the surface tension of the liquid. R. Rioboo *et al* [Rioboo 2001] categorized the outcome of the impact of drop on various solid surfaces into six main categories. Figure 1.1 shows the images of drop impact for each category [Rioboo 2001].

At small impact velocity, the drop spreads on the substrate and stays, known as deposition. The prompt splash results from a high impact velocity and gives rise to ejection of small droplets from the rim of the sheet at the spread contact line. If the surface tension is reduced, then the impact results in corona splash in which a thin liquid sheet forms a bowl-like structure that subsequently ejects small droplets. During the receding break-up stage, lamella may break up into fingers and result in ejection of secondary droplets due to capillary instability. If the kinetic energy is not too much dissipated and surface energy is sufficiently large, then the receded drop may result in partial or complete rebound. The maximal extension reached by the impinging drop when it spreads on the surface is one of the important parameters that has been examined extensively. It will be discussed in the next section.

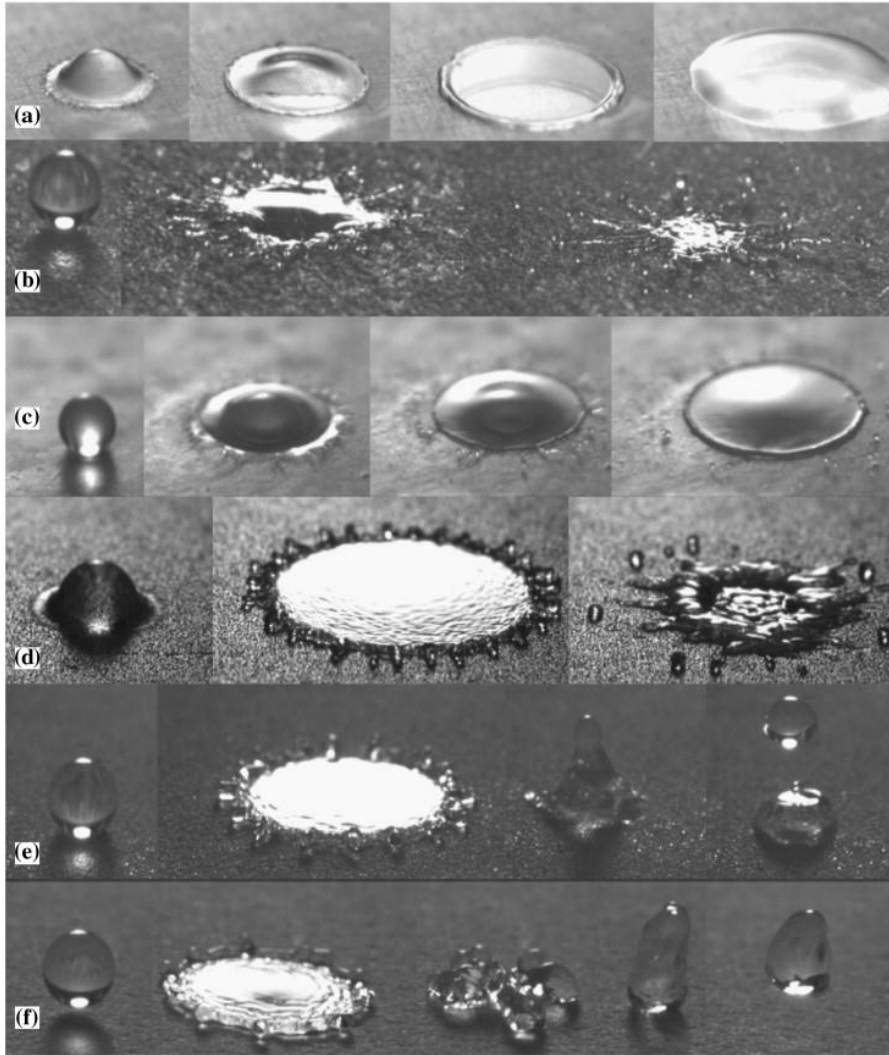


Figure 1.1: Snapshots of images at different time instants for the impact of a liquid drop on various solid substrates (a) deposition (b) prompt splash (c) corona splash (d) receding break-up (e) partial rebound and (f) rebound [Rioboo 2001].

Maximal spread factor: When a drop impacts on a smooth solid surface, the dynamics of the sheet is governed by at least three competitive forces, inertia, capillary forces, and viscous forces [Pasandideh-Fard 1996, Aziz 2000]. The maximal extension reached by the impinging drop when it spreads on the surface is expressed as the maximal spread factor $\lambda = d_{\max}/d_o$, here d_{\max} is the maximum diameter of the sheet and d_o is the initial drop diameter. Most of the scaling laws that have been proposed concern Newtonian fluids and distinguish two regimes: (i) a viscous regime in which λ is determined by balancing the kinetic energy and viscous dissipation leading to $\lambda \sim Re^{1/5}$ [Chandra 1991, Rein 1993] and (ii) inertial regime where λ is obtained by a balance between kinetic energy and surface energy (at maximum deformation) giving $\lambda = We^{1/2}$. There are many scaling laws that have been proposed to explain the spreading factor inclusive of viscous dissipation.

Table 1.1 shows commonly used scaling laws to fit the experimental data.

References	Empirical model
[Scheller 1995]	$\lambda \sim 0.61Re^{1/5}(WeRe^{-2/5})^{1/6}$
[Pasandideh-Fard 1996]	$\lambda = \sqrt{\frac{We + 12}{3(1 - \cos\theta) + 4(We/\sqrt{Re})}}$
[Roisman 2009]	$\lambda \sim 0.87Re^{1/5} - 0.4Re^{2/5}We^{-1/2}$

Table 1.1: Different scaling laws proposed in the literature to account for the maximal spread factor [Josserand 2016]. Here Re is the Reynolds number, We is the weber number and θ is the contact angle.

1.1.1b Impact of liquid drops on solid surfaces under minimized dissipation conditions

Small solid target

There has been constant evolvment in the experimental set-ups to limit the effect of viscous dissipation. M. Vignes-Adler *et al* [Rozhkov 2002, Rozhkov 2004] studied the impact of drops on small cylindrical targets of diameter comparable to the size of the droplets. Using this experimental set-up, the spreading sheet is freed from shear dissipation when it leaves the target. When the drop hits the target, it radially expands freely in air and retracts back under the action of surface tension. We note that this configuration is the discrete version of the Savart experiment, where a liquid jet hits normally a flat solid disk, resulting in a stationary planar liquid sheet [Savart 1833]. Figure 1.2a schematically shows the expanded sheet produced by the impact of a drop on a solid target and time series of the expansion and retraction of the sheet is shown in Figure 1.2b. Interestingly, the ejection angle of the sheet can be controlled by incorporating a coaxial cylinder [Villermaux 2011]. Recently, C. Vernay *et al* [Vernay 2015c] proposed a simple experimental technique to access the thickness field of the expanding sheet thanks to time and space-resolved measurement of the absorbance of the sheet.

Superhydrophobic surfaces

Another way to reduce the dissipation due to the interaction of the liquid drop with the solid surface is to use super-hydrophobic surfaces (SHS). In this case, the contact between the liquid drop and the solid substrate is only partial due to the presence of air pockets that prevent full surface wetting and eliminate the contact angle hysteresis. Hysteresis occurs due to the surface defects that cause energy loss. SHS have been used in

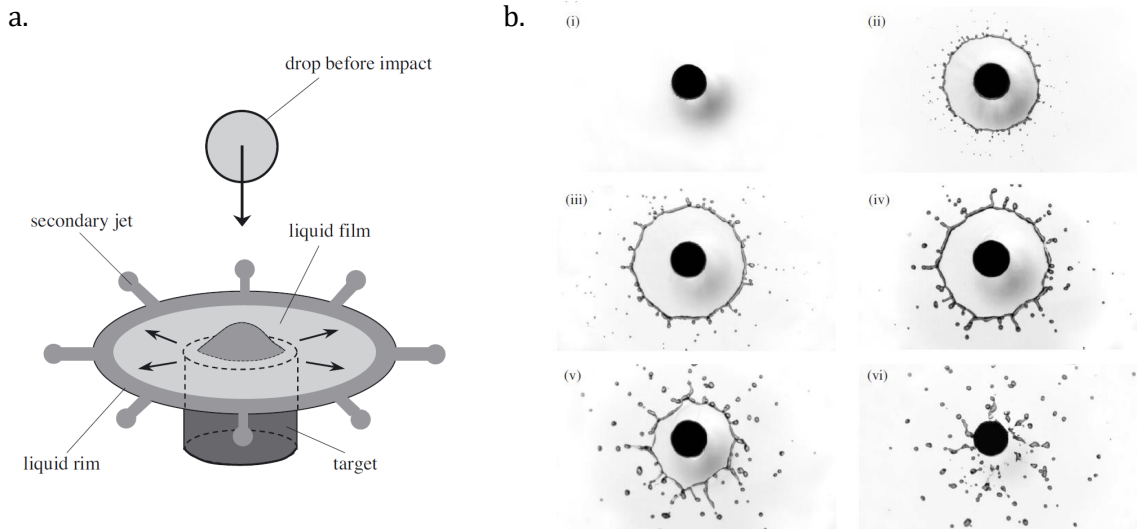


Figure 1.2: (a) Scheme of small solid target experimental set-up. (b) Time series of the formation of the sheet. Time interval between images is 1 ms. The scale bar is set by the black solid disc of 4 mm [Rozhkov 2004].

many experiments to study the impact of drops [Richard 2002, Okumura 2003, Luu 2009, An 2012, Luu 2013]. For instance D. Richard *et al* [Richard 2000] used SHS with a contact angle of 170° to study the drop impact. They found a coefficient of restitution close to 0.9 for rebounding liquid drops. However, A.L. Biance *et al* [Biance 2006] showed that even with high contact angles (typically 160°), adhesion occurs at low velocities which induce energy loss. Impact velocity can set the criteria for the super-hydrophobicity: the smaller is the velocity at which rebound occurs the more efficient would be SHS.

Superheated surfaces

Rebound of liquid drops is facilitated even by elevating the temperature (T) of the substrate i.e. above the Leidenfrost temperature. In Leidenfrost condition, the drop hovers on the surface due to the formation of gaseous vapor cushion from the droplet that thermally insulates the drop [Chandra 1991, Rein 2002]. A systematic study has been performed by T. Tran *et al* and V. Bertola [Tran 2012, Bertola 2015] where the authors investigated the (We, T) phase space to study the outcome of drop impact. They showed that there is a gentle film boiling regime where the expanded sheet is supported by a thick vapor layer to prevent any contact between the liquid lamella and the solid surface. T. Tran *et al* also provided the measurement for the thickness of this vapor layer in the gentle film boiling regime and found that it is one order of magnitude thinner than the thickness of the vapor layer in static regime [Biance 2003]. More recently, H. Lastakowski *et al* [Lastakowski 2014] performed experiments in the scenario of zero viscous coupling thanks to the formation of a vapor layer between the liquid and solid surface and measured the flow field and local thickness profiles of an expanding sheet.

Sublimating surfaces

C. Antonini *et al* [Antonini 2013] compared the outcome of drop impact on three different repellent solid surfaces a). very hot plate (Leidenfrost effect) b). SHS and c). sublimating surface as shown in Figure 1.3 (left). They showed that nonwetting and slip condition can also be achieved in the case of very cold substrates such as dry ice (solid carbon dioxide). Similarly to the Leidenfrost effect when the drop at ambient temperature impacts dry ice, a vapor layer of carbon dioxide forms in between the drop film and the substrate that thermally insulates the droplet and also inhibits the interaction between the substrate and the droplet. The authors also measured the rebound time and maximal spread factor for three types of modified surfaces (SHS, superheated and sublimating surfaces) which will be discussed in later sections.

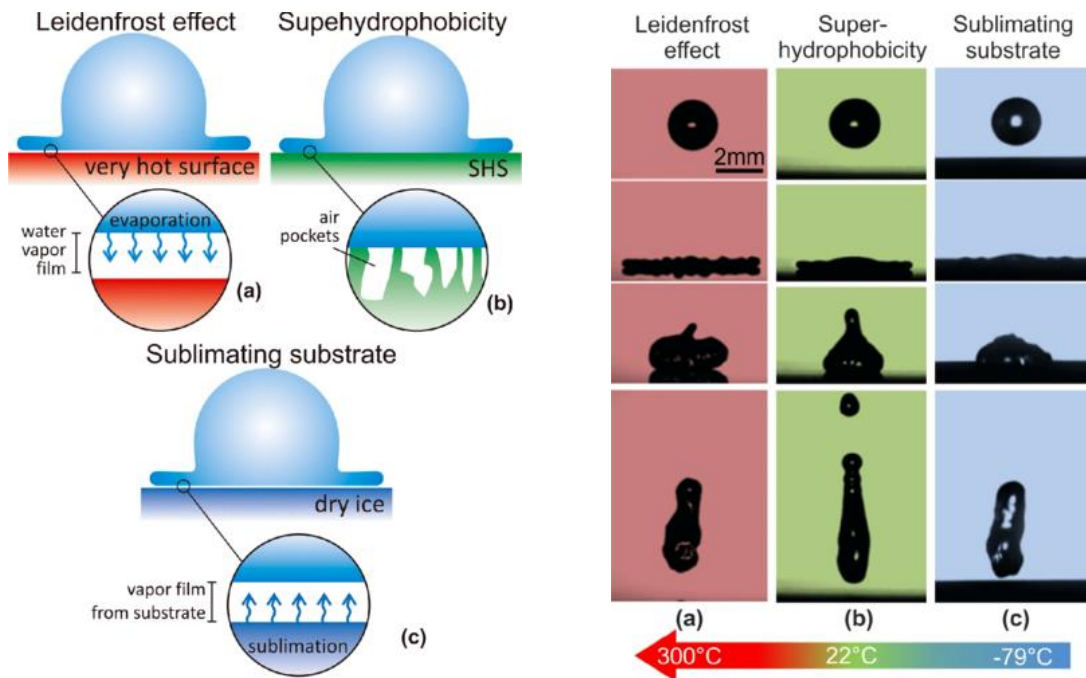


Figure 1.3: Scheme to show the drop interaction with different repellent solid surfaces (left). Dynamics of the sheet on three different substrates as mentioned (right) [Antonini 2013].

Maximal spread factor: In the case of a SHS where the shear dissipation is expected to be negligible and at high We for which no splash is present, C. Clanet *et al* [Clanet 2004] developed a model to predict the maximal spread factor λ . They use mass conservation based on the pancake thickness which is governed by the capillary wave created by the impact. This model yields $\lambda \sim We^{1/4}$ instead of $We^{1/2}$ scaling obtained

from classical arguments based on energy conservation. This scaling has been successfully adopted to interpret experimental studies [Biance 2006, Tsai 2011, Guémas 2012]. However, C. Josserand *et al* [Josserand 2016] claimed that the correction due to initial radius of the drop should be considered at low We . C. Antonini *et al* [Antonini 2013] on the other hand compared the impact of liquid drop for three different surfaces a) a very hot plate (Leidenfrost effect) b). a SHS and c). a sublimating surface. The authors found that $\lambda \sim We^{0.4}$, an exponent close to $1/2$, which can be explained by considering a simple balance between kinetic energy and surface energy (Figure 1.4). This is also shown by T. Tran *et al* [Tran 2012] for the case of drop impact on superheated surfaces. The authors claimed that this could be due to the vapor layer that is shooting radially outwards and might give an extra driving force for liquid spread.

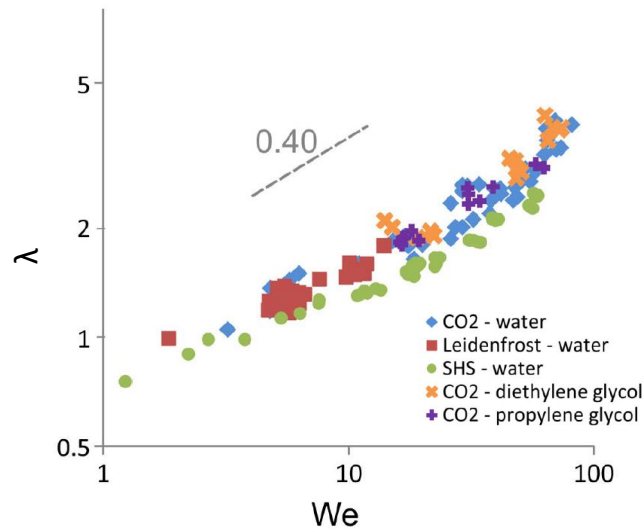


Figure 1.4: Maximal spread factor as a function of We and the experimental fit of the data yields $d_{\max}/d_o = We^{0.4}$ adapted from [Antonini 2013].

Contact time: Another interesting parameter to measure in the impact dynamics of a drop is rebound time also known as contact time τ_c . D. Richard *et al* [Richard 2002] studied the impact of a water drop on a SHS and showed that the contact time increases linearly with the drop size but stays constant for impact velocity varying between 20 cm/s and 230 cm/s. τ_c follows a simple scaling law obtained by balancing inertia and capillarity: $\tau \sim (\rho d_o^3 / 8\gamma)^{1/2}$, also observed earlier by L.H.J. Wachters *et al* [Wachters 1966]. However, the contact time increases at small velocities [Okumura 2003]. A similar scaling for τ_c has also been observed by C. Antonini *et al* [Antonini 2013] for the impact of water drop on the three types of repellent surfaces (SHS, superheated and sublimating surface). Interestingly, J.C. Bird *et al* [Bird 2013] showed that this contact time can be reduced by using macro textured surfaces.

1.1.2 Impact of soft elastic beads

Since the pioneering work by H. Hertz [Hertz 1881], the impact of elastic solid beads on solid surfaces has attracted less attention than the impact of liquid drops. Y. Tanaka *et al* [Tanaka 2003, Tanaka 2005] impacted soft spherical gel balls of centimeter size with Young's modulus on the order of 10^4 Pa on an aluminum plate in non-stick conditions. Figure 1.5 shows snapshots at maximum deformation for beads with different elastic moduli and at different impact velocities. They observed three different regimes of impact depending on the elasticity and the impact velocity: (i) a hertz regime for small impact velocity (ii) a quasi-ellipsoidal regime for intermediate velocities and (iii) a pancake regime for high velocities. The authors measured the rebound time and maximal spread factor for different impact velocities and showed that the dynamics of spreading solely depends on a balance between the inertia and bulk elastic forces, characterized by the Mach number M . They gave a simple scaling theory to predict the λ . They showed that for large velocities $\lambda \sim M$ and for small velocities $\lambda \sim M^{8/5}$. Here M is the Mach number defined as $M = v_o/U_S$, with v_o is the impact velocity, $U_S = \sqrt{G_0/\rho}$ the velocity of transverse sound waves (G_0 the shear plateau modulus and ρ the density). Y. Tanaka [Tanaka 2005] also proposed a model that assumes a uniform deformation to explain the value of the contact time by incorporating different fitting parameters.

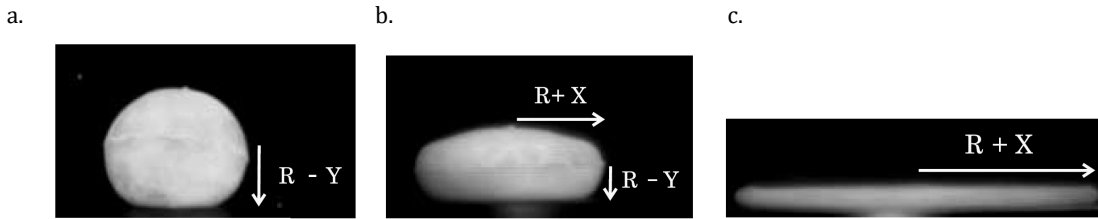


Figure 1.5: Maximum deformation of gel ball for different impact velocities v_o and elastic modulus G_0 (a) $G_0 = 27$ kPa, $v_o \lesssim 0.4$ m/s (b) $G_0 = 12$ kPa, $v_o = 2$ m/s and (c) $G_0 = 12$ kPa, $v_o = 7$ m/s [Tanaka 2003].

1.1.3 Impact of non-Newtonian drops

The impact of drops of non-Newtonian liquids has also been less explored. S. Chen *et al* [Chen 2016] studied drops of yield stress fluids (Carbopol) on a superheated surface and found a scaling law, $\lambda \sim We^{0.3}$, close to the one predicted by C. Clanet *et al* [Clanet 2004]. Yield-stress fluids have also been studied by L.H. Luu [Luu 2009, Luu 2013]. The authors investigated the impact of Carbopol drops on smooth glass surfaces and rough hydrophobic surfaces. They found that for smooth glass substrate $\lambda \sim M^{1/3}$ and for a small solid target (perfect slip condition) $\lambda \sim M$. Similar experiments have been performed by M. Guémas *et al* [Guémas 2012] for two systems: Carbopol and cornstarch. They found the

same scaling as the one of [Luu 2013] for Carbopol impacting smooth partially wetting surfaces. By contrast for cornstarch drops impacting SHS, the maximal spread factor followed the same scaling law as the one found for Newtonian fluids [Clanet 2004].

1.1.4 Objectives : Part I

We have seen that different experimental configurations have been used so far to study the impact of liquid drops, elastic beads, and viscoelastic drops, yet the field is not exhaustive. In this work, we will investigate the dynamics of freely expanding sheets prepared with (i) Newtonian fluids whose viscosity can be varied over a large range, (ii) self-assembled transient networks that behave as pure Maxwell fluids whose characteristic elastic modulus and relaxation time can be finely tuned allowing one to independently study the role of viscosity and elasticity in the impact dynamics of viscoelastic sheets, and (iii) permanent crosslinked polyacrylamide elastic gel beads. The sheets are produced by impacting a drop or bead on a small solid target of size comparable to that of a drop and on a solid surface covered with liquid nitrogen which can be considered as a repulsive surface. These experimental conditions provide us different ways to explore diverse behavior of viscous fluids, viscoelastic fluids, and elastic gels.

1.2 Fracture in viscoelastic fluids

The ability of viscoelastic materials to fracture is less documented than for solid materials. The behavior of viscoelastic samples is more complex as one may expect viscous dissipation to be enhanced and eventually dominate, thereby causing the sample to flow instead of break. However, when submitted to deformation rates larger than the inverse of their slowest relaxation times, viscoelastic fluids can break as solids. Moreover, from an experimental point of view, because viscoelastic samples flow, standard tools to investigate the fracture of solids cannot generally be used. Novel geometries have therefore been considered to investigate fracture processes in viscoelastic fluids, using a shear cell, a Hele-Shaw cell, extensional flow experimental configurations. A comprehensive review on fractures in transient networks (viscoelastic system) is provided by C. Ligoure *et al* [Ligoure 2013].

1.2.1 Fractures in shear cells

We consider here a transient network, with a characteristic relaxation time τ , subjected to a constant shear rate $\dot{\gamma}$. As $\dot{\gamma}$ is applied to the sample, the shear stress first increases linearly with $\dot{\gamma}$ but above a critical shear rate $\dot{\gamma} \sim \tau^{-1}$, the flow curve is found to exhibit a sudden stochastic drop (Figure 1.6a [Tabuteau 2009]). F. Molino *et al* [Molino 1999] were the first to propose that the sudden drop in the shear stress may be

linked to fracture propagation in transient networks. J.F. Berret *et al* [Berret 2001] gave an experimental evidence of shear-induced fractures in polymeric networks thanks to a flow visualization technique using a plate-plate transparent shearing cell. They showed that, for a low deformation field, the velocity field decreases linearly from the rotating wall to the stationary one. The flow becomes inhomogeneous above a certain shear rate that marks the onset of fracture. Similar results have been shown by P.J. Skrzyszewska *et al* [Skrzyszewska 2010] by using particle image velocimetry. The authors also observed that the shape of the crack is irregular and the width of the fracture zone increases with increasing the shear rate. The fracture zone can occur anywhere in the gap and is different for every experiment. H. Tabuteau *et al* [Tabuteau 2009] made a direct optical observation of the shear-induced fractures in transient networks comprising of microemulsion bridged by telechelic polymers. Figure 1.6b shows the growth of a crack tilted at 45° from the shear plane. The authors observed that at a critical shear rate normal stress difference σ_N is larger than σ indicating tensile stress may trigger the crack rather than shear stress.

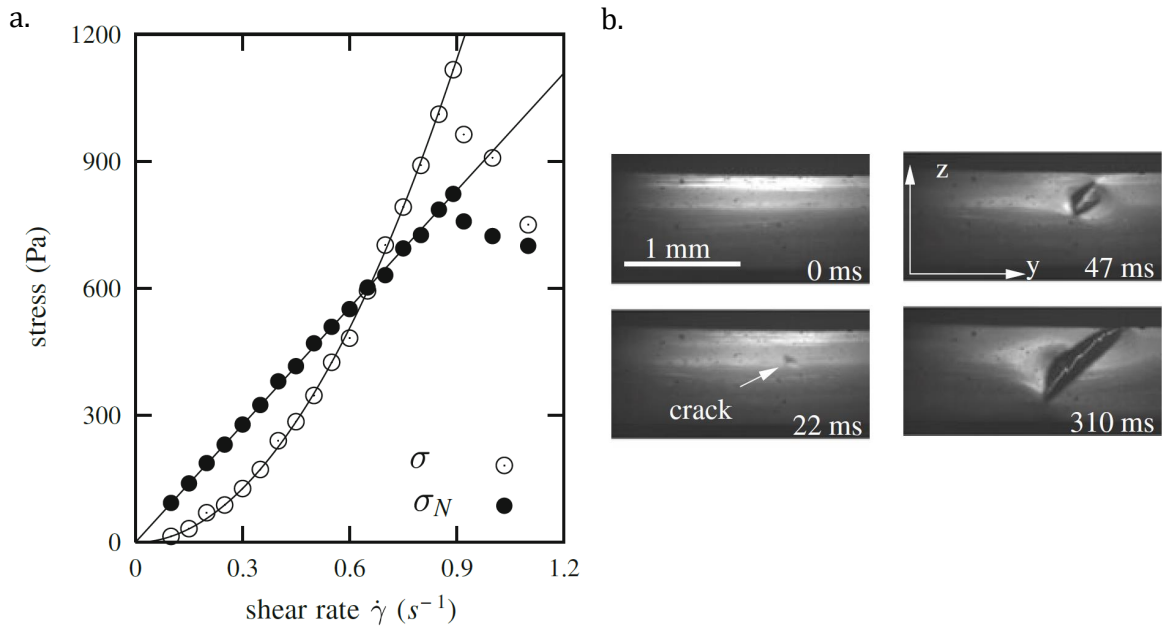


Figure 1.6: (a) Shear stress (σ) and first normal stress difference σ_N as a function of the shear rate $\dot{\gamma}$ for a transient network (with a shear modulus $G_0 = 1210$ Pa and $\tau = 0.8$ s). (b) Growth of a crack in a shear cell at a shear rate $\dot{\gamma} = 0.9 s^{-1}$. [Tabuteau 2009].

P.J. Skrzyszewska *et al* [Skrzyszewska 2010] showed another approach to observe fracture process by performing creep experiment where a constant stress is applied and the time evolution of resulting deformation is measured. They found that fracture occurs immediately when the applied stress is above a critical stress $\sigma \sim G_0$. For stresses below the critical stress, the fracture is delayed and this delay time is not well defined but

varies from one experiment to another demonstrating the stochastic nature of fracture phenomenon.

1.2.2 Fracture in Hele-Shaw cells

Saffman-Taylor instabilities arise when a low viscous fluid pushes a more viscous fluid that is confined between two closely spaced parallel plates (Hele-Shaw cell) [Saffman 1958]. The interface between the two fluids develops a hydrodynamic instability, called a viscous fingering instability. More complex behavior may occur when one or the two fluids are non-Newtonian liquids. For instance, fracture-like pattern instabilities can be observed in circular Hele-Shaw cells when a fluid is injected into a thin cell containing a transient gel. H. Zhao *et al* [Zhao 1993] showed the fingering to fracturing transition in associative polymers using Hele-Shaw cell at different injection rates (Figure 1.7a). The authors observed that there exists a critical injection rate above which fracture instabilities are observed and below which viscous fingers are observed. Dynamic fracture-like flow instabilities of associating polymeric solutions have also been studied using rectangular Hele-Shaw cell by measuring the crack tip velocity [Ignes-Mullol 1995] and correlating the tip velocity to the pressure gradient [Vlad 1999]. S. Mora *et al* [Mora 2010a, Mora 2012] revisited theoretically and experimentally the Saffman-Taylor instability for a model of viscoelastic fluids i.e. upper-convected Maxwell model. The authors showed that the fracture-like patterns results from the elasticity of the complex fluid and take place in the linear regime. Recently, G. Foyart *et al* [Foyart 2013] studied the morphology and velocity flow field in the vicinity of the interface of a finger instability and of a crack tip using image correlation velocimetry (Figure 1.7b) in a radial Hele-Shaw cell for transient gels and provided quantitative arguments to discriminate a finger from a crack. In another study [Foyart 2016] they investigated fracture process in double transient networks and quantified the rearrangement process zone around the crack tips thanks to birefringence measurements.

1.2.3 Fractures in extensional geometry

By pulling a viscoelastic fluid column sufficiently rapidly, one can observe fracture in the filament depending on the time scale of observation. Fracture in polymeric liquids has been recently reviewed by Q. Huang [Huang 2017].

A. Tripathi *et al* [Tripathi 2006] studied non-linear rheology of associative polymers using a filament stretching rheometer. A sample of initial length L_o is filled in the gap between two circular plates. The end plates then can move apart to a final separation with an exponentially increasing profile given as $L(t) = L_o \exp(\dot{\epsilon}t)$. Here, $\dot{\epsilon}$ is the strain rate. The author measured the evolution of tensile force and mid-filament diameter at the same time. They observed for low concentration of polymer and at high strain rates $\dot{\epsilon}$ that rupture of the filament occurred and followed by an oscillatory damping elastic recoil

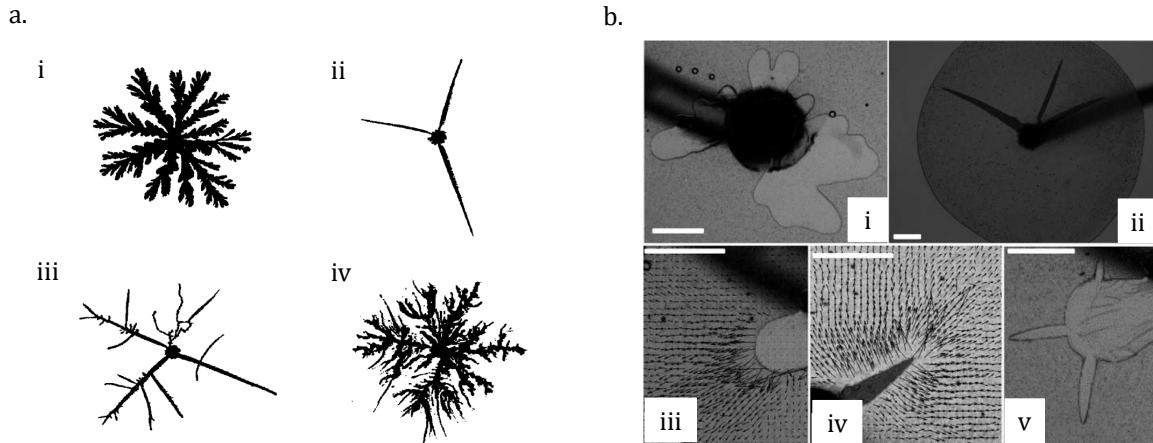


Figure 1.7: Images showing the transition from finger to fracture-like pattern in self-assembled networks confined in Hele-Shaw cells. (a) Images of the instabilities developed when dyed water is pushed in the viscoelastic gel at different injection rates [Zhao 1993]. (b) Fingering (low injection rate (i)) to fracture transition (high injection rate (ii)) for a transient gel and zoomed image of the oil/gel interface for (iii) low injection rate (iv) high injection rate and (v) a jump from low to high rate is performed (v). The arrows in (iii) and (iv) show the displacement field in the gel, as determined by image correlation velocimetry. The scale bars are 6 mm [Foyart 2013].

of the two pieces of the samples (as shown in Figure 1.8). For low strain rates, the filament did not rupture, but instead, it pinched off through viscopillary or elastocapillary thinning after a considerable necking of the filament. Rupture of filaments of viscoelastic fluids has been observed by different authors [Rothstein 2003, Bhardwaj 2007].

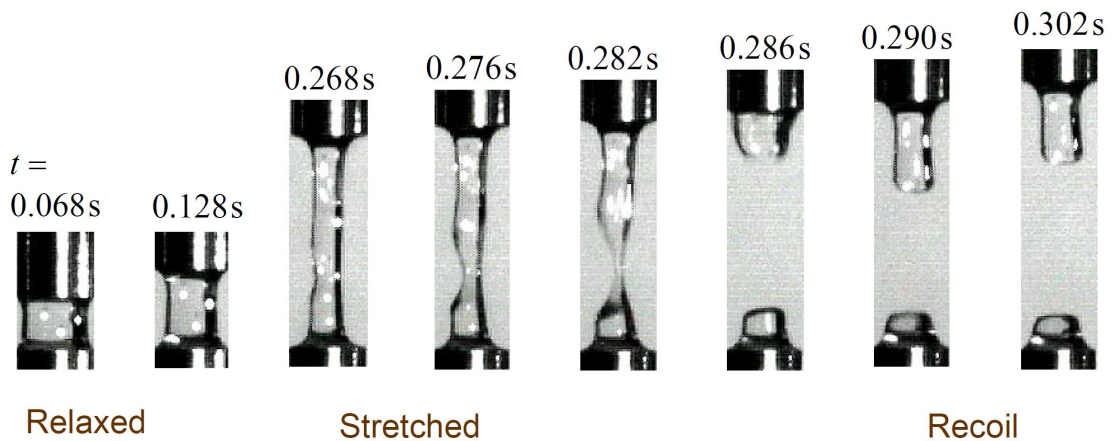


Figure 1.8: Time series of the rupture of a filament of gel stretched at a strain rate $\dot{\epsilon} = 3 \text{ s}^{-1}$ [Tripathi 2006].

The propagation of a crack in a millimeter filament occurs very rapidly and thus need

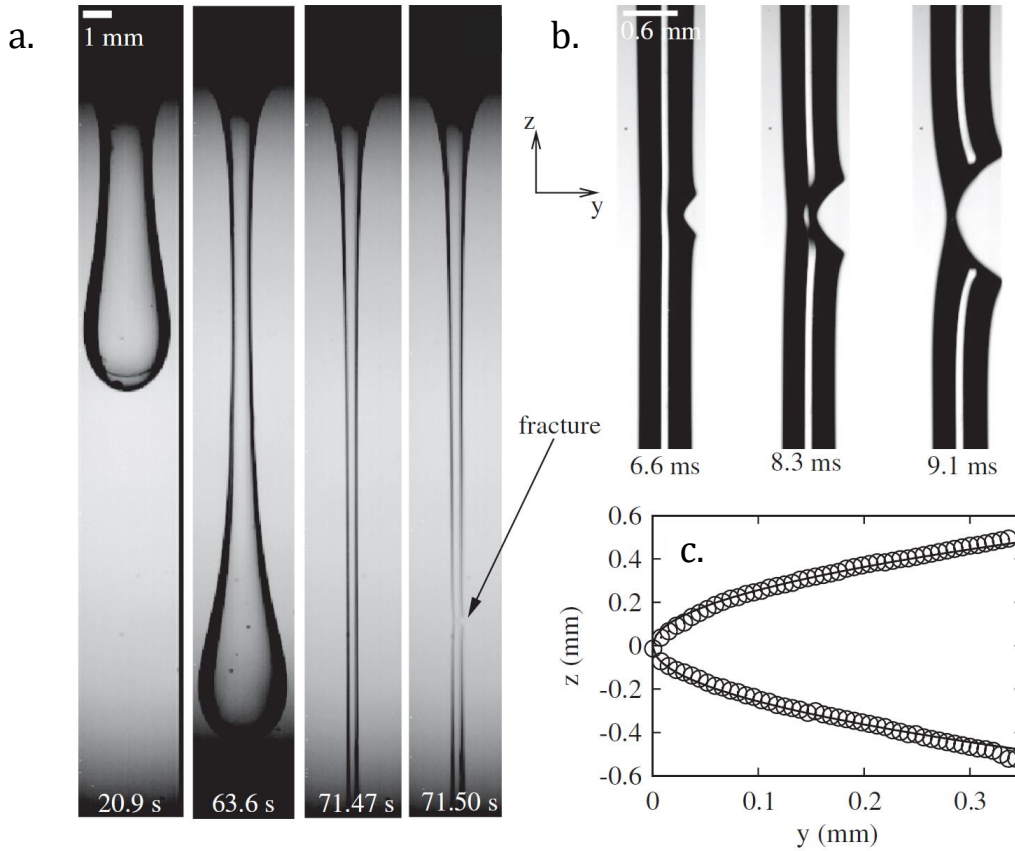


Figure 1.9: (a) Sequence of images of the fall of a drop under gravity of a transient network, (b) Zoomed images of the fracture that propagates across the sample, and (c) Typical parabolic profile of the crack tip corresponding to images in (b). The black solid line is a parabolic fit [Tabuteau 2009].

fast imaging to obtain time-resolved observations. With the advancement in high-speed video technology, it is now easier to image the propagation of cracks in a filament. H. Tabuteau [Tabuteau 2009, Tabuteau 2011] observed fracture in viscoelastic fluids using very simple experimental configuration: a so-called pendant drop experiment. A millimeter size drop falls under its own weight forming a filament behind until a crack nucleates in the filament that propagates perpendicular to it (Figure 1.9). The authors showed that the fracture is purely elastic and reversible without any significant interfacial and bulk viscous dissipation. However, they showed hyperelastic corrections have to be taken into account for quantitative analysis of the crack profiles owing to the low elastic modulus of the complex fluids under consideration.

In a controlled filament stretching configuration, Q. Huang *et al* [Huang 2016b] coupled high-speed videography with an extensional rheometer. They performed a uniaxial extension of polymeric liquid filaments. They observed multiple cracks that occur by an

edge fracture that propagates perpendicular to the axes of filament thus breaking the axis symmetry as shown in Figure 1.10. They showed that the fracture profile close to the crack tip has a parabolic shape with a width z that scales as $x^{1/2}$ (where x is the distance from the crack tip) as expected for an elastic material, and further away the profile is fitted by $z \sim x^{3/2}$ in agreement with viscoelastic trumpet model of de Gennes [De Gennes 1996, Saulnier 2004]. Similarly, in an another recent experiment A. Shabbir *et al* [Shabbir 2016] showed a fully elastic crack propagation in an associative polymer filament demonstrated by a parabolic profile throughout the crack.

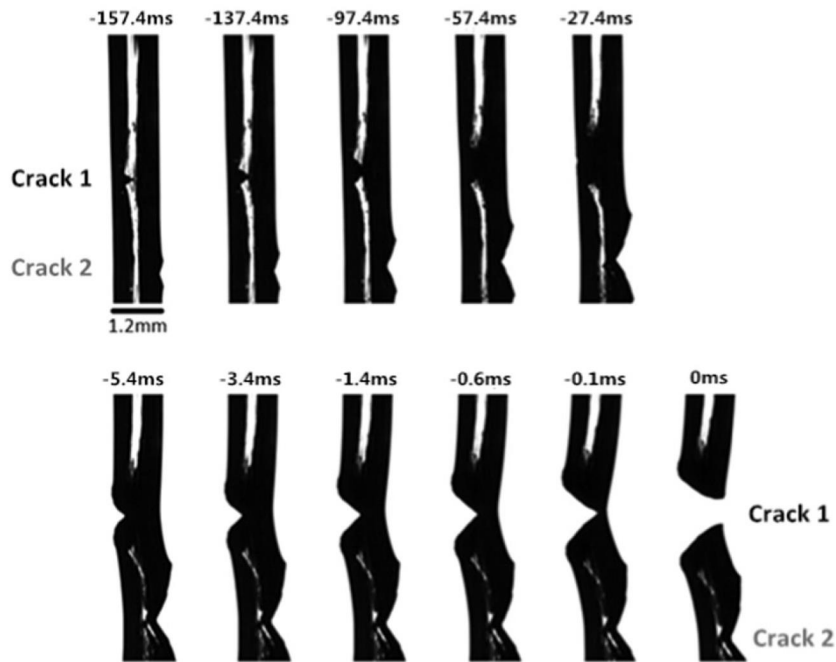


Figure 1.10: Time series of images of cracks propagating in a filament undergoing a uniaxial extensional flow [Huang 2016b].

1.2.4 Objectives : Part II

With the coupling of a fast camera and an extensional rheometer, we will study the extensional rheology and the rupture of double transient networks undergoing uniaxial stretching. Our aim is to investigate the role of the sample structure on the process at play.

Materials and Methods

Contents

2.1	Experimental systems	19
2.1.1	Self-assembled transient networks	19
2.1.2	Elastic beads	23
2.1.3	Newtonian fluids	26
2.2	Rheological methods	27
2.2.1	Shear rheological measurements	28
2.2.2	Extensional rheology measurements and imaging	32
2.2.3	Measurement of the elastic modulus of elastic beads	34
2.3	Experimental set-ups	36
2.3.1	Drop impact on a small target	36
2.3.2	Drop impact using an inverse Leidenfrost effect	38
2.4	Image analysis	40

This chapter focuses on the experimental samples used. Methods and set-ups employed to characterize the samples.

2.1 Experimental systems

Note: Appendix A contains the information for all the chemical constituents used for the preparation of all samples.

2.1.1 Self-assembled transient networks

Complex materials that can spontaneously form three-dimensional networks in a solvent and are able to transiently transmit elastic forces over macroscopic distance are known as self-assembled transient networks. These networks consist of reversibly cross-linked polymers. They exhibit simple rheological properties and are even able to fracture [Ligoure 2013]. We have worked with two classes of self-assembled transient network:

surfactant micelles and surfactant-stabilized oil droplets (microemulsions) suspended in water and reversibly linked by home-synthesized triblock telechelic polymers.

A telechelic polymer has a poly(ethylene oxide)(PEO) hydrophilic backbone with hydrophobic aliphatic chains grafted at both ends, C_nH_{2n+1} , where $n = 12, 18$ or 23 . The weight of the PEO block is $10,000 \text{ gmol}^{-1}$ or $35,000 \text{ gmol}^{-1}$. Using NMR, the degree of substitution of hydroxyl group can be determined [Hartmann 1999], which is greater than 98%. When a telechelic polymer is dispersed in water, telechelic chains self-assemble and form flower-like micelles with the hydrophobic stickers gather together forming a hydrophobic core. When a telechelic polymer is added to surfactant micelles, it either decorates the micelles forming a loop or links two distinct micelles forming a bridge as shown in Figure 2.1. Similarly, this also holds for surfactant stabilized oil-droplets in water (microemulsions).

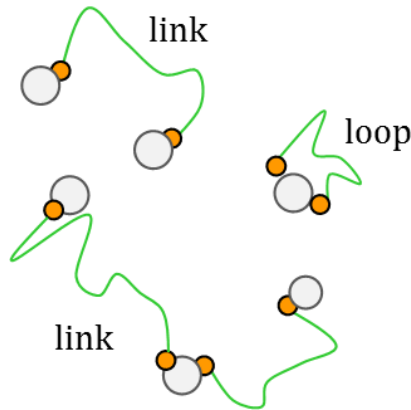


Figure 2.1: Schematic to show how telechelic polymer (hydrophilic chain in green and hydrophobics stickers in orange) cross-links the two distinct micelles or decorate the micelles by forming a loop.

2.1.1a Bridged microemulsion

Microemulsions are thermodynamically stable, transparent and homogeneous dispersions of oil droplets in water. We have used the same system of microemulsions as investigated in [Filali 1999, Molino 1999], shown in Figure 2.2. Decane is used to swell the droplets in brine (0.2 M NaCl) and surfactant cetylpyridinium chloride (CpCl) and co-surfactant n-octanol are used for the stabilization of the droplets by forming a surfactant film around the oil droplet. The radius of the droplet is equal to the spontaneous radius of curvature of the surfactant film. This radius can be adjusted according to two parameters:

$$\Omega = \frac{m_{\text{cosurfactant}}}{m_{\text{surfactant}}} \quad \text{and} \quad \Gamma = \frac{m_{\text{oil}}}{m_{\text{cosurfactant}} + m_{\text{surfactant}}}$$

$m_{\text{cosurfactant}}$, $m_{\text{surfactant}}$ and m_{oil} are the mass of cosurfactant, surfactant and oil respec-

tively. In our experiments, $\Omega = 0.25$ and $\Gamma = 0.56$ yielding stable microemulsions of radius 6 nm [Filali 2001].

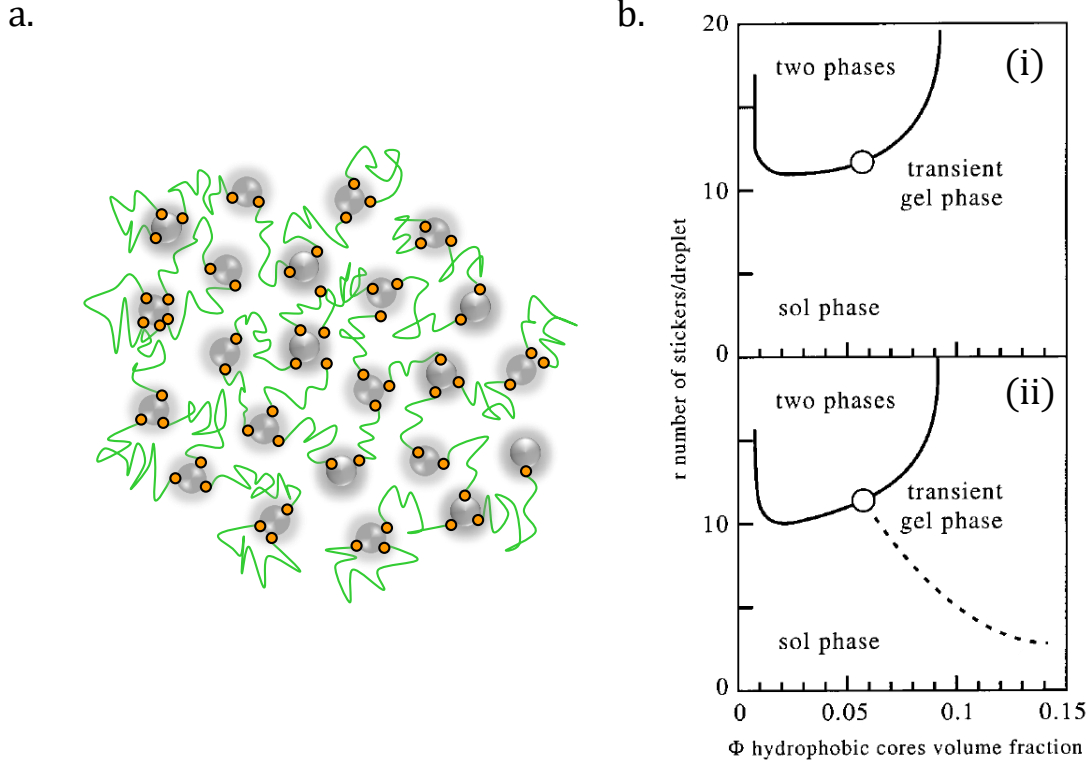


Figure 2.2: (a) A schematic of oil in water microemulsions bridged by telechelic polymers. (b) Phase diagram of microemulsion comprising telechelic polymer (i) C_{12} (ii) C_{18} , adapted from [Filali 2001].

To bridge the microemulsions, we have used telechelic polymers, with aliphatic chain length C_{12} and C_{18} . We can tune the mass fraction of the microemulsion, ϕ and the average number of stickers per oil-droplet, r . The parameters ϕ and r are defined as:

$$\phi = \frac{m_{\text{hydrophobic}} + m_{\text{oil}}}{m_{\text{total}}} \quad \text{and} \quad r = \frac{\text{number of polymer stickers}}{\text{number of oil droplets}}$$

Here, $m_{\text{hydrophobic}}$ is the mass of the hydrophobic part of surfactant, cosurfactant and telechelic polymer and m_{oil} is the mass of oil. For large range of ϕ and r , bridged microemulsions are monophasic, but this monophasic range can be divided into two sub-range depending on ϕ and r values. Figure 2.2b shows the phase diagram of microemulsions on addition of telechelic polymer as a function of ϕ the hydrophobic cores volume fraction and r the number of stickers per droplet. Sol phase exists for the low ϕ and r values and in this phase the samples flows easily. At high ϕ and r values, transient network forms and the samples in this phase are viscoelastic. The two phases are separated by the percolation line [Michel 2000, Filali 2001].

Sample preparation: We have fixed the average number of telechelic stickers per oil droplet, $r = 4$ and varied the mass fraction of oil droplets between 0.5 and 10%. Surfactant, CpCl is added to 0.2 M brine (NaCl in Milli-Q water) and properly mixed. Then octanol is added followed by decane. The mixture is swirled to ensure the proper mixing of the constituents. The solution is then filtered using a $0.22 \mu\text{m}$ filter. Then, the polymer is added to the filtered microemulsions. The mixture is stirred to obtain a one-phase transparent mixture. Samples are then stored in thermostat cabinet maintained at temperature 30°C . The erioglaucine dye of concentration 2.5 g/l is also added to the same samples for experimental study.

2.1.1b Bridged micelles

When surfactant molecules are added in the aqueous medium they tend to form aggregates known as micelles by creating an environment where the tail groups sequester in the interior, forming hydrophobic domains expelling most of the water. Head groups constitute the outer layer in the aqueous medium. There exists a concentration of surfactant above which surfactant molecules form micelles, known as the critical micellar concentration (CMC). Below CMC there are just free surfactant molecules in the aqueous medium. Shape and size of the micelles are controlled by the nature and size of an amphiphilic molecule, temperature, salt concentration, type of salt and addition of cosurfactant. Rehage and Hoffman, [Rehage 1988, Rehage 1991], showed that the shape of the micelles can be tuned by the cosurfactant to surfactant ratio. This ratio acts as an elongation factor for the micelles, allowing one to modify the surfactant aggregate from spheres to rods to wormlike tubes as shown in Figure 2.3.

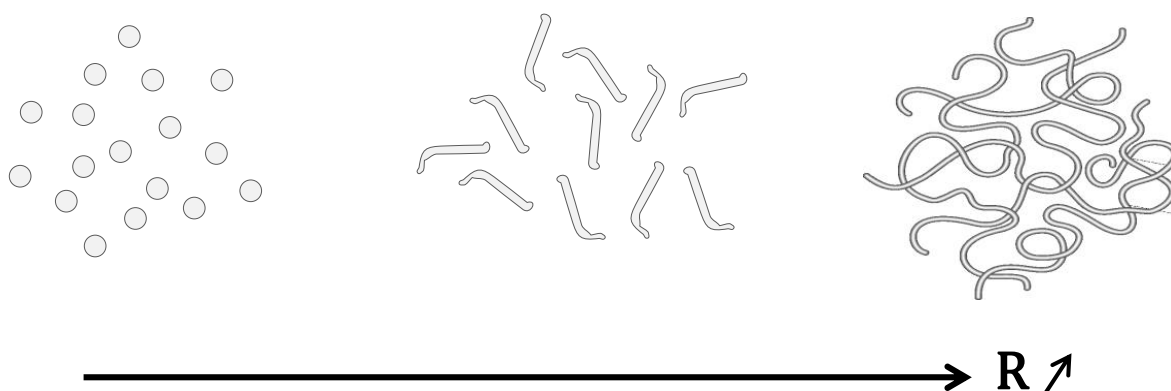


Figure 2.3: Schematic to show the change of morphology of the micellar system on varying the cosurfactant to surfactant ratio, R : spherical to rod-like to wormlike micelles.

Cetylpyridinium chloride (CpCl) is used as a cationic surfactant and sodium salicylate (NaSal) as a cosurfactant in brine (0.5 M NaCl) to form the micelles. Telechelic polymer of carboxylic chain length C_{12} , C_{18} and C_{23} are used to bridge the micelles.

[Tixier 2010]. The structural properties of bridged micelles of different morphologies are previously studied in our laboratory [Ramos 2011]. The samples are prepared by weight and to tune the morphology of the system, three parameters are taken into consideration, φ , mass fraction of the micelles, β , amount of polymer and R , cosurfactant to surfactant ratio:

$$\varphi = \frac{m_{\text{CpCl}} + m_{\text{NaSal}}}{m_{\text{total}}}, \quad \beta = \frac{m_{\text{polymer}}}{m_{\text{CpCl}} + m_{\text{NaSal}}} \quad \text{and} \quad R = \frac{n_{\text{NaSal}}}{n_{\text{CpCl}}}$$

Here, m_{CpCl} , m_{NaSal} , m_{total} , m_{polymer} , n_{NaSal} and n_{CpCl} are respectively, the mass of cetylpyridinium chloride, the mass of sodium salicylate, total mass of the sample, mass of triblock telechelic polymers, the mole number of sodium salicylate and the mole number of cetylpyridinium chloride in the mixture.

Similarly to bridged microemulsions (Section 2.1.1a), a percolation threshold also exists for the bridged micellar system. For spherical and short rodlike micelles bridged by telechelic polymers, there exists a critical concentration of φ or β , above which a transient network forms and behaves as a viscoelastic liquid, known as percolation threshold. For long cylindrical micelles, the network is self-sustaining even at low φ and β [Tixier 2010] and thus for the bridged wormlike micelles no such percolation exists.

Sample preparation: For sample preparation, we have fixed the mass fraction of micelles $\varphi = 10\%$ and the amount of polymer β is varied between 0 and 55%. Surfactant (CpCl) is added to 0.5 M brine (NaCl in Milli-Q water) and the mixture is stirred until a clear homogeneous solution is obtained. The solution is filtered using a 0.22 μm filter. Then, the polymer is added to the surfactant solution which is thoroughly mixed. The cosurfactant is added after complete dissolution of the polymer in the surfactant solution. The samples are stored in a thermostat cabinet maintained at temperature 30°C. All the samples prepared for the experiment are homogeneous and transparent.

2.1.2 Elastic beads

Polyacrylamide gels are prepared by copolymerization of acrylamide (monomer) and N, N' -methylenebisacrylamide (comonomer) in the presence of initiators in water. Tetramethylethylenediamine (TEMED) and sodium persulfate are often used to initiate the radical polymerization. TEMED is added to accelerate the production of free radicals from sodium persulfate by a redox reaction. The free radicals of sodium persulfate so generated, in turn, facilitate free radicals of acrylamide monomer. This is the initiation process which is followed by propagation, in which monomer radicals react with other monomers which are not radicalized and bisacrylamide cross-links the chain of monomers. Figure 2.4 shows the polymerization of acrylamide.

There are many factors which can inhibit the polymerization process, like presence of oxygen, impurities in monomer or comonomer. It is important to do the polymer-

ization reaction in an inert atmosphere and saturate the solutions with inert gas before commencing the polymerization reaction. Temperature also plays an important role, an optimal temperature of 23 – 25°C is good for the polymerization reaction [Menter 2000].

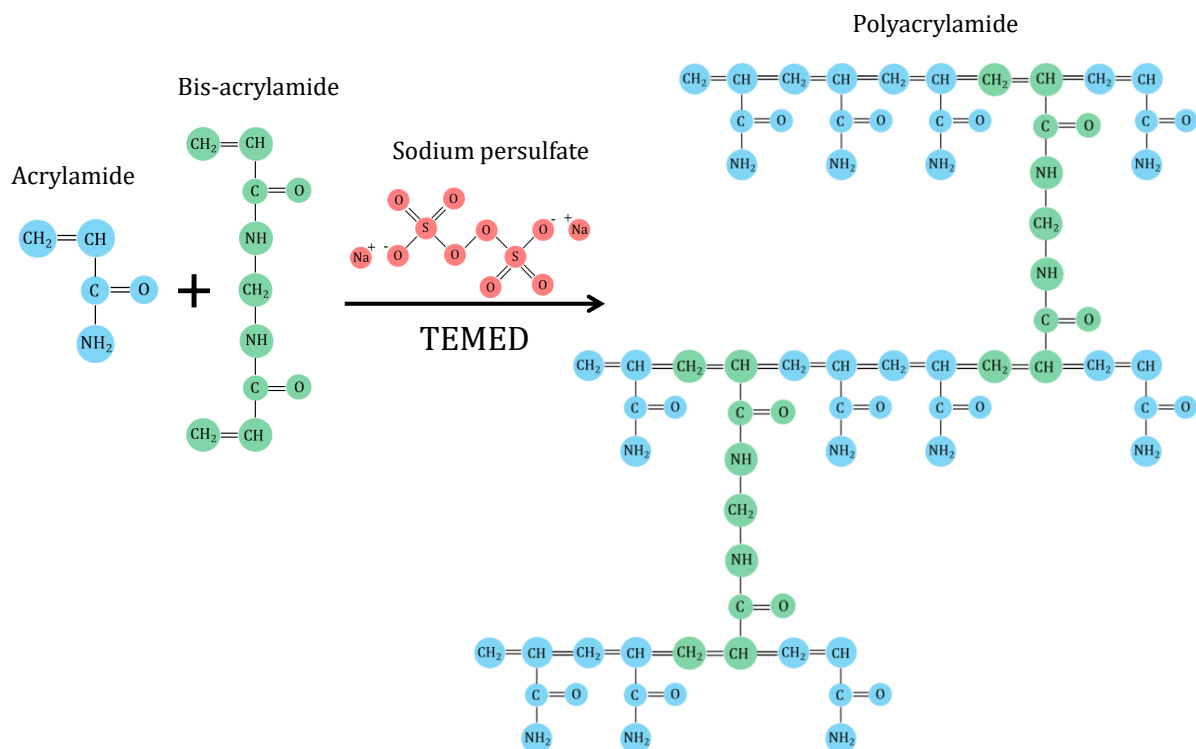


Figure 2.4: Polymerization reaction of acrylamide and bisacrylamide in presence of sodium persulfate and TEMED as an initiator.

Sample preparation: Elastic beads are home-synthesized from the guidance of Ty Phou. Elastic beads of fixed radius $r = 1.85$ mm are prepared. The polymerization reaction is done in a nitrogen atmosphere. Prior to mixing the constituents, all the solutions are saturated with nitrogen gas, to ensure the near insufficiency of oxygen. To tune the elasticity, Table 2.1 lists the range of concentration for different chemical constituents.

For a required elasticity of a polyacrylamide gel bead, solutions of monomer and comonomer are mixed in a beaker and then the TEMED and sodium persulfate are added. The solution is quickly swirled and then 26.5 μl (corresponding to drop radius 1.85 mm) of the solution mixture is transferred immediately to various eppendorf tubes, filled with poly(methylhydrosiloxane) oil. This oil has a density nearly equal to that of water (1.006 g/ml at 25°C) to support the floating drop. The remaining solution is left in the beaker (sealed from top) for the polymerization to occur and then it is later used to measure the elastic modulus.

Chemical Constituents	Concentration (g/l)
Acrylamide	28.80 - 46.03
Bis-acrylamide	0.186 - 0.373
Sodium Persulfate	0.93
Tetramethylenediamine	0.6

Table 2.1: Showing the range of concentration used for preparing polyacrylamide gel of different elasticity.

Erioglaurine disodium salt (dye) is used to improve the contrast of the images captured during experiments. Figures 2.5a and 2.5b show an elastic bead (dyed) floating in oil inside eppendorf and pinned to pipette tip in air, respectively. Time duration for the polymerization to finish for two polyacrylamide gels is shown in Figure 2.5c. The time for each polymerization to finish is approximately the same (80 mins) because the concentration of the two initiators is fixed in our sample preparation.

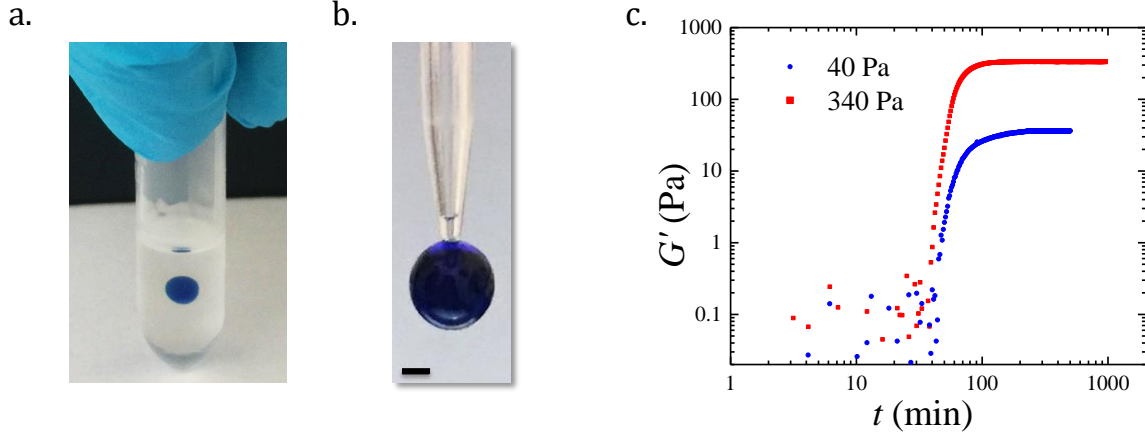


Figure 2.5: (a) Elastic bead floating in eppendorf filled with oil. (b) Elastic bead (radius $r = 1.85$ mm) of shear modulus $G_0 = 736$ Pa, scale bar is 1 mm. (c) Time evolution of shear modulus for a typical polymerization process to occur.

The elastic modulus is varied between 10 Pa and 740 Pa and overall 200 elastic beads are prepared. We show in Figure 2.6 elastic beads of different elastic moduli placed on a polypropylene sheet, under their own weight. Soft elastic beads deform more in comparison to harder beads.

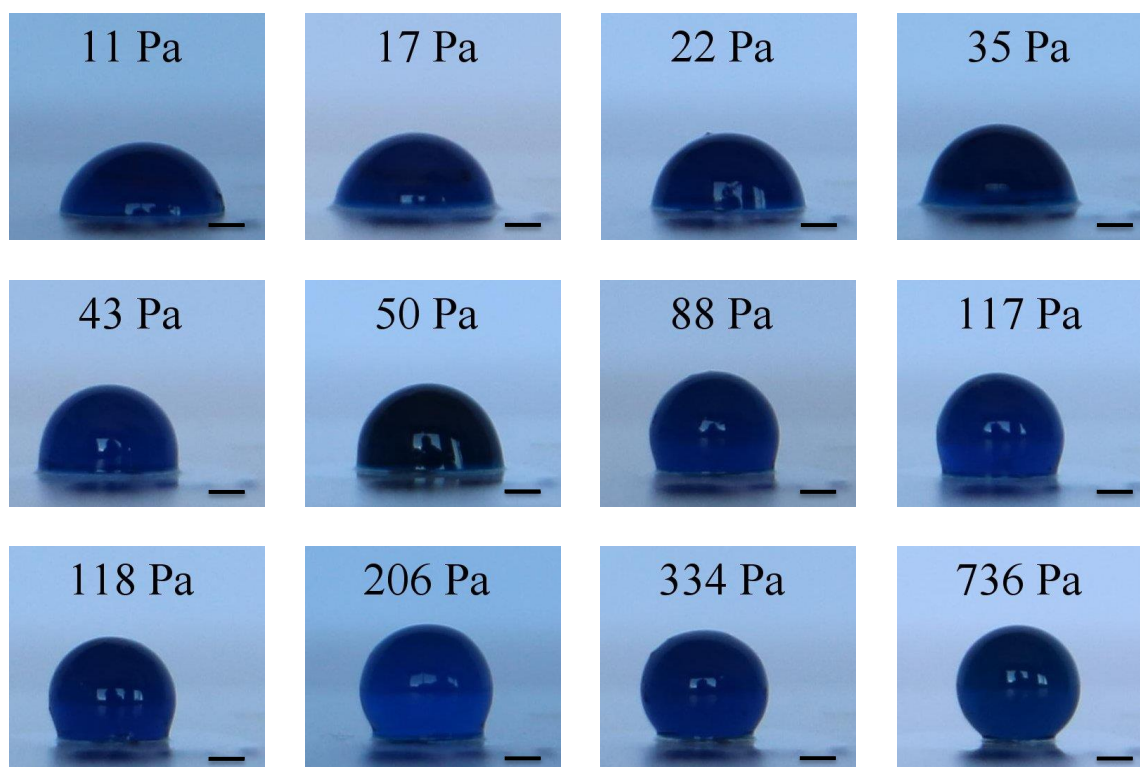


Figure 2.6: Images of prepared elastic beads with different elastic modulus as indicated, deposited on polypropylene sheet. The scale bars are 1 mm.

2.1.3 Newtonian fluids

Newtonian fluids are used to compare the experimental results with viscoelastic fluids and elastic systems. (i) Glycerol-water mixtures of varying weight percent of glycerol in water are prepared. The samples are eventually comprised of CpCl (5.88 mM) and 0.5 M NaCl. The equilibrium surface tension is measured using Wilhelmy plate tensiometer (KSV NIMA). The surface tension data is plotted in Figure 2.7a as a function of *wt%* of glycerol in water (with and without surfactant). The experimental data is comparable to literature values for pure glycerol-water mixture [producers association 1963]. We show in Figure 2.7b the evolution of zero-shear viscosity with *wt%* of glycerol in water. We have also checked that the addition of CpCl and NaCl does not modify the sample viscosity. The viscosity is varied between 1.8 mPa.s and 700 mPa.s. The measured experimental values are comparable to literature values [Sheely 1932] as indicated by the black solid line.

(ii) Ethanol-water mixtures are prepared with two different mole fractions of ethanol 0.033 and 0.17 having surface tension values (50.44 ± 0.2) mN/m and (32.54 ± 0.06) mN/m respectively. The surface tension for the mixture is measured with a pendant drop tensiometer (SINTERFACE PAT-1M) and are comparable to literature values [Khatab 2012].

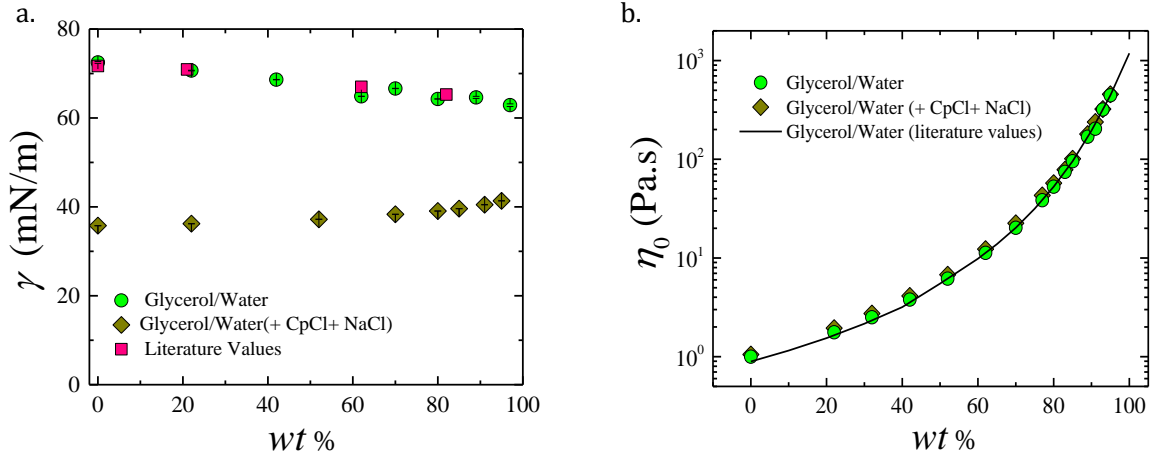


Figure 2.7: (a) Surface tension for different weight percent of glycerol in water (with and without surfactant). (b) Zero-shear viscosity for glycerol-water mixtures as function of wt% of glycerol in water (with and without surfactant).

2.2 Rheological methods

Rheology is the most common measurement done to study the simple flows and deformation of materials. Rheology allows one to determine the physical properties of the system such as viscosity, characteristic time, elastic modulus etc. There are two fundamental flows: shear flow and extensional flow.

In shear flow, fluid elements flow over or past each other under the action of force as shown in Figure 2.8a. Consider two parallel plates separated by a gap h . When a force F is applied on the top plate, it results in a deformation in the material between the plates. Top plate is displaced by an amount Δx . Thus, shear stress is defined as $\sigma = F/A$ and the shear strain as $\gamma = \Delta x/h$. The velocity gradient in direction perpendicular to the flow is called the shear rate $\dot{\gamma} = V_x/h$ ($\dot{\gamma} = \frac{1}{h} \frac{\Delta x}{\Delta t}$). V_x is the velocity in direction of force applied. For a constant shear rate, the fluid elements are separated linearly in time. For the elastic solid shear stress is proportional to shear strain ($\sigma = G\gamma$) and the constant of proportionality is known as shear modulus (G). For viscous materials, shear stress is proportional to shear rate ($\sigma = \eta\dot{\gamma}$) and the constant of proportionality is called viscosity (η).

In the case of an extensional flow, the fluid elements either flow towards each other or away from each other as shown in Figure 2.9a. Figure 2.9b shows the schematic of a cylinder undergoing uniaxial extensional flow due to the force applied in a direction perpendicular to the face of cylinder. The strain rate in this case is defined as $\dot{\epsilon} = d\epsilon/dt$ and $d\epsilon$ is the differential strain of the sample ($d\epsilon = dl/l$). Hence, one can deduce that the fluid elements are separated exponentially in time for the material undergoing extensional deformation ($l = l_0 e^{\dot{\epsilon}t}$) at a constant strain rate. This shows that the material undergoes

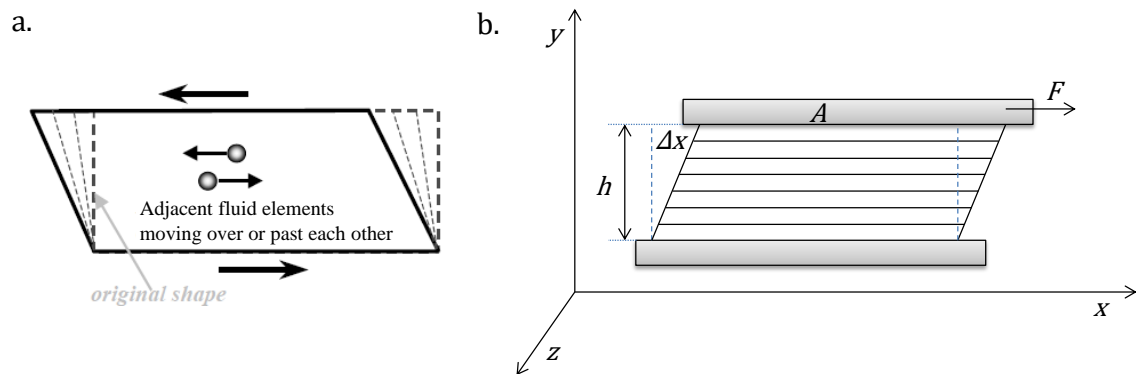


Figure 2.8: (a) Simple shear flow to show the effect on fluid elements when subjected to a force, adapted from [Barnes 2000]. (b) Schematic showing the deformation in the material when the force (F) is applied on top plate.

much stronger deformation in an extensional flow compared to shear deformation.

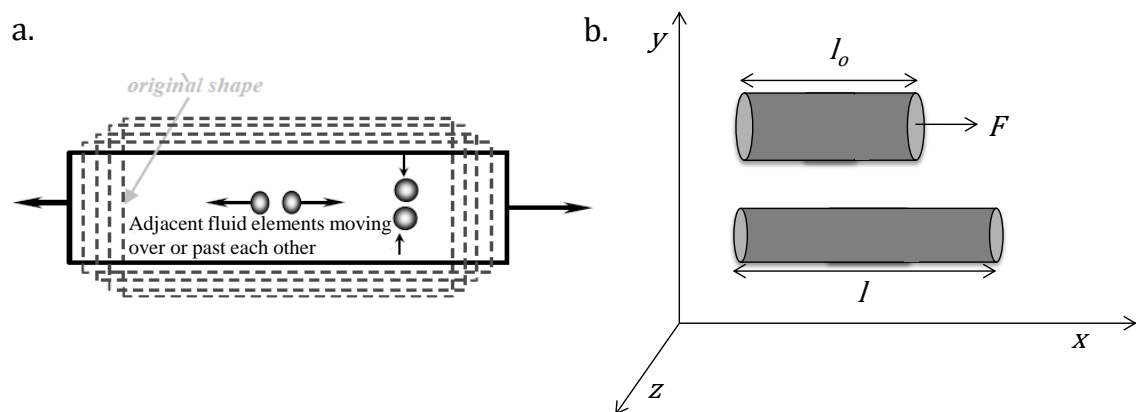


Figure 2.9: (a) Simple extensional flow to show the effect on particles when subjected to a force adapted from [Barnes 2000]. (b) Schematic showing the uniaxial extension in the case of a cylindrical material, when the force (F) is applied from one side.

Rheometers are used to study the rheological properties of materials. Example for a strain controlled rheometer equipped with simple flow geometries, the material undergoes deformation and corresponding resulting stress is measured to understand the nature of the material.

2.2.1 Shear rheological measurements

Shear rheology is performed to investigate the sample viscoelasticity. Two rheometers have been used, a strain-controlled rheometer (Ares from TA instrument) and a stress-controlled rheometer (MCR 502 from Anton-Paar), both equipped with a Couette

geometry. Initial measurements are performed with ARES TA instrument. Due to some technical problem with the rheometer, we had later on switch to MCR-502 Anton-Paar to carry forward the rheological measurements.

To understand the mechanical behavior of viscoelastic fluids, frequency sweep has been performed in the linear regime. In an oscillatory measurement, a sinusoidal shear deformation ($\gamma(t) = \gamma_0 \sin(\omega t)$) is imposed on the sample and the resultant stress response of viscoelastic material is measured as $\sigma(t) = G'(\omega)\gamma_0 \sin(\omega t) + G''(\omega)\gamma_0 \cos(\omega t)$. The measurement is done as a function of pulsation ω because the material can behave as elastic solid or viscous liquid depending on the time scale at which it is probed. Storage (G') and loss (G'') moduli are measured with frequency ω in the range (0.1 - 100 rad/s) for a fixed amplitude strain $\gamma_0 = 10\%$. G' is associated with a solid-like response while G'' with a liquid-like response of the material. Frequency dependence moduli of the viscoelastic samples are fitted using Maxwell models. Depending on the experimental system one mode or two mode Maxwell model is used to fit the data.

For bridged spherical micelles and microemulsions, frequency sweep data is fitted by a one mode Maxwell model:

$$G'(\omega) = \frac{G_0(\omega\tau)^2}{1 + (\omega\tau)^2} \quad (2.1)$$

$$G''(\omega) = \frac{G_0(\omega\tau)}{1 + (\omega\tau)^2} \quad (2.2)$$

Here G_0 is the shear modulus and τ is the characteristics time.

Figure 2.10a shows the frequency dependence G' and G'' together with the fit of G' and G'' from one mode Maxwell model for a C_{18} -bridged microemulsion ($\phi = 3\%$ and $r = 4$). Independent fits of G' and G'' using Equation 2.1 and 2.2 yields: $G_0 = (43.03 \pm 1.1)$ Pa, $\tau = (0.46 \pm 0.02)$ s (from G'), and $G_0 = (40.52 \pm 0.34)$ Pa, $\tau = (0.52 \pm 0.01)$ s (from G''). The fact that independent fitting of the storage and the loss moduli give equal values within 3% shows the good quality of the fits. There are some samples for which data at frequencies larger than the inverse of the relaxation time are not experimentally accessible. In that case, the Maxwell model can be approximated as $G'(\omega) \approx G_0(\omega\tau)^2$ and $G''(\omega) \approx G_0(\omega\tau)$. From the independent fitting of G' and G'' one can determine G_0 and τ . We show a plot in Figure 2.10b for a C_{18} -bridged micellar system ($\varphi = 10\%$ and $\beta = 24.64\%$), for which we find: $G_0 = (335 \pm 4.8)$ Pa, $\tau = (2.8 \pm 0.03)$ ms.

For entangled micellar systems, the two mode Maxwell model is used to fit the frequency sweep data and $G'(\omega)$ and $G''(\omega)$ are defined as:

$$G'(\omega) = \frac{G_{\text{slow}}(\omega\tau_{\text{slow}})^2}{1 + (\omega\tau_{\text{slow}})^2} + \frac{G_{\text{fast}}(\omega\tau_{\text{fast}})^2}{1 + (\omega\tau_{\text{fast}})^2} \quad (2.3)$$

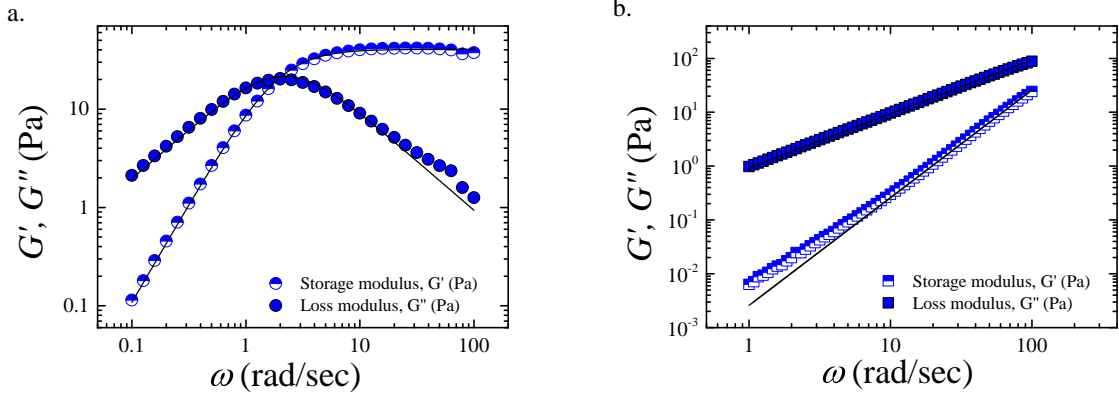


Figure 2.10: G' and G'' moduli dependence with the frequency, ω for (a) C_{18} -bridged microemulsion ($\phi = 3.0\%$ and $r = 4$) and (b) C_{18} -bridged spherical Micelles ($\varphi = 10\%$ and $\beta = 24.64\%$). Symbols are the experimental data points and lines are fits with one mode Maxwell model (Equation 2.1 and 2.2).

$$G''(\omega) = \frac{G_{\text{slow}}(\omega\tau_{\text{slow}})}{1 + (\omega\tau_{\text{slow}})^2} + \frac{G_{\text{fast}}(\omega\tau_{\text{fast}})}{1 + (\omega\tau_{\text{fast}})^2} \quad (2.4)$$

Here, G_{fast} and G_{slow} are the elastic plateau modulus of fast and slow mode, τ_{fast} and τ_{slow} are the relaxation time of fast and slow mode respectively. Elastic plateau modulus is the sum of fast and slow mode elastic modulus, $G_0 = G_{\text{slow}} + G_{\text{fast}}$. The slow mode is associated with the transient network of entangled micelles and the fast mode with the network of telechelic polymer bridging the micelles [Nakaya-Yaegashi 2008].

Figure 2.11 shows the frequency dependence of G' and G'' moduli (symbols) together with the fit of G' and G'' with a two mode Maxwell model (lines) for C_{23} -bridged wormlike micelles ($\varphi = 10\%$ and $\beta = 5\%$). Independent fit of G' and G'' gives: $G_{\text{slow}} = (220.03 \pm 7.08)$ Pa, $G_{\text{fast}} = (294.32 \pm 7.7)$ Pa, $\tau_{\text{slow}} = (1.7 \pm 0.09)$ s, $\tau_{\text{fast}} = (0.076 \pm 0.003)$ s (from G' , Equation 2.3) and $G_{\text{slow}} = (214.7 \pm 2.5)$ Pa, $G_{\text{fast}} = (289.7 \pm 3.5)$ Pa, $\tau_{\text{slow}} = (1.92 \pm 0.03)$ s, $\tau_{\text{fast}} = (0.095 \pm 0.003)$ s (from G'' , Equation 2.4). This gives $G_0 = (509.37 \pm 14.26)$ Pa.

For all the viscoelastic systems (self-assembled transient networks) and Newtonian fluids, zero shear viscosity η_0 is measured. Ramp of shear rate is applied in the range $(0.01 - 100 \text{ s}^{-1})$ and corresponding shear stress and viscosity are measured. Figure 2.12 shows the flow curve for two systems: C_{18} -bridged micelles ($\varphi = 10\%$ and $\beta = 25\%$) and C_{18} -bridged microemulsion ($\phi = 2\%$ and $r = 4$).

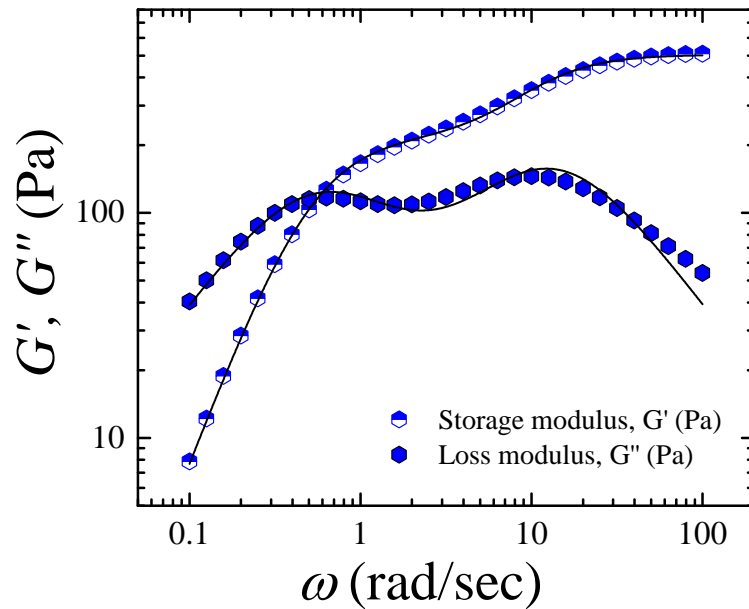


Figure 2.11: Frequency sweep data of C_{23} -bridged wormlike micelles ($\phi = 10\%$ and $\beta = 5\%$). Symbols are the experimental data points and lines are fits from two mode Maxwell model (Equation 2.3 and 2.4).

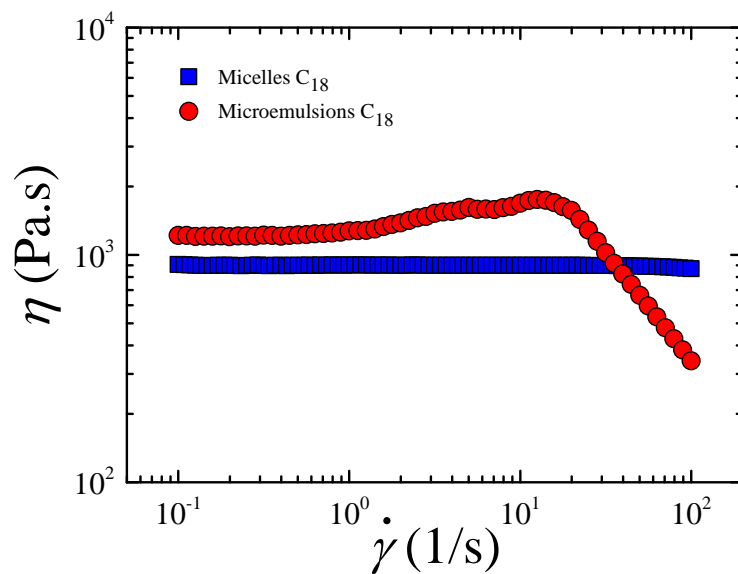


Figure 2.12: Flow curves, steady state viscosity vs shear rate, for a C_{18} -bridged micelle ($\phi = 10\%$ and $\beta = 25\%$) and a C_{18} -microemulsion ($\phi = 2\%$ and $r = 4$).

2.2.2 Extensional rheology measurements and imaging

To study the transient stress growth coefficient of viscoelastic fluids under the extensional deformation flow field, VADER 1000 (Versatile accurate deformation extensional rheometer) from Rheo Filament ApS [Huang 2016b] is used. These experiments are performed in Technical University of Denmark (DTU) in collaboration with Prof. Ole Hassager.

First, pure extensional rheological measurements are performed on VADER 1000. The sample is put in between the two cylindrical stainless steel plates of identical diameters (6 mm, 9 mm) aligned vertically (Figure 2.13).

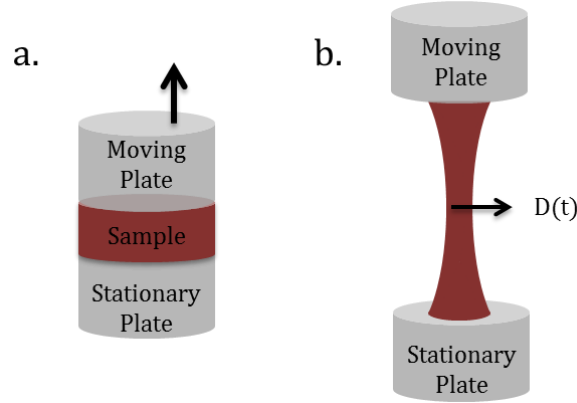


Figure 2.13: Schematic to show (a) when the sample is between the two cylindrical plates and (b) stretched filament. Diameter in time is recorded at mid-filament using laser micrometer.

The Hencky strain is defined as: $\varepsilon = -2\ln(D(t)/D_o)$, $D(t)$ is the mid-filament diameter measured at time (t) and D_o is the initial diameter. A laser micrometer is used to measure the diameter during the stretching. The motion of top plate is governed by a control loop scheme, with an active feedback control, to ensure the constant Hencky strain rate, $\dot{\varepsilon} = (d\varepsilon/dt)$ [Marín 2013]. This administers the uniaxial stretching at the mid-filament plane.

Transient stress growth coefficient, η_E^+ [Barnes 1989] was calculated from the mean stress difference at the mid-plane filament.

$$\eta_E^+ = \frac{\langle \sigma_{zz} - \sigma_{rr} \rangle}{\dot{\varepsilon}} = \frac{F(t)}{(\pi/4)D(t)^2\dot{\varepsilon}} \quad (2.5)$$

The different strain rates are applied to measure the response of viscoelastic material in viscous and elastic regimes. All the experiments are performed at ambient temperature, 25°C. Figure 2.14 shows the transient stress growth coefficient as a function of time for the C₂₃-bridged wormlike micelles ($\varphi = 10\%$ and $\beta = 5\%$) at different strain rates along

with the linear viscoelastic envelope (LVE). LVE is calculated from the Maxwell model fit parameters of the oscillatory shear measurement. For a Maxwell model with i modes, extensional stress growth coefficient is given as:

$$\eta_E^+ = 3 \sum_i G_i \tau_i (1 - \exp(-t/\tau_i)) \quad (2.6)$$

Here, G_i and τ_i are the elastic modulus and characteristic time for the i Maxwell mode. Strain hardening is observed for this sample, characterized by an abrupt increase of η_E^+ as compared to LVE.

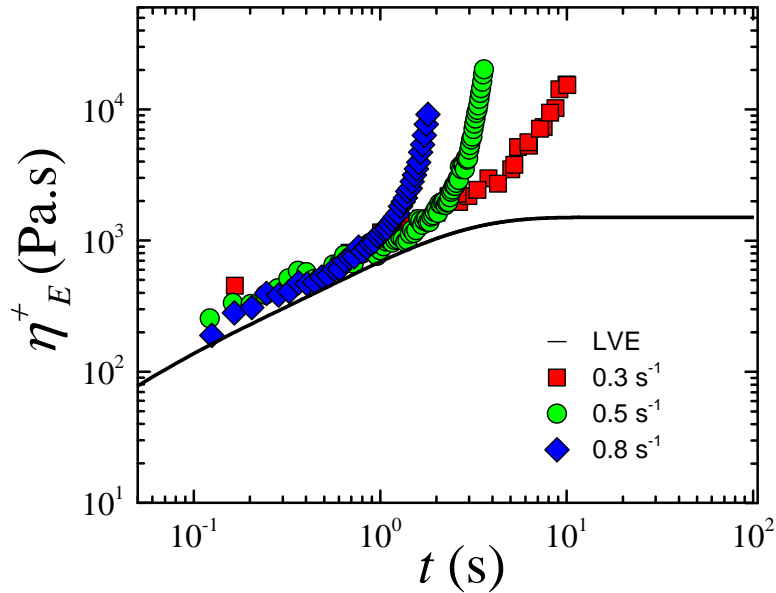


Figure 2.14: Growth of η_E^+ in time for different Hencky strain rates as indicated in the legend for C₂₃-bridged wormlike micelles ($\varphi = 10\%$ and $\beta = 5\%$). Symbols are data points obtained from extensional experiment and line shows the LVE calculated from Maxwell model parameters (Equation 2.6).

The measurements performed in control loop with a laser micrometer for constant strain rates are used to calculate feedforward control parameters [Marín 2013]. These parameters define the kinematic trajectory of the top plate during stretching. This is done because the laser micrometer cannot be used while doing imaging of a stretching filament. High-speed camera Photron Mini UX100 is coupled with VADER 1000 for the image acquisition [Shabbir 2016]. Time series of filament stretching is recorded at the operating setting of 5000 frames/s at the resolution of 1280×1000 pixel². Figure 2.15 shows the time series of images of the filament undergoing stretching.

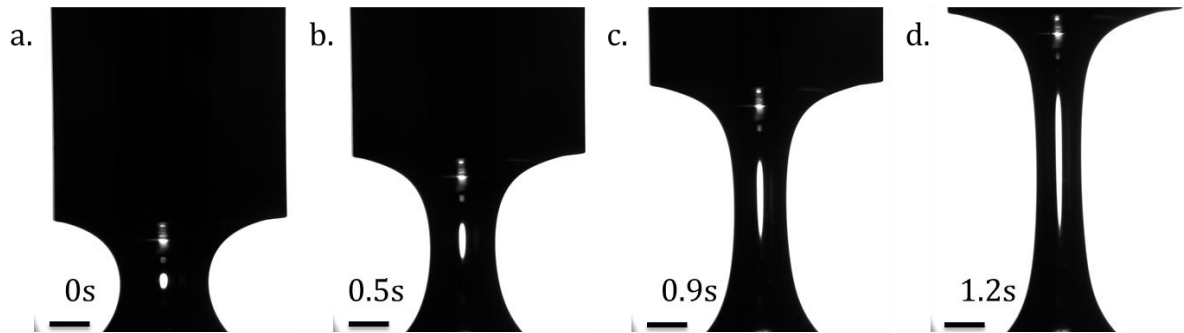


Figure 2.15: Stretching of a filament in time at Hencky strain rate 1 s^{-1} for pure wormlike micelles ($\varphi = 10\%$). The scale bar are 1 mm.

2.2.3 Measurement of the elastic modulus of elastic beads

In this section, we present a method to determine the shear modulus G_0 of very soft elastic gels. This method has been developed in the lab by Jean-Marc Fromental and Serge Mora. A scheme of the set-up is shown in Figure 2.16.

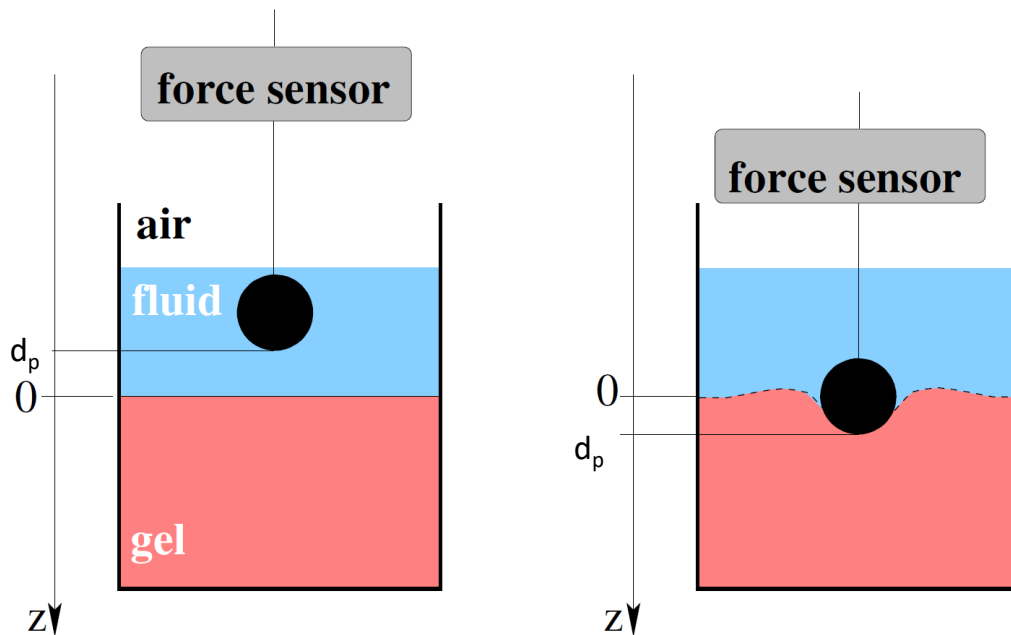


Figure 2.16: A container is partially filled with a gel with shear modulus G_0 and the gel is covered with a liquid. A rigid sphere indents the initially horizontal surface of the gel. The penetration depth of the sphere below the gel surface is d_p , and the (vertical) force applied to the sphere is F .

The horizontal surface of the gel is covered by the gel's solvent of density ρ_{fluid} , and a centimetric sphere of radius R indents gradually the surface of the gel. A thin rod is fixed perpendicular to the surface of the rigid sphere. The sphere is first completely immersed

in the liquid and then gradually pushed down. Note that the vertical rod supporting the sphere is assumed to be thin enough so that excess buoyancy due to the change in the immersed volume is negligible. The force F exerted on the rod in order to drive the motion of the sphere is measured. F is constant until the bottom of the sphere reaches the surface of the gel. Let F_0 be the value of this constant force. An additional downward vertical displacement of the sphere requires a deformation of the gel surface. The force F then increases.

The effects of gravity, surface energies, and adhesion forces are physically removed by the solvent so that the unique remaining force is the elastic one, which can thus be precisely measured.

Let d_p be penetration depth of the sphere below the initial location of the gel-fluid interface. We consider quasi-static states (so that the kinetic energy is negligible) and we take the configuration with an unstressed gel as a reference. Following the arguments of Hertz theory, the radius a of the contact area is of the order $\sqrt{Rd_p}$. In the absence of any significant disturbance, the solution provided by Hertz [Hertz 1895, Johnson 1987] for the contact of a rigid sphere in an elastic half-space applies.

For $d_p < 0$, the sphere is completely immersed in fluid,

$$F = F_0 = \frac{4\pi}{3}R^3(\rho_{\text{fluid}} - \rho_{\text{sphere}})g \quad (2.7)$$

When the sphere is in contact with the gel ($d_p > 0$). The relationship between the indentation depth and the normal force is given by:

$$F = \frac{16}{3}G_0R^{1/2}d_p^{3/2} + F_0 \text{ for } d_p > 0. \quad (2.8)$$

The experimental protocol follows directly from Equation 2.8. The force F_0 is measured by a force sensor before the sphere has reached the surface of the gel ($d_p < 0$). Then, the unique remaining parameter in Equation 2.8 to be fitted with the experimental data points for $d_p > 0$ is G_0 .

As an example we show in Figure 2.17 the force F applied to the vertical rod holding the sphere as a function of the vertical displacement of the sphere. We measure a constant force F_0 prior the contact ($F = F_0$), and a supplementary force ($F - F_0$) that increases as $d_p^{3/2}$ beyond the contact point (i.e. for $d_p > 0$), in agreement with Equation 2.8.

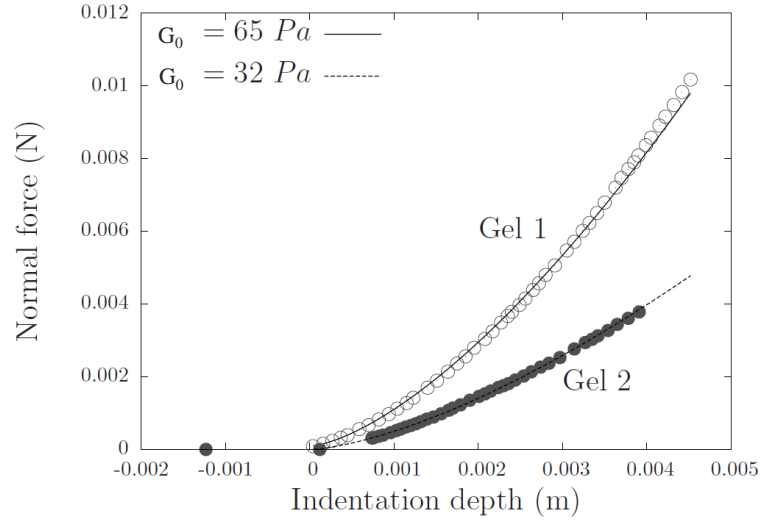


Figure 2.17: Indentation force $F - F_0$ as a function of the penetration depth for two different gels. The lines are fits of the experimental data with Equation 2.8, with F_0 and G_0 as fitting parameters.

2.3 Experimental set-ups

This section focuses on two experimental set-ups that have been used and developed to investigate the impact dynamics of thin sheets.

2.3.1 Drop impact on a small target

The experimental set-up used to study the impact of a liquid drop on a small cylindrical target has been originally designed by Vignes-Adler et al. [Rozhkov 2002]. Schematic of the set-up is shown in Figure 2.18.

A hydrophilic target of diameter, $d_t = 6$ mm is made from aluminum and a glass lamella is affixed on top of the cylinder. The solid target is conjoined with a coaxial cylinder [Villermaux 2011] to keep the ejection angle of the sheet to 90 degree with respect to the solid target. The liquid drop is injected from a syringe pump through a needle placed vertically above the target. The size of the falling droplets is dictated by the inner diameter of the syringe and the equilibrium surface tension of the samples. In order to maintain a constant droplet size, needles with different diameters are used to account for the various equilibrium surface tension of the samples.

A vertical tube is integrated into the set-up which is held between the needle and slightly above the target to lessen the effects of air currents. The target is fixed on transparent plexiglass plate, illuminated from below by a high-luminosity backlight (Phlox LLUB, luminance of $19,842$ cd/m²). Time series are recorded after the impact of the drop using a high-speed camera (Phantom V7.3) operated at 6700 frames/s and resolution

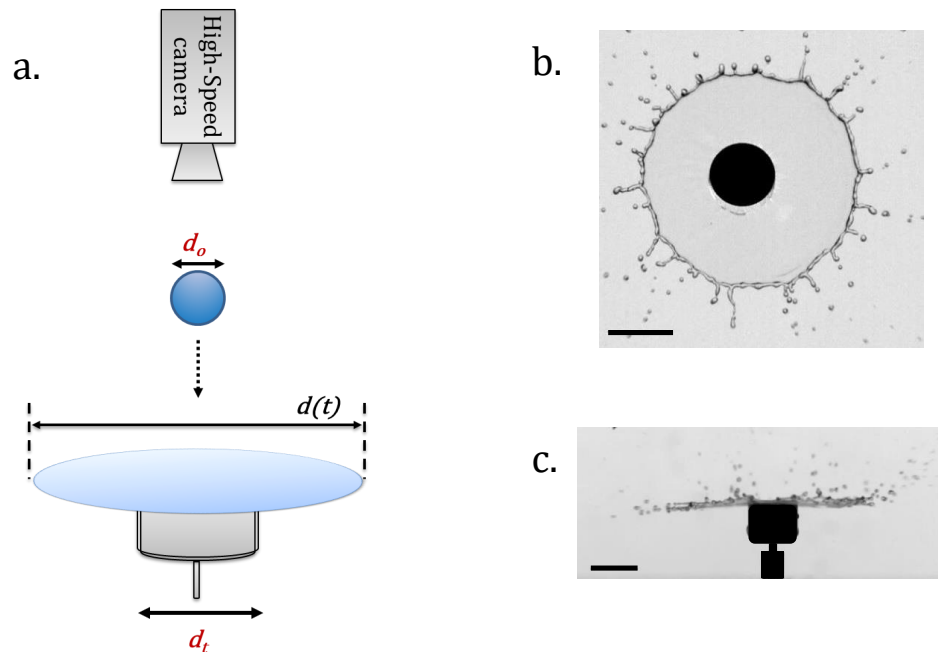


Figure 2.18: (a) Schematic to show the experimental set-up. (b) and (c) Maximum expansion of a liquid sheet from the top and side view for pure water with $d_o = 3.7$ mm and $v_o = 4$ m/s. The scale bars are 6 mm

800×600 pixels². Figure 2.19 shows the time evolution of a liquid sheet produced by the impact of a water drop. After the drop impact, a liquid sheet freely expands in air. The sheet is bounded by the thicker rim that destabilizes into ligaments, which subsequently disintegrates into secondary drops. The sheet then retracts back due to surface tension.

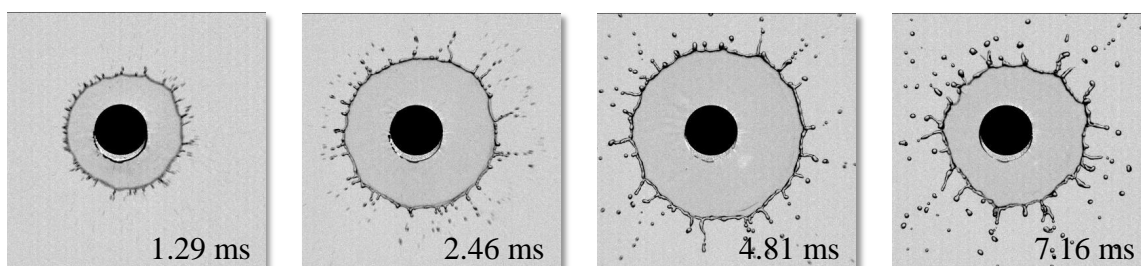


Figure 2.19: Time series of the liquid sheet produced by the impact of water drop. Time instant is indicated in the images. The target (black disk) of diameter 6 mm sets the scale.

To measure the impact velocity, v_o and to ensure the flatness of the sheet, side view imaging is also done. The experimental values are comparable to the theoretical values (within 7% error) calculated using the relation, $v = \sqrt{2gh_n}$, where g is the acceleration due to gravity and h_n is the height of the needle from the target. We used this theoretical

relation with the assumption of free fall and negligible air friction. v_o is varied from 4.3 m/s to 1.3 m/s and h_n between 111 cm and 11 cm respectively.

There is a finite possibility of rupture of an expanding sheet (dewetting) at a solid-liquid interface. To suppress the dewetting, glass disc is treated with a plasma gun (Corona Surface Treater, Electro-Technic products) to facilitate the hydrophilicity to ensure the wetting on the glass lamella [Vernay 2015a].

2.3.2 Drop impact using an inverse Leidenfrost effect

To substantially eliminate the role of a solid surface on the dynamics of liquid sheet, we have designed an experimental set-up based on inverse Leidenfrost phenomenon [Hall 1969]. Leidenfrost effect was first reported in 1756 [Leidenfrost 1756]. In a Leidenfrost phenomenon, when a liquid drop at ambient temperature comes in contact with a hot surface, having a temperature much higher than the boiling point of the drop, a vapor layer is formed. This layer thermally insulates the drop from evaporating instantly, instead, it levitates on its own vapor cushion. There is a critical temperature above which this phenomenon is observed known as Leidenfrost temperature. This temperature depends on the nature of the substrate, the physical properties of droplet under study, the impact velocity, the atmospheric pressure and presence of impurities. It is, therefore difficult to realize this temperature for several experimental systems. For our experimental study, we have instead worked with inverse Leidenfrost configuration. This is achieved by impacting a drop at ambient temperature on a silicon wafer covered with a thin layer of liquid nitrogen at $T = -196^\circ\text{C}$. At the impact of drop (relatively hotter than liquid nitrogen), local vapor cushion forms at the liquid-surface interface due to the evaporation of liquid N_2 . This vapor layer thermally insulates the droplet from freezing instantly, proving a unique scenario of nonwetting and slip conditions which decreases the viscous dissipation [Antonini 2013].

Figure 2.20 represents a schematic diagram of the experimental set-up. Expanded polystyrene is used to make a box of dimension 35 cm \times 35 cm which acts as a liquid nitrogen bath. Plexiglass is used to cover the box, to form an enclosed chamber to minimize the boiling of liquid nitrogen by homogenizing the environment inside the chamber with N_2 gas, to minimize the humidity and to protect against the air currents. Polished Silicon wafer (Si-Mat silicon materials) is used as a solid substrate for the impact of liquid drops and elastic beads. The level of liquid N_2 is maintained in the bath below the silicon wafer to avoid the boiling droplets of liquid N_2 to hover on the surface. Due to the very low temperature of a silicon wafer, frosting occurs on its surface. To limit this from interfering with the impact of a liquid drop or elastic bead, two holes are pierced in the polystyrene to make inlets for compressed N_2 gas and liquid N_2 . Before each impact of a liquid drop or an elastic bead, the silicon wafer is cleaned by blowing the compressed N_2 gas and then a finite layer of liquid N_2 is deposited.

The liquid drops or elastic beads are ejected from a needle placed above the silicon

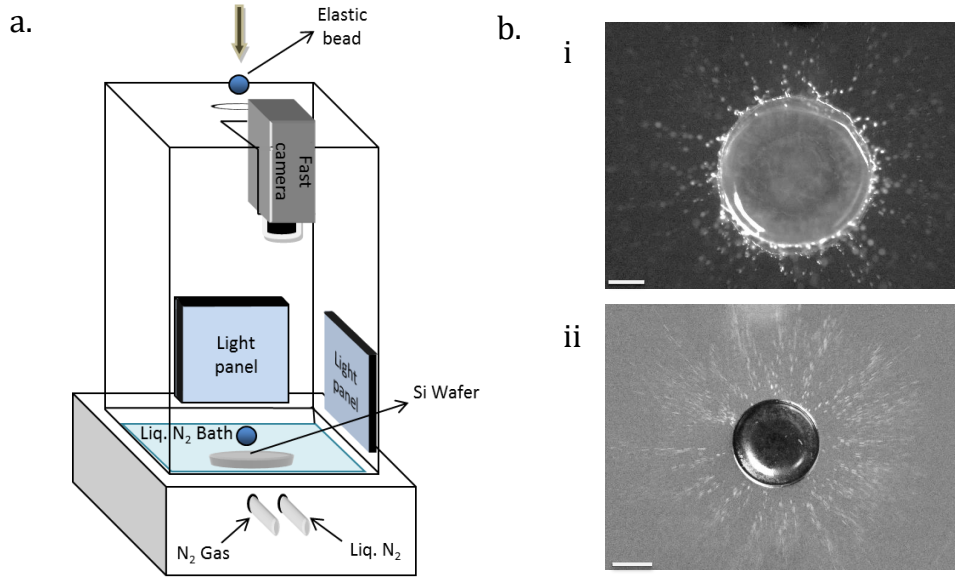


Figure 2.20: (a) Illustration of the experimental set-up, and (b) snapshots of sheet produced with (i) liquid, ethanol-water mixture (surface tension 50 mN/m) and (ii) solid, elastic bead (elastic modulus $G_0 = 118$ Pa). The scale bars are 6 mm.

wafer. The needle is fixed on a movable cylindrical tube to change the distance between the substrate and needle, thus varying the impact velocity. Liquid drops are injected from a syringe pump through the needle. The fixed diameter of the falling drop is maintained as explained above (section 2.3.1). In the case of elastic beads, a needle (narrow tip) is attached to a syringe via a flexible tube. The bead is pinned at the needle by gently sucking air. On ceasing the suction, the bead is released. To record the time series of images, a fast camera (Phantom V7.3) is used with operating setting of 6700 frames/s and with the resolution of 800 pixels \times 600 pixels. High-intensity backlights (Phlox HSC, luminance of 98,203 cd/m² and Phlox LLUB, luminance of 19,842 cd/m²) are used to properly illuminate the chamber for image acquisition. Side view imaging is also done to measure the impact velocities, and later are compared with the theoretical relation, $v = \sqrt{2gh_n}$.

Experimentally, one cannot completely prevent the evaporation of liquid nitrogen, but it can be slowed down to a point where the experiments (that lasts a few ms) can safely be performed on a finite thin layer of liquid N_2 . Visually, it is easy to follow the evaporation front as shown in Figure 2.21a where the arrow guides the direction of evaporation. In addition, we have tried to minimize the crown formation due to the splash of liquid N_2 upon impact of a liquid drop or elastic bead, owing to low surface tension 8.9 mN/m of liquid nitrogen. The liquid drop or elastic beads are impacted just at the onset of evaporation of liquid nitrogen from the silicon wafer. Each distinct sample of elastic bead or liquid drop impact is repeated 5 times to ensure the reproducibility of the measurements. Figure 2.21b shows the maximum expansion of a liquid sheet produced by

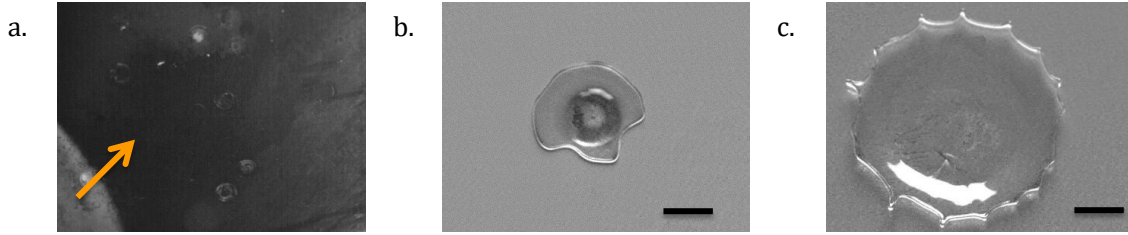


Figure 2.21: Images showing the effect of liquid nitrogen on the maximum expansion of a liquid drop. (a) Arrow showing the evaporation front of liquid nitrogen. (b) and (c) Images showing the maximum diameter of glycerol-water mixture (zero-shear viscosity 227 mPa.s) on cold surface of silicon wafer without liquid nitrogen and in presence of liquid nitrogen layer. The scale bars are 6 mm.

the glycerol-water mixture in the presence of liquid nitrogen and devoid of liquid nitrogen.

2.4 Image analysis

This section describes the techniques used to quantitatively analyze images obtained from different experiments using a fast camera.

(i) For the experiments done using the set-up of "Drop impact on a small target" (section 2.3.1) time series of the liquid sheet (formation, expansion, and retraction) is recorded. Image J software is used to compute the time-evolution of the sheet diameter. As shown in Figure 2.22a, the contour of the sheet is determined by thresholding the images (filaments are also taken into account), and using Wand (Tracing) tool, the sheet area A is measured, from which an effective diameter of the liquid sheet is deduced using the simple geometric relation, $d = \sqrt{4A/\pi}$. Figure 2.22b shows the diameter of liquid sheet calculated for the whole process of expansion and retraction. Diameter (d) of a liquid sheet is plotted as a function of time (t). For the pure water sample shown here, the sheet reaches its maximal expansion, $d_{\max} = 21.03$ mm, at time $t_{\max} = 4.82$ ms.

For the drop impact experiments performed using inverse Leidenfrost effect (section 2.3.2), the contour of the sheet is manually picked and the area of the sheet is measured to calculate the effective diameter, due to the insufficiency of the contrast to perform automatic thresholding.

(ii) To study the heterogeneity in the sheet, erioglaucline disodium salt (dye) is used in the preparation of samples. Variation of intensity in time is evaluated by choosing four ROIs of equal area, 5 mm^2 at fixed position in the sheet. The mean intensity (I) and standard deviation ΔI are measured in time for each ROI as shown in Figure 2.23. The coefficient of variation ($\Delta I/I$) is calculated to study the relative magnitude of standard deviation in time. Figure 2.24 shows the time evolution of coefficient of variation of intensity for liquid sheet produced from the impact of a water drop. The empty symbols

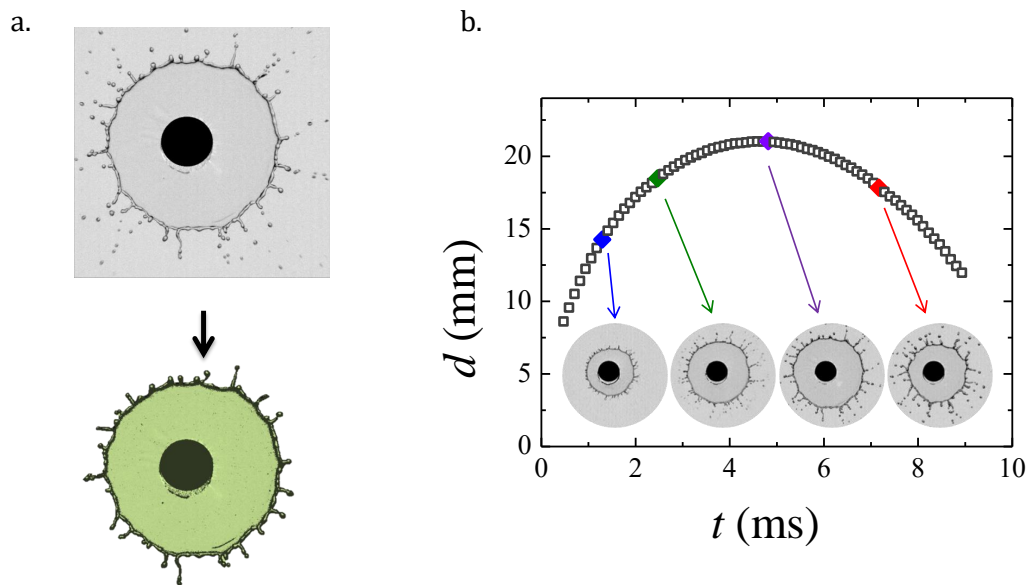


Figure 2.22: (a) Maximum diameter of the sheet for water on thresholding to calculate the area of the sheet by picking the contour of sheet by the Image J wand tool. (b) Time evolution of the sheet diameter for pure water. Images of the liquid sheet at different times are shown in the inset. The target (black disk) of diameter 6 mm sets the scale.

shows the variation from four different ROIs and black solid line shows the averaging done in time over the four ROIs.

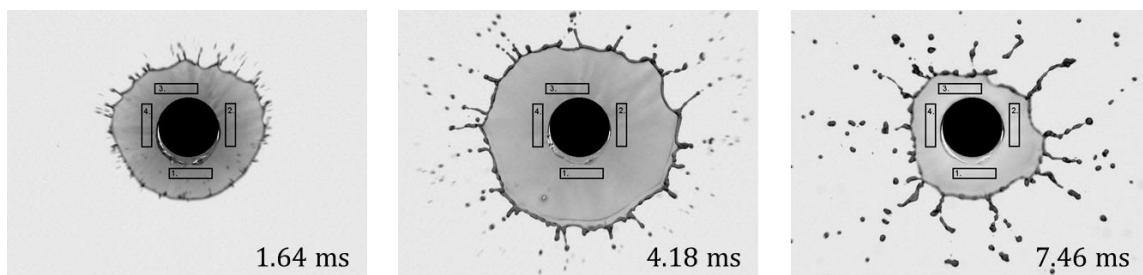


Figure 2.23: Time evolution of the liquid sheet produced with the water (dye). Four ROIs are marked at fixed points in the sheet. The target (black disc) of diameter 6 mm sets the scale.

In addition, to compare the data at maximum expansion of the sheet for different samples, manual outline (in black) is sketched to cover the whole sheet area as shown in Figure 2.25. The mean intensity and standard deviation are noted for the sketched region (in green), excluding the rim and area around the solid target.

(iii) Images of a filament of viscoelastic samples stretched using the extensional rheometer (section 2.2.2) are analyzed using Matlab. To quantify a crack, a Matlab

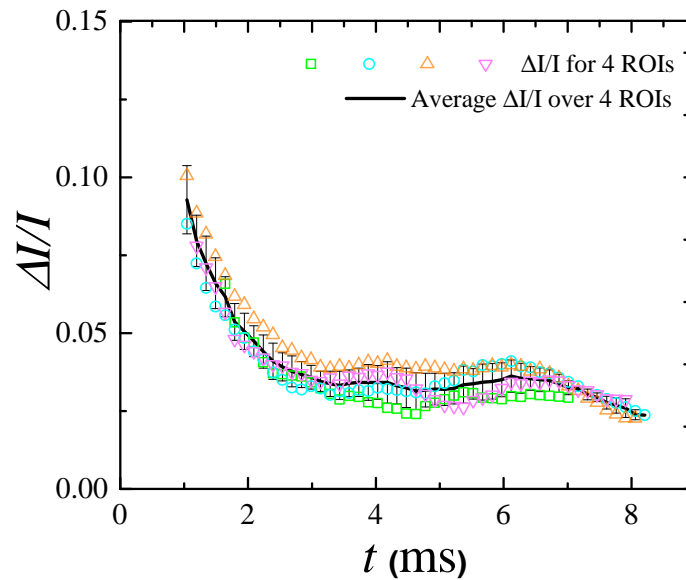


Figure 2.24: Time evolution of coefficient of variation ($\Delta I/I$) of the intensity for a liquid sheet generated by the impact of water drop. The symbols show the data from the four different ROIs and black solid line shows the average $\Delta I/I$ over four ROIs.

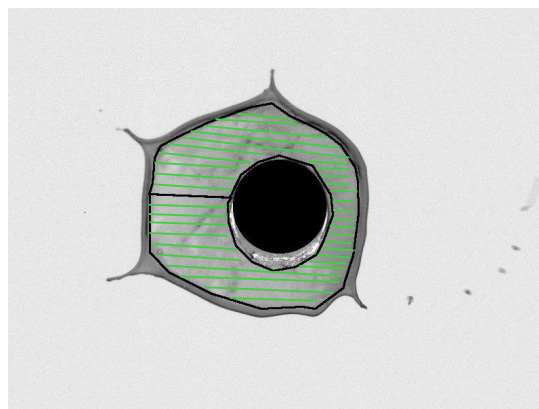


Figure 2.25: Maximum expansion of the sheet produced with a C_{18} -bridged microemulsion ($\phi = 2.75\%$ and $r = 4$). Mean intensity and standard deviation are measured over the entire sheet area shown by marked green lines.

code is developed to pick the coordinates which outline the crack as shown in Figure 2.26. Matlab code is based on intensity cut-off value, which allows one to pick intensity values on the periphery of the fracture. This allows one to compute the corresponding position coordinates and the vertex of the crack tip.

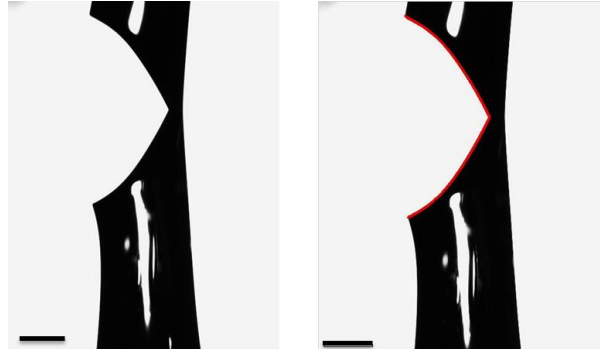


Figure 2.26: Crack profile of bridged wormlike micelles ($\varphi = 10\%$ and $\beta = 15\%$) (left) and the coordinates picked by the Matlab program (shown in red) to outline the crack profile (right). The scale bars are 1 mm.

Interplay between Viscosity and Elasticity in Freely Expanding Liquid Sheets

Contents

3.1	Experimental samples and techniques	46
3.2	Linear viscoelasticity	46
3.3	Dynamics of viscous and viscoelastic sheets	49
3.3.1	Dynamics of liquid sheets: $De \ll 1$	49
3.3.2	Dynamics of liquid sheet: $De \approx 1$ and $De \gg 1$	58
3.4	Conclusion	62

In this chapter, the dynamics of freely expanding liquid sheets prepared with fluids with different rheological properties has been investigated, (i) viscous fluids with a zero-shear viscosity η_0 in the range (1–1000) mPa.s and (ii) viscoelastic fluids whose linear viscoelastic behavior in the frequency range (0.1 – 100) rad/s can be accounted by a Maxwell fluid model with characteristic elastic modulus G_0 , relaxation time τ , and zero-shear viscosity $\eta_0 = G_0\tau$, which can be tuned over several orders of magnitude. The sheets are produced by impacting a drop of fluid on a small cylindrical solid target. For viscoelastic fluids, we show that when τ is shorter than the typical lifetime of the sheet ($\tau_{\text{life}} \sim 10$ ms), the dynamics of the sheet is similar to that of Newtonian viscous liquids with equal zero-shear viscosity. In that case, for less viscous samples ($\eta_0 \lesssim 30$ mPa.s), the maximum expansion of the sheet, d_{max} , is independent of η_0 , whereas for more viscous samples, d_{max} decreases as η_0 increases. We provide a simple model to account for the dependence of the maximal expansion of the sheet with the viscosity that is based on an energy balance between inertia, surface tension, and viscous shear dissipation on the solid target, and which accounts well for our experimental data. By contrast, when τ is longer than the typical lifetime of the sheet, the behavior drastically differs. The sheet expansion is strongly enhanced as compared to that of viscous samples with comparable zero-shear viscosity, but is heterogeneous with the occurrence of cracks, revealing the elastic nature of the viscoelastic fluid.

Most of the content of this chapter has been published in [Arora 2016]

3.1 Experimental samples and techniques

Two classes of self-assembled transient networks have been used: surfactant micelles (spherical micelles) and surfactant stabilized oil droplets (microemulsions) suspended in water and reversibly linked by telechelic polymer. Telechelic polymers used for bridging the two classes of self-assembled transient networks consist of PEO block of weight 35 kg/mol with the aliphatic chain length, C_n with $n = 12$ or $n = 18$. To compare the experimental results obtained from self-assembled transient networks, tests with Newtonian glycerol-water mixtures are also performed. A glycerol-water mixture comprising of surfactant, CpCl (5.88 M) and NaCl (0.5 M) is used to see the effect of surface tension. Table 3.1 shows the range of composition used for the preparation of samples. The samples are prepared by weight.

Experimental Samples	Experimental parameters
Bridged Micelles	mass fraction of micelles, $\varphi = 10\%$ polymer concentration, $\beta : 0\% - 50\%$
Bridged Microemulsions	average number of telechelic stickers per droplet, $r = 4$ mass fraction of oil droplets, $\phi = 0.5\% - 10\%$
Glycerol/Water (with and without surfactant)	weight fraction of glycerol: $0\% - 97.5\%$

Table 3.1: Showing composition for different classes of the samples.

Shear rheology is used to investigate the sample viscoelasticity and viscosity as explained in Chapter 2 (section 2.2.1). Thin sheets freely expanding in the air are produced by impacting a single drop of fluid on a solid target as explained in section 2.3.1 and the techniques used for image analysis are described in section 2.4.

3.2 Linear viscoelasticity

The sample composition is varied in order to tune the sample viscoelasticity. Our objective is to produce viscoelastic samples with relatively low zero shear viscosity so that drops can be produced and impacted on the target. As shown previously for similar systems [Michel 2000, Tixier 2010] the experimental samples investigated here (spherical micelles and microemulsion reversibly linked by telechelic polymers) behave as purely viscous liquids below a percolation threshold and exhibit viscoelasticity above the threshold. In contrast to previous investigations [Tabuteau 2009, Tixier 2010, Tabuteau 2011], we here focus on the region of the phase-diagram close above the percolation threshold.

Samples above the percolation threshold behave as Maxwell fluids and are characterized by an elastic shear plateau modulus, G_0 , and a characteristic relaxation time, τ . These parameters are determined by fitting the frequency-dependent moduli of the samples with the Maxwell model. Here, one varies the formulation, i.e. the mass fraction of oil droplets, ϕ , for the emulsion-based samples, and the amount of telechelic polymers, β , for the micelle-based samples, in order to approach the percolation threshold where G_0 and τ vanish critically. One defines ε as the normalized distance from the percolation threshold: $\varepsilon = \frac{\beta - \beta_c}{\beta_c}$ for the micelle-based samples and $\varepsilon = \frac{\phi - \phi_c}{\phi_c}$ for the oil droplets-based samples.

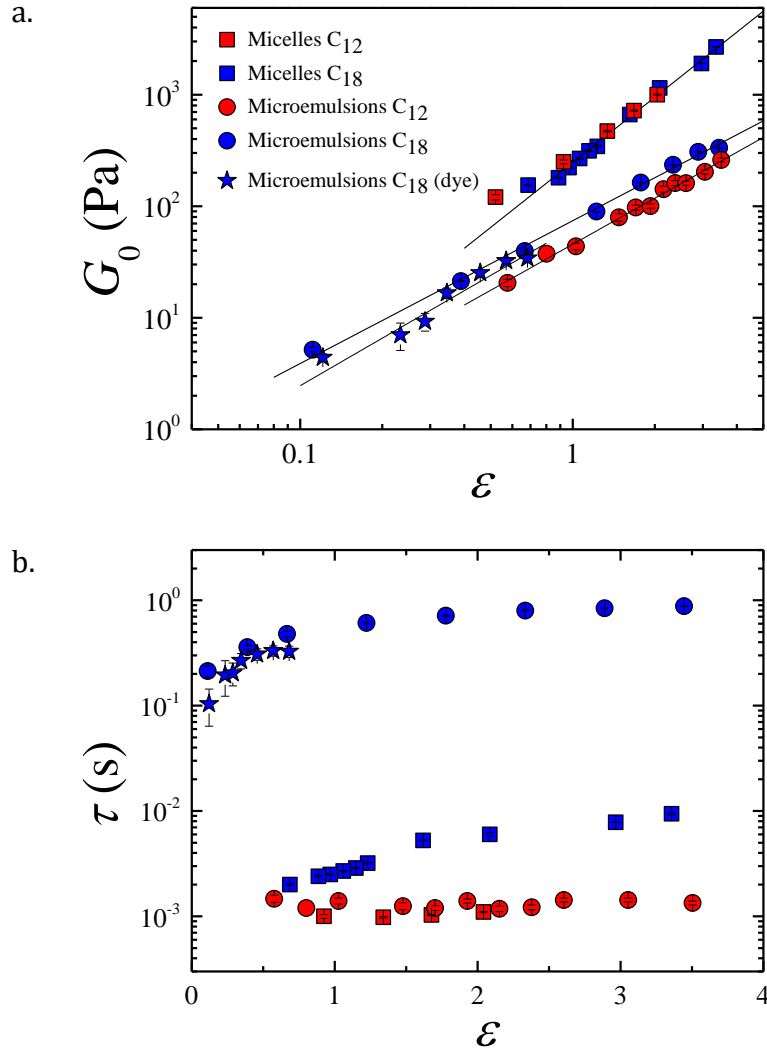


Figure 3.1: (a) Elastic shear plateau modulus and (b) characteristic relaxation time of viscoelastic samples as a function of the distance from the percolation threshold. Symbols are data points and the lines are power law fits of the experimental data.

Figure 3.1a shows the evolution of the shear elastic plateau modulus with ε for the four classes of samples (spherical micelle and microemulsion comprising telechelic polymers with C₁₈- and C₁₂-long hydrophobic stickers). In all cases, close to the percolation threshold, the evolution of the elastic modulus with the distance from the percolation threshold can be approximated by a power law fit: $G_0 = A\varepsilon^p$ [Tixier 2010]. Numerical values of the percolation thresholds, and of the exponent p , as derived from a power law fit of the data, are given in Table 3.2. Notably, we found for each class of samples (micelle-based and microemulsion-based networks) comparable values for the percolation threshold and for the exponent, p , which are found independent of the telechelic polymer used.

Sample	$\phi_c(\%)$	$\beta_c(\%)$	p
Micelles C ₁₈		13.5	1.76
Micelles C ₁₂		11.5	1.76
Microemulsion C ₁₈	1.8		1.28
Microemulsion C ₁₂	2.2		1.37

Table 3.2: Percolation thresholds and critical exponents of the shear plateau moduli for the four classes of transient networks.

On the other hand, the characteristic relaxation times τ strongly varies, as shown in Figure 3.1b, where the evolution of τ with ε is plotted for the four classes of samples investigated. Indeed, changing the length of the hydrophobic carboxylic stickers leads to a change of the average residence time of the stickers in the micelles and oil droplets, implying, in turn, modification of the characteristic viscoelastic relaxation times. We note that the relaxation times for the C₁₈-microemulsion-based samples are systematically about two orders of magnitude larger than those for the C₁₈-micelle-based samples. Using the four classes of samples, one therefore has access to viscoelastic samples whose relaxation times span almost three orders of magnitude (from 1 ms to 880 ms). The zero-shear viscosity, η_0 , of the samples, below and above the percolation threshold (above percolation threshold, $\eta_0 = G_0 \times \tau$) is plotted in Figure 3.2. Below percolation threshold ($\varepsilon < 0$), the viscosity of the C₁₂- and C₁₈-based samples are roughly equal, and weakly increases with ε . Above percolation threshold, η_0 increases more sharply with ε , and, as expected, the viscosity of the C₁₂- and the C₁₈-based samples strongly differ. Overall the zero-shear viscosity spans more than 6 orders of magnitude, from viscosity close to the one of water (0.0012 Pa.s) to 307 Pa.s.

Notably, Maxwell fluids that display the same zero-shear viscosity but with drastically different characteristic relaxation time are available, allowing one to decouple the effect of viscosity and of elasticity in the processes at play in the dynamics of freely expanding sheets. For the Newtonian fluids, zero-shear viscosity varies between 1.8 mPa.s and 700 mPa.s, the addition of CpCl and NaCl does not modify the sample viscosity.

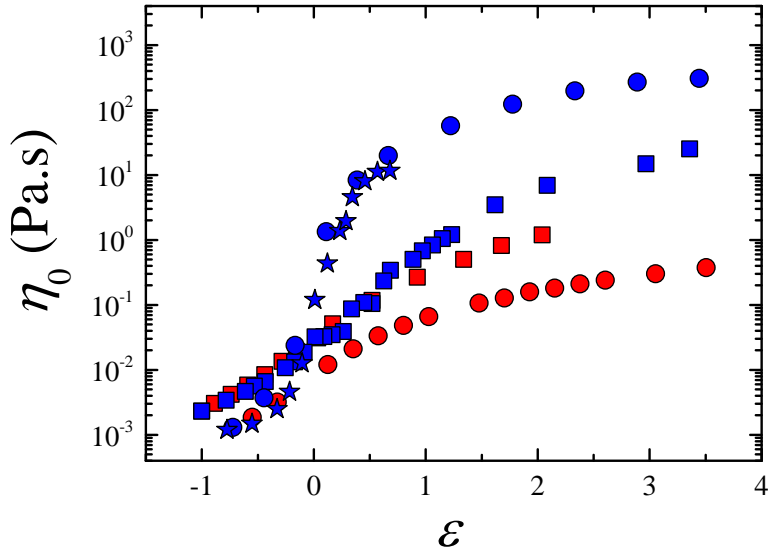


Figure 3.2: Zero-shear viscosity of viscoelastic samples as a function of the distance from the percolation threshold. Symbols are the same as in Figure 3.1

3.3 Dynamics of viscous and viscoelastic sheets

For viscoelastic fluids, a relevant parameter is the Deborah number, De , defined as the ratio between the characteristic relaxation time of the viscoelastic samples and the lifetime of the sheet (typically 10 ms). From the viscoelasticity measurements (Figure 3.1b), one deduces that the only class of samples for which De is significantly larger than 1 is the microemulsions linked by C_{18} telechelic polymers. For the C_{18} -based micelles, $De \cong 1$, whereas for the C_{12} -based samples, $De \ll 1$.

3.3.1 Dynamics of liquid sheets: $De \ll 1$

3.3.1a Experimental observations

Figure 3.3 displays a series of images of sheets produced by impacting drops of Newtonian fluids of various viscosities (mixtures of water and glycerol and a micellar system). It qualitatively shows that with the increase in the zero shear viscosity, maximum expansion of the sheet decreases. At the same time, ejection of secondary droplets from the rupture of ligaments decreases and ceases above $\eta_0 \simeq 100$ mPa.s.

In Figure 3.4 we show the time evolution of the effective sheet diameter for samples with various zero-shear viscosity, η_0 . For the sake of clarity, we have only shown data for glycerol/water mixtures and C_{12} based micellar system. The two sets of data display similar features. As η_0 increases, the sheet expands less: the maximum diameter d_{\max} is

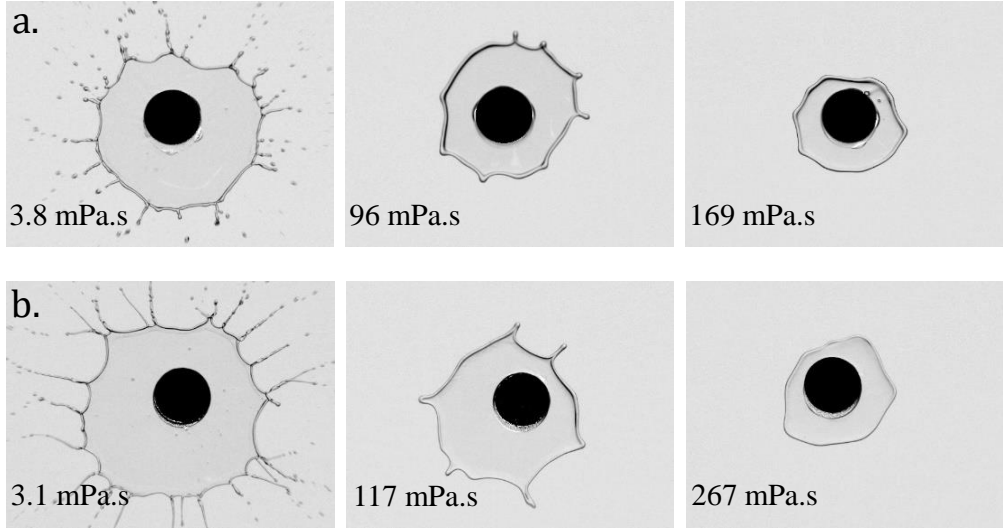


Figure 3.3: Snapshots of (a) viscous sheets made of water/glycerol mixtures and (b) sheets made of C_{12} -based micellar system, of various zero-shear viscosities as indicated. In (b), the sample with the lowest viscosity $\eta_0 = 3.1$ mPa.s is viscous and the two other samples are viscoelastic. Images are taken at the maximal expansion of the sheets.

smaller and is reached earlier.

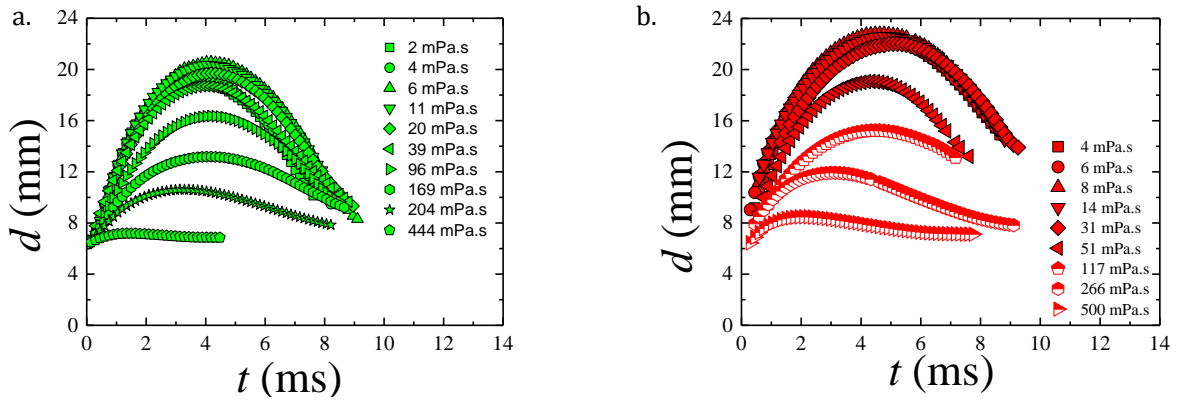


Figure 3.4: Time evolution of the sheet diameter for (a) glycerol/water mixtures and (b) C_{12} based micellar system of various viscosities as indicated in the legend. Half filled symbols are representing the viscoelastic samples.

We quantify how the maximum expansion depends on viscosity and plot in Figure 3.5 the maximal diameter normalized by its value at small viscosity (the inviscid case), $\tilde{d} = \frac{d_{\max}}{d_{\max}(\eta_0 \rightarrow 0)}$ as a function of the zero-shear viscosity (bottom x -axis). We find that the maximal diameter is constant $d_{\max} = (21.2 \pm 1.2)$ mm, and independent of the viscosity for $\eta_0 \leq \eta_c \sim 30$ mPa.s, and then continuously decreases with η_0 . We notice that, in the viscosity regime where the sheet dynamics is affected by the viscosity ($\eta_0 > \eta_c$),

volume loss due to ejection of secondary droplets is negligible. The evolution of the normalized maximal expansion diameter, \tilde{d} , with the viscosity, η_0 , for the C_{12} -based micelles and microemulsions superimposes quite well over the whole range of viscosity investigated with the data acquired for water/glycerol mixtures. These samples, although being viscoelastic, behave as purely viscous samples. This is shown qualitatively in the images displayed in Figure 3.3b taken at the maximal expansion of sheets produced with C_{12} -based micelles, and more quantitatively in Figure 3.5.

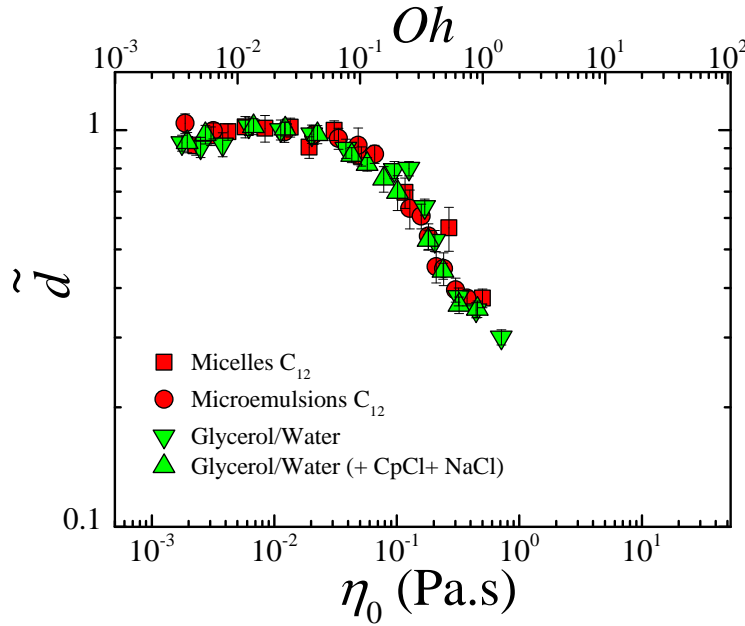


Figure 3.5: Maximum diameter (normalized by its value at low viscosity), as a function of zero-shear viscosity (bottom x axis) and Ohnesorge number (top x axis).

We note that data obtained for pure water/glycerol mixtures and for water/glycerol mixtures containing surfactant and salt perfectly collapse over the whole range of viscosity investigated. The two classes of mixtures differ by their equilibrium surface tension: $\gamma = (66.9 \pm 3.4) \text{ mN.m}^{-1}$ for pure water/glycerol and $\gamma = (38.5 \pm 2.0) \text{ mN.m}^{-1}$ for the mixtures with CpCl and NaCl. Because of this difference, the diameter of the needle used to dispense the drops has been modified in order to obtain droplets of equal size for all water/glycerol mixtures. However, the collapse of the two sets of data suggests that the equilibrium surface tension is not relevant to account for the sheet expansion. This is presumably due to the fact that on the time scale needed to reach the maximal expansion (at most 4 ms), the surface tension of the air/liquid interface does not have enough time to reach its equilibrium value. This time scale can be estimated as $t_d = \frac{\pi}{4D} \left(\frac{\Gamma_{\text{eq}}}{C_B} \right)^2$, where D is the diffusion coefficient of the surfactant molecules, Γ_{eq} is the surface concentration of the surfactant at equilibrium and C_B is the bulk surfactant concentration [Bonfillon 1994]. For CpCl, $\Gamma_{\text{eq}} = 5 \times 10^{-10} \text{ mol/cm}^2$, and $D = 8.6 \times 10^{-6}$

cm²/s in water ($\eta_0 = 1$ mPa s) [Rillaerts 1982], yielding for a bulk concentration of 5.88 mM, $t_d = 0.7$ ms in pure water. Hence, because D is expected to scale as the inverse of the viscosity, the time scale needed to reach the equilibrium surface tension exceeds the time scale needed to reach the maximal expansion of the sheet for viscosity larger than ~ 5 mPa s. Consequently, for large viscosity the relevant surface tension of the water/glycerol/CpCl mixtures is expected to be that of water/glycerol mixtures, as observed experimentally. Note, finally that surface tension gradients are presumably not relevant in our experiments. Indeed, because of Marangoni stresses, such gradients would cause perforation of the sheet [Vernay 2015c, Rozhkov], which is never observed in our experiments.

The normalized maximal diameter, \tilde{d} , is also plotted as a function of the Ohnesorge number, Oh (top x axis, Figure 3.5). The Ohnesorge number is a dimensionless number that represents the ratio of internal viscous dissipation to surface tension energy: $Oh = \frac{\eta_0}{\sqrt{\rho\gamma d_o}}$, where ρ is the sample density, η_0 its zero-shear viscosity, γ the surface tension and d_o the drop diameter. Accordingly, for small Oh ($Oh \lesssim 0.1$), the maximal expansion of the sheet is governed by a balance between inertia and surface tension, whereas the higher Oh , the more dominant the viscous dissipation is.

3.3.1b Modeling

(i) **Theoretical model:** We provide here a modeling of the data obtained for Newtonian fluids and micellar and micro-emulsions based samples bridged by C₁₂ polymer. We use a standard energy conservation approach as a starting point. For an inviscid fluid, the kinetic energy of the drop upon impact is mainly converted into surface energy [Marmottant 2000, Villermaux 2011]. A rough estimate of the maximal expansion diameter of the sheet can be derived by balancing the kinetic energy of the drop and the surface energy at the maximal expansion of the sheet. In the case of a viscous drop, some amount of energy is dissipated during the process, reducing the inertial expansion. We assume that part of the impact energy is dissipated by a radial flow in the liquid sheet. Balancing the initial kinetic energy against the surface energy at the maximal extension of the sheet and the viscous dissipation energy E_{diss} yields:

$$\frac{1}{2}mv_0^2 \approx \frac{\gamma\pi d_{\text{max}}^2}{2} + E_{\text{diss}} \quad (3.1)$$

Here, m is the mass of the drop, v_0 is the impact velocity and γ is the surface tension. Note that Equation 3.1 neglects the interfacial energy between the target and the liquid (this is expected to hold as long as $d_t \ll d_{\text{max}}$) and assumes that the sheet has a disk shape (the external rim is neglected). We have neglected the dissipation that might occur in the rim due to vortical flows [Clanet 2004]. We define an effective velocity v_{eff} as the impact velocity of a fictive drop of the same but inviscid fluid that will lead to the same maximal extension of the sheet. By definition, no dissipation occurs in this case, and the

energy balance reads:

$$\frac{1}{2}mv_{\text{eff}}^2 \approx \frac{\gamma\pi d_{\text{max}}^2}{2} \quad (3.2)$$

The dissipation energy therefore reads: $E_{\text{diss}} = \frac{1}{2}mv_0^2\left(1 - \left(\frac{v_{\text{eff}}}{v_0}\right)^2\right)$. The maximal diameter of the sheet normalized by its value in the inviscid case is obtained by considering Equation 3.1 (with $E_{\text{diss}} = 0$) and Equation 3.2 yielding:

$$\tilde{d} \approx \frac{v_{\text{eff}}}{v_0} \quad (3.3)$$

To model the effective velocity using a theoretical approach, we make a parallel with experiments on so-called Savart sheets, formed through the impact of a slender jet on a small disc at high Reynolds number [Clanet 2002]. In the stationary regime, the effect of the disc is to induce a shear viscous dissipation, which alters the liquid film velocity at the edge of the target leading to [Clanet 2001, Yarin 2006, Roisman 2009, Villermaux 2013]:

$$\frac{v_{\text{eff}}}{v_0} \approx \frac{1}{1 + \zeta} \quad (3.4)$$

Here v_{eff} is the velocity of the liquid film at the edge of the target, v_0 is the impact velocity of the liquid jet, and ζ is the ratio between the thickness of the viscous boundary layer, δ , and the thickness of the fluid sheet at the edge of the target, h , as calculated from mass conservation. This model ensures that outside the target region, the flow of the viscous sheet emerging from the impacting jet is identical to the flow of an inviscid liquid jet, provided that the impact velocity v_0 is replaced by the effective velocity v_{eff} . On the other hand, it has been shown theoretically [Villermaux 2011] that the kinematics fields of the liquid sheet arising from the impact of a drop of an inviscid fluid onto a small target are a time-dependent adaptation of a steady-state axisymmetric solution of Euler equations for a continuous jet impacting a solid target. These predictions have been confirmed experimentally [Vernay 2015b, Vernay 2015c]. Hence, following Clanet and Villermaux [Clanet 2002, Villermaux 2011] we assume that the effect of the viscous dissipation after the impact of the drop on the target with an impact velocity v_0 can be evaluated by considering that the flow of the viscous sheet is equivalent to the flow of an inviscid liquid sheet with an impact velocity v_{eff} given by Equation 3.4. The scaling of the parameter ζ is however different when one considers a jet and a drop impacting the target. In the case of a single drop of diameter d_o hitting a target of diameter d_t , simple mass conservation yields for the thickness of the fluid sheet when it fully covers the target (yet does not expand in air):

$$h \approx \frac{2}{3}d_o(d_o/d_t)^2 \quad (3.5)$$

On the other hand, the thickness of the viscous boundary layer reads $\delta = \sqrt{\frac{\eta T}{\rho}}$ with $T \approx \frac{d_t}{2v_0}$ the time needed to reach the edge of the target. Hence:

$$\delta \approx \sqrt{\frac{\eta_0 d_t}{2\rho v_0}} \quad (3.6)$$

In the case of a single drop the adimensional parameter $\zeta = \frac{\delta}{h}$ therefore reads:

$$\zeta \approx \frac{3}{2\sqrt{2}} \frac{1}{\sqrt{Re}} \left(\frac{d_t}{d_o}\right)^{5/2} \quad (3.7)$$

where $Re = (\rho v_0 d_o)/\eta$ is the Reynolds number. In our experimental conditions, ζ varies from 0.03 to 0.96. From Equation 3.2, one therefore derives a simple expression for the maximal extension of the sheet:

$$\frac{d_{\max}}{d_o} \approx \sqrt{\frac{We}{6}} \frac{1}{1 + \zeta} \quad (3.8)$$

where $We = (\rho v_0^2 d_o)/\gamma$ is the Weber number, ρ is the density of the liquid and γ is the surface tension. Once written for parameters normalized by their values in the inviscid case, Equation 3.8 reads:

$$\tilde{d} \approx \frac{1}{1 + \zeta} \approx \frac{1}{1 + \alpha\sqrt{\eta_0}} \quad (3.9)$$

with

$$\alpha = \frac{3}{2\sqrt{2}} \frac{1}{\sqrt{\rho v_0 d_o}} \left(\frac{d_t}{d_o}\right)^{5/2} \quad (3.10)$$

Equation 3.9 shows that the maximal extension continuously decreases with the square root of the sample viscosity. We check quantitatively this simple prediction with the experimental results obtained from water/glycerol mixtures and C₁₂-based viscoelastic fluids of various viscosities (Figure 3.7). The dashed line (Figure 3.7) is the theoretical prediction (Equation 3.9) using the calculated value $\alpha = (1 \pm 0.1) \text{ (Pa.s)}^{-0.5}$ (Equation 3.10). Error bars for α come from uncertainties on the drop diameters. Note that here we have taken an average value for the water/glycerol density (1125 kg/m³) and have neglected the increase in the density as the mixture gets enriched in glycerol, this increase (at most 20 %) being negligible compared to that of the viscosity (3 orders of magnitude). We find that the theoretical model provides a correct order of magnitude of the normalized diameter but systematically underestimates the dissipation. A fit of the experimental data using α as unique fitting parameter yields $\alpha = (1.46 \pm 0.13) \text{ (Pa.s)}^{-0.5}$ but does not provide a significantly better account of the viscosity-dependence of the normalized maximal diameter as shown in Figure 3.7.

(ii) **Semi-empirical model:** To better account for the viscosity dependence of the maximal expansion, we still use a similar approach based on energy conservation and consider that a viscous sheet expands as an inviscid one but with an effective impact velocity v_{eff} reduced compared to the real one. This velocity is assumed to be the velocity at the edge of the target and is reduced compared to the initial velocity of the sheet due to viscous dissipation on the surface of the target. Instead of using a theoretical model for v_{eff} as above (Equation 3.4), we here measure v_{eff} directly as the time derivative at short time of d the diameter of the sheet: $v_{\text{eff}} = \frac{1}{2} \frac{\partial d}{\partial t} \Big|_{t \rightarrow 0}$. We show in Figure 3.6a v_{eff} for all the viscous samples and viscoelastic samples with $De \ll 1$. Data for all samples reasonably collapse and show a continuous decrease with the sample viscosity. We find that a linear dependence of v_{eff} with $\sqrt{\eta_0}$ accounts fairly well for the dependence of v_{eff} with the sample viscosity (Figure 3.6b).

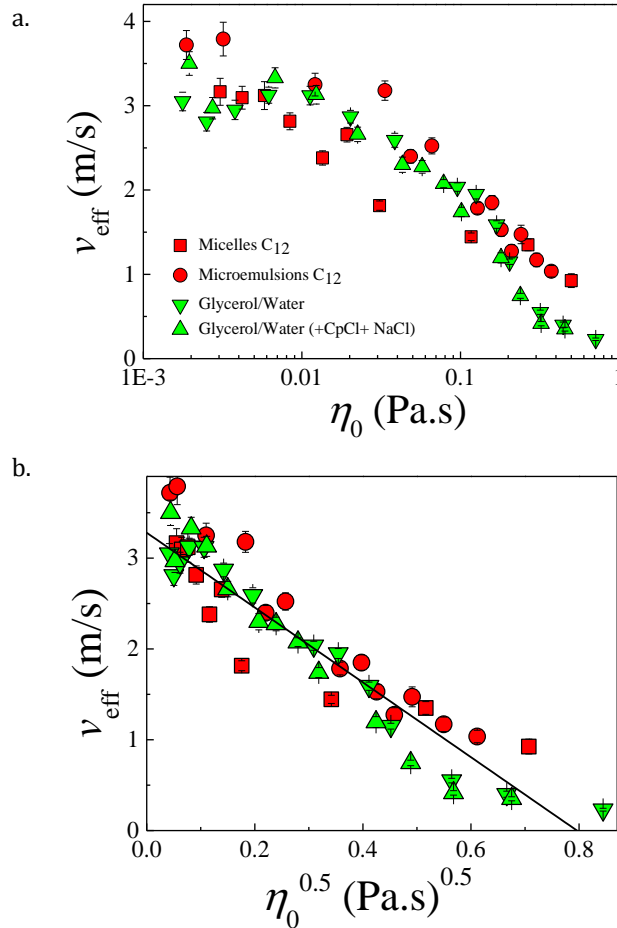


Figure 3.6: (a) Effective velocity of the sheet measured at the edge of the target, v_{eff} as a function of the zero-shear viscosity η_0 in lin-log scale, for the viscous samples and the viscoelastic samples for which $De \ll 1$. (b) Same data plotted as a function of $\sqrt{\eta_0}$ in a lin-lin scale.

Note that other simple functional forms, as for instance a linear dependence with the viscosity or the theoretical expectation (Equation 3.4), are significantly less good. A fit of the experimental data with the functional form $v_{\text{eff}} = v^*(1 - \lambda\sqrt{\eta_0})$ yields $v^* = (3.2 \pm 0.1)$ m/s and $\lambda = 1.24 \pm 0.10$ (Pa.s)^{-0.5}. Note that v^* is 20 % smaller than the impact velocity ($v_0 = 4$ m/s), indicating that some dissipation also occurs in the inviscid case. A possible reason could also be the conjoined co-axial cylinder to the solid target to limit the bell effect [Clanet 2002]. From Equation 3.3 one therefore predicts:

$$\tilde{d} = v_{\text{eff}}/v^* = 1 - \lambda\sqrt{\eta_0} \quad (3.11)$$

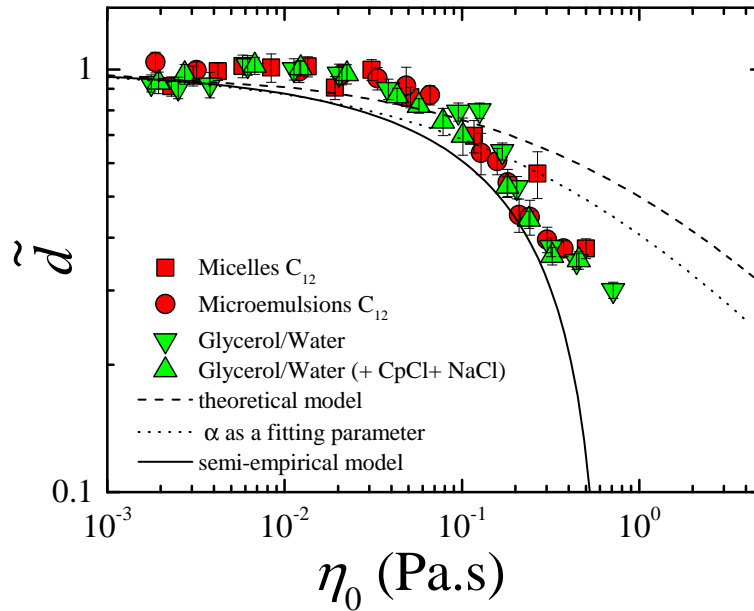


Figure 3.7: Maximum diameter (normalized by its value at low viscosity), as a function of zero-shear viscosity for viscous samples and viscoelastic samples for which $De \ll 1$, as indicated in the legend. The symbols are data points and the lines are theoretical and semi-empirical modeling.

We show in Figure 3.7 that Equation 3.11 provides a very good agreement of the experimental data, with the numerical value of λ extracted from the fit of the effective velocity (Figure 3.7). In spite of its simplicity, we find that the semi-empirical approach provides a better agreement of the experimental data, especially, in the regime of relatively high viscosity where the theoretical model fails. We also note that $1 - \lambda\sqrt{\eta_0}$ in Equation 3.11 is the limit of $1/(1 + \lambda\sqrt{\eta_0})$ for $\lambda^2\eta_0 \ll 1$, a functional form that corresponds to the theoretical model (Equation 3.9).

(iii) **Discussion on expected role of shear and extensional viscosity:** To confirm the crucial role played by the viscous dissipation on the surface of the small target,

we have performed an experiment where we expect to suppress any dissipation on a solid surface. To do so, a drop is impacted (with the same velocity as for previous experiments on a solid target) on a surface covered by a thin layer of liquid nitrogen, allowing the sheet to float above a gaseous cushion. Comparative images of the sheets at maximal expansion are shown in Figure 3.8 for the same mixture of water and glycerol with a zero-shear viscosity of 128 mPa.s, $d_{\max} = 16.3$ mm when the drop is impacting on the small solid target, whereas d_{\max} reaches 27.3 mm on nitrogen. This expansion is comparable to that of a fluid with a very low Newtonian viscosity, demonstrating that viscous dissipation on the solid target governs the expansion dynamics.

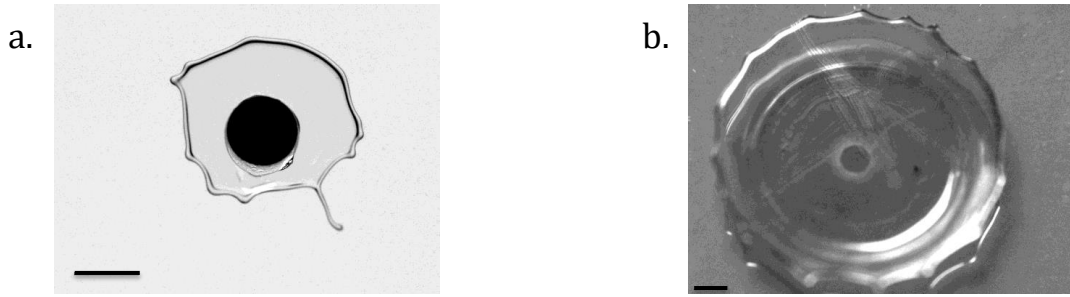


Figure 3.8: Images of viscous sheet taken at the maximal expansion for a drop of water/glycerol mixture with zero-shear viscosity 128 mPa.s impacting at the same velocity (a) a small solid target and (b) a silicon wafer covered with a thin layer of liquid nitrogen. The scale bars are (a) 6 mm and (b) 3 mm.

More quantitatively, we can evaluate and compare the shear viscous dissipation that occurs in the boundary layer at the interface between the surface of the solid target and the liquid sheet and the extensional viscous dissipation that occurs when sheet expands in air. We therefore compare at a scaling level the magnitudes of the viscous dissipation energies per unit volume (V_{drop}) due to expansion of sheet in air ($E_{\text{extension}}$) and due to shearing stresses on solid target (E_{shear}). Dissipation energy per unit volume due to the radial expansion of the sheet in air can be evaluated on the basis of extensional stresses which develop as a result of expansion and can be written as:

$$\frac{E_{\text{extension}}}{V_{\text{drop}}} \simeq \eta_{be} \left(\frac{1}{t_{\max}} \right) \left(\frac{(d_{\max} - d_o)^2}{d_o d_{\max}} \right) \quad (3.12)$$

Here, η_{be} is the biaxial extensional viscosity and for a purely viscous fluid $\eta_{be} = 6\eta_0$ [Macosko 1994]. The derivation of Equation 3.12 is given in detail in Appendix B.

On the other hand energy dissipation per unit volume due to the flow driven by shearing stresses (on small solid target) can be written as:

$$\frac{E_{\text{shear}}}{V_{\text{drop}}} \simeq \eta_0 t_{\max} \left(\frac{v_o}{l} \right)^2 \quad (3.13)$$

here, $l = \min(h, \delta)$ is the thickness over which the liquid sheet is sheared. In our experiments $\delta < h$, thus we consider viscous boundary layer δ to calculate the E_{shear} .

$$\frac{E_{\text{shear}}}{V_{\text{drop}}} = \eta_0 t_{\text{max}} \left(\frac{v_o}{\delta} \right)^2 \quad (3.14)$$

with $\delta \approx \sqrt{\frac{\eta_0 d_t}{2\rho v_o}}$. Using this expression in Equation 3.14, we find that $\frac{E_{\text{shear}}}{V_{\text{drop}}}$ is independent of the zero shear viscosity (η_0) while energy due to the extensional stresses is proportional to the zero shear viscosity.

We consider the case of liquid sheets produced by glycerol/water mixtures at different viscosities. We plot in Figure 3.9 the energy dissipation per unit volume E due to shear stresses over the target and the elongational stresses because of the extension of the liquid sheet. We find that in the whole range of zero shear viscosity investigated (1 – 1000 mPa.s) the dissipation due to an extension of the sheet (in air) is much lower than the dissipation, occurring due to the boundary layer. This simple calculation confirms that the dissipation essentially occurs on the solid target.

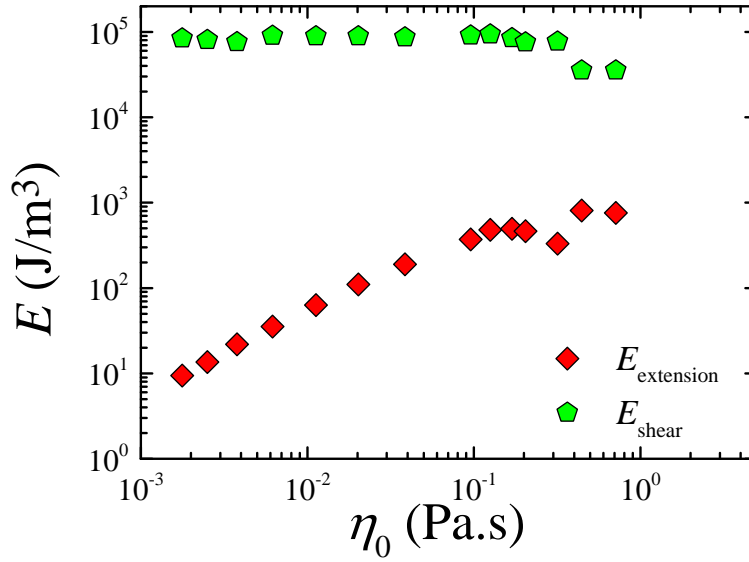


Figure 3.9: Energy dissipation per unit volume as a function of zero shear viscosity for glycerol-water mixtures.

3.3.2 Dynamics of liquid sheet: $De \approx 1$ and $De \gg 1$

In the high Deborah number regime, we observe that the sheets expand much more than viscous sheets or sheets produced with viscoelastic samples with a short relaxation

time. Remarkably, we find that up to zero-shear viscosity of 20 Pa.s, the maximal expansion of the sheet does not significantly decrease compared to the case of inviscid fluids, whereas for the other samples (C_{12} -based micelles and microemulsions, and C_{18} -based micelle), the maximum diameter of the sheet expansion is smaller than the target diameter ($\tilde{d} < 0.25$). Moreover, we note that quantitatively comparable results are obtained for regular microemulsions and for dyed ones.

Interestingly, the behavior of C_{18} -based micelles for which the Deborah number is of the order of 1 is intermediate between that of the C_{12} -based samples ($De \ll 1$), and that of the C_{18} -based microemulsions ($De \gg 1$), confirming a crucial role of the coupling between the characteristic relaxation time of the samples and the life-time of the sheet. Figure 3.10 shows the maximum diameter normalized by its value at small viscosity (the inviscid case) as a function of zero shear viscosity (bottom x-axis) and Ohnesorge number (top x-axis).

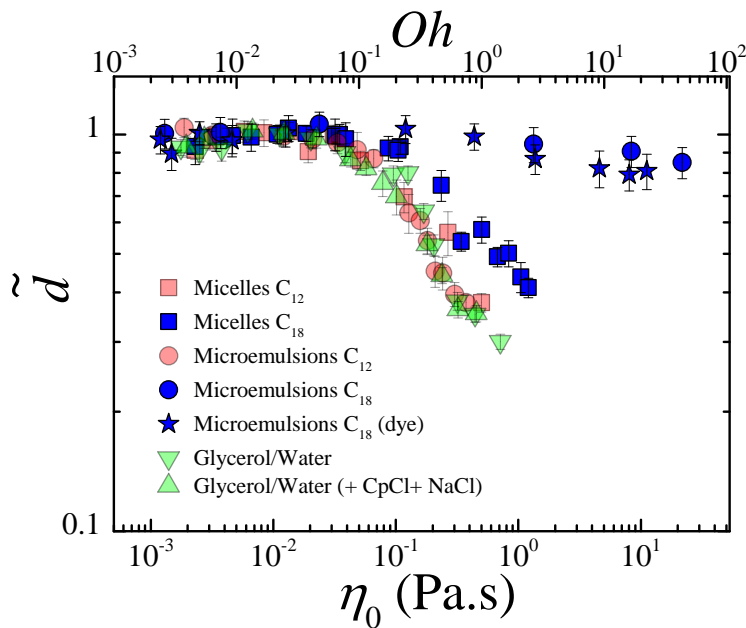


Figure 3.10: Maximum diameter (normalized by its value at low viscosity), as a function of zero-shear viscosity (bottom x axis), and Ohnesorge number (top x axis).

Qualitatively, viscoelastic samples with characteristic times much larger than the life-time of the sheet, as the C_{18} -based microemulsions, behave in a drastically different fashion. Figure 3.11 both dyed and undyed samples, cracks and holes invade the interior of the sheets, while the sheet maintains the integrity of its contour. Hence, it is tempting to associate the fracture process that occurs in extension and shear for C_{18} -based microemulsion samples to the cracks observed when the sheet expands.

Our observations nevertheless clearly emphasize that the elastic contribution in the viscoelasticity plays a crucial role in the overall way a sheet expands and are reminis-

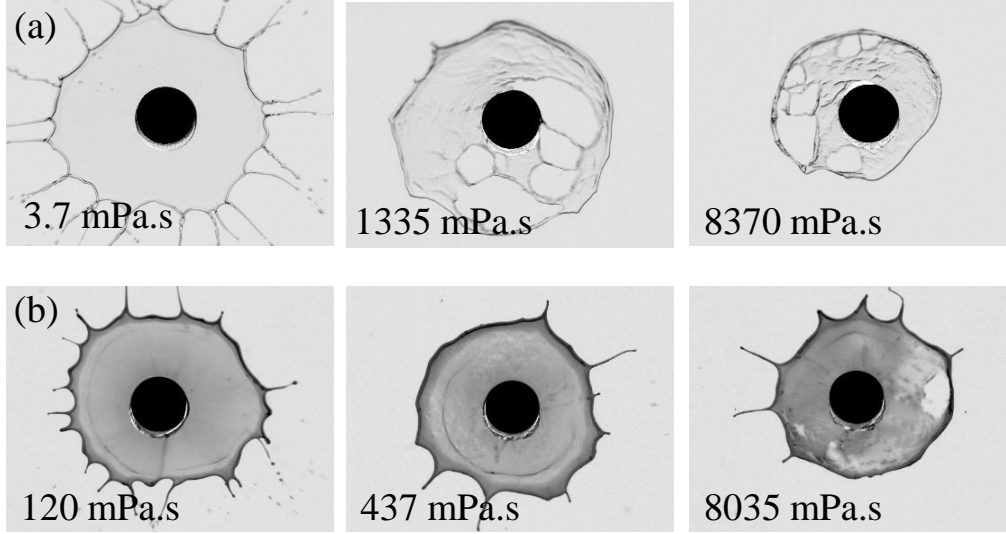


Figure 3.11: Snapshots of sheets made of C_{18} -based microemulsions (a) without dye, (b) with dye. Images are taken at the maximal expansion of the sheets. All samples are above the percolation threshold, except the ones with lower zero-shear viscosity (3.7 mPa.s and 120 mPa.s).

cent of the rupture processes of Savart sheets observed upon collision of viscoelastic jets [Miller 2005]. Note that, in sharp contrast, in the low number Deborah regime, in which the viscoelastic sheet behaves as a viscous sheet, the sheet expands in a rather smooth way and always preserves its integrity (Figure 3.3). Our experimental observations show a clear link between the capability of a sheet to expand and the linear rheological properties of the fluid for samples with zero-shear viscosity larger than ~ 30 mPa.s. A simple yet quantitative way to account for the samples viscoelasticity is to consider the dynamic viscosity. Note that this approach is similar to that followed by de Gennes to describe the fracture dissipation process for complex fluids in the framework of the trumpet model [De Gennes 1988, De Gennes 1996, Saulnier 2004, Tabuteau 2011].

For a Maxwell fluid, the dynamic viscosity reads as:

$$\eta' = G''(\omega)/\omega = \frac{G_0\tau}{1+(\omega\tau)^2}$$

Taking as characteristic time, t_{\max} , the time at which the sheet reaches its maximal expansion, we can deduce:

$$\eta' = \frac{\eta_0}{1+De^2}$$

with $De = \tau/t_{\max}$. Interestingly, if the data of the maximal expansion are plotted as a function of η' instead of η_0 we find that the data for C_{18} -based micelles (for which $De \approx 1$) and C_{18} -based microemulsions (for which $De \gg 1$) almost collapse with the

data gathered for Newtonian fluids and C_{12} -based samples (Figure 3.12). This suggests that the deviation from the Newtonian behavior, which is observed for viscoelastic samples whose relaxation time is comparable to, or larger than, the life-time of the sheet, can be accounted for by the sample linear viscoelasticity. For C_{18} -based microemulsions, the characteristic relaxation time being much larger than the life-time of the sheet ($De \gg 1$), the dynamic viscosity is much smaller than the zero-shear viscosity, indicating that dissipation is negligible, and the samples behave as almost purely elastic. Based on previous experiments in different experimental conditions, we know that, for those kinds of samples, fracture processes occur [Ligoure 2013]. Cracks have indeed been observed in the gap of a shear cell (pure shear flow [Tabuteau 2009]), in a pendant drop experiment (pure extensional flow [Tabuteau 2009]) and in Hele-Shaw cell (complex flow involving both shear and extensional flows [Mora 2010a, Foyart 2013]). Fracture occurs when the sample is deformed at rates larger than the inverse of its viscoelastic relaxation time.

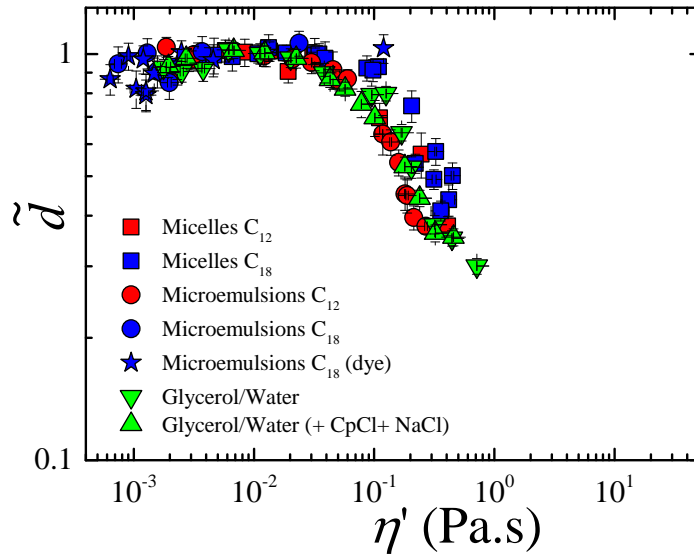


Figure 3.12: Same data as in figure 3.10 but plotted as a function of the dynamic viscosity.

It is therefore instructive to evaluate the deformation rates involved upon the sheet expansion. The extension rate of the fluid upon the expansion of the sheet, $\dot{\epsilon}$, can be computed as $\dot{\epsilon} = \frac{1}{d} \frac{\partial d}{\partial t}$. Note that at short times, $\dot{\epsilon} = \frac{2}{d_t} v_{\text{eff}}$, with $d_t = 6$ mm the target diameter, and v_{eff} the effective velocity determined above (Figure 3.6), yielding a rate $\dot{\epsilon} \approx 1000 \text{ s}^{-1}$ at short time that steadily decreases with time until vanishing when the sheet reaches its maximal expansion. We can also evaluate the shear rate involved as the drop hits the target. A simple estimation, by considering that shear flow only occurs when the fluid interacts with the solid surface, gives $\dot{\gamma} \approx \frac{v_{\text{eff}}}{\delta}$, with δ the thickness over which viscous dissipation takes place (Equation 3.6). For C_{18} -based microemulsions above

percolation, $v_{\text{eff}} \approx 3.5$ m/s, and $\dot{\gamma}$ is in the range (1000 – 10000) s⁻¹. Hence, the rates involved are systematically larger than the inverse of the relaxation time (τ is in the range (0.1 – 1) s, Figure 3.1b), suggesting that fracture processes may occur.

Cracks in the viscoelastic sheet (C₁₈-based microemulsion) will be discussed more in detail in Chapter 5

3.4 Conclusion

We have investigated how viscous and viscoelastic sheets resulting from the impact of a droplet on a small target of size comparable to that of the droplets expand in air. We have found that, for viscous droplets and for small Ohnesorge number Oh , the maximal expansion of the sheet is governed by the balance between inertia and surface tension, whereas for higher Oh viscous dissipation plays an important role. We have used a simple modeling of the sheet expansion where inertia, surface tension, and viscosity are taken into account to compute an energy balance. One of the main ingredients is that dissipation occurs in the viscous boundary layer at the interface between the surface of the target and the liquid. Accordingly, we have directly measured the sheet velocity at the edge of the target and relate this velocity to the maximal expansion of the sheet. The quantitative agreement between the model and the experiments shows that the dissipation mainly occurs on the small surface of the target and that, when the sheet freely expands in air, extensional viscous dissipation is negligible, in agreement with an experiment performed with a viscous sample freely expanding on a gaseous nitrogen cushion.

In addition, we have also investigated model complex fluids that behave as Maxwell fluids, characterized by a plateau modulus G_0 and a unique relaxation time τ . We have been able to independently and finely tune τ and the zero-shear viscosity $G_0\tau$, allowing us to decouple the effect of the viscosity and elasticity on the spreading of viscoelastic sheets. Our experiments have evidenced a key role of the adimensional Deborah De number defined as the ratio between τ and the typical lifetime of the sheet. When $De \ll 1$, we find that the Maxwell fluids behave as simple Newtonian fluids with zero-shear viscosity $G_0\tau$. Samples for which $De > 1$, the departure from the Newtonian case can be accounted for by the sample viscoelasticity. Interestingly, the dynamics of viscoelastic sheets produced with Maxwell fluids whose characteristic relaxation time is much larger than the life time of the sheet ($De \gg 1$) drastically differ from those of other samples. The sheet expands much more than viscous sheets with comparable zero shear viscosity, due to reduced viscous dissipation. In addition, upon expansion the sheet is highly heterogeneous and displays cracks and holes, revealing the sample elasticity. Our results therefore show the interplay between the relaxation time of the viscoelastic fluid and the characteristic time of the experiments, as could also be observed in other experimental conditions like the dispensing of drop from a syringe with a controlled flow rate [Clasen 2012]. The experimental set-up, originally designed by M. Vignes-Adler and

collaborators and subsequently modified by Villermaux and Bossa to limit the bell effect, provides an unusual yet interesting configuration for testing the rheology of complex fluids as it involves large deformations and highly extensional flows on very short time scales.

Unified Description of the Resilient Behavior of Elastic Beads and Liquid Drops on Impacting Surfaces

Contents

4.1	Experimental samples and techniques	65
4.2	Dynamics of elastic and liquid sheets	66
4.2.1	Experimental observations	66
4.2.2	Quantitative analysis	68
4.3	Conclusion	78

In this chapter, we study the dynamics of freely expanding sheets formed by soft spherical elastic beads of millimeter size and elastic modulus in the range (10 Pa - 700 Pa). The sheets are produced by impacting the elastic beads on a silicon wafer covered with a thin layer of liquid nitrogen, thanks to the inverse Leidenfrost effect. The liquid nitrogen layer suppresses shear dissipation at the bead-surface interface due to the formation of a vapor cushion on impact. At high impact velocity, the elastic bead deforms into a flattened disc like a pancake. For analogy, we also perform similar experiments with liquid droplets with various surface tensions. We measure the maximal deformed size of the sheet d_{\max} , for several impact velocities. The experiments reveal a universal scaling behavior of d_{\max} with impact velocity for elastic beads and liquid drops. Moreover, we show that, the dynamics of the system mimics a conventional spring-mass system with a stiffness given by a combination of surface tension and bulk elasticity demonstrating the absence of viscous dissipation.

4.1 Experimental samples and techniques

Soft elastic beads are prepared by the polymerization of acrylamide and bis-acrylamide in the presence of initiators in water. To tune the elasticity of the beads, the concentrations of acrylamide and bis-acrylamide are varied. The preparation of the elastic beads is explained in details in section 2.1.2. To compare the results obtained with the beads

to those obtained with liquid drops we have performed experiments with pure water and ethanol-water mixtures. All the elastic beads and liquid drops have a same diameter $d_o = 3.7$ mm.

The experimental set-up to measure the elastic modulus is described in section 2.2.3. In brief, a rigid sphere is indented in the gel and the force along with the indentation depth are measured to determine the shear modulus G_0 of the gel [Hertz 1895, Johnson 1987]. The elastic modulus of beads is varied between 10 Pa and 740 Pa. The surface tension γ of the elastic beads is taken to be equal to that of water 72 mN/m [Chakrabarti 2013]. For liquid drops we use samples with various surface tensions (72 mN/s, 50 mN/m and 32 mN/s) by changing the concentration of ethanol in water as explained in section 2.1.3.

Thin sheets are produced by impacting elastic beads and liquid drops on a silicon wafer covered with a thin layer of liquid nitrogen. We vary the impact velocity v_o in the range (1 m/s - 5 m/s.) The time series of the images of the sheet are recorded using a fast camera as detailed in section 2.3.2. The images are analyzed using the technique explained in section 2.4.

4.2 Dynamics of elastic and liquid sheets

4.2.1 Experimental observations

We have shown the advantage of using the inverse Leidenfrost effect over the impact on solid target in chapter 2. This allows one to study the dynamics of freely expanding sheet of elastic/or liquid in the absence of shear viscous dissipation. When the elastic bead or liquid drop impacts the substrate the inertial forces causes it to spread radially. On impacting the silicon wafer covered with a thin layer of liquid nitrogen, a local vapor cushion of nitrogen gas forms which thermally insulates the expanding sheet from freezing. This evaporating vapor from liquid nitrogen moves radially outwards which induces the slip conditions and reduces the viscous dissipation due to the non-wetting condition between the substrate and the expanding sheet thus enhancing the expansion of the sheet [Tran 2012, Antonini 2013]. Figure 4.1 shows the time evolution of sheet expansion and retraction on impacting the silicon wafer for elastic bead $G_0 = 35$ Pa and ethanol-water mixture $\gamma = 50$ mN/m. Time at the impact is taken as $t = 0$. Unlike the elastic beads, we see the formation of secondary droplets in the case of ethanol-water mixture because of the rim destabilization.

Figure 4.2 shows the snapshot at the maximum expansion of elastic beads with different elastic moduli G_0 but at fixed impact velocity ($v_o = 4.35$ m/s). As G_0 increases, the maximum expansion of the sheet decreases. Figure 4.3 shows the snapshots at the maximum expansion of sheets produced with the elastic bead of elastic modulus $G_0 = 11$

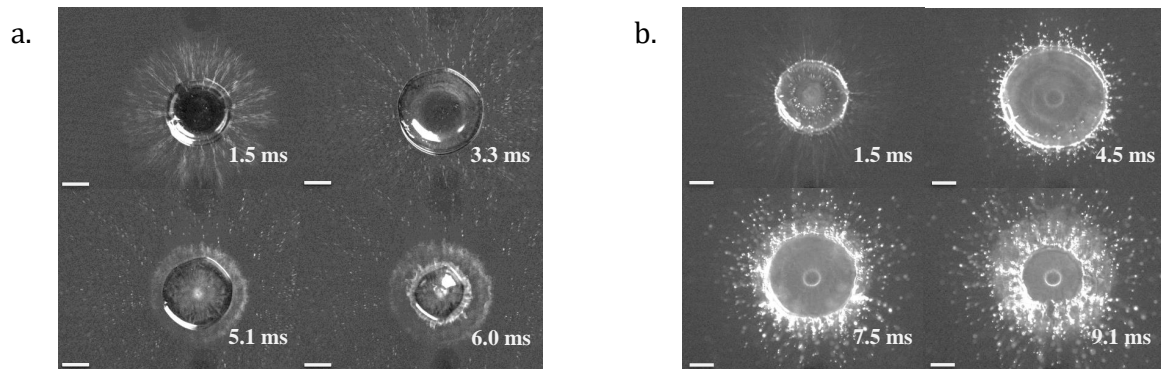


Figure 4.1: Images of the sheet at different times at a fixed impact velocity $v_o = 4.35$ m/s for (a) an elastic bead with shear modulus $G_0 = 35$ Pa and (b) an ethanol-water mixture with surface tension $\gamma = 50$ mN/s. The scales bars are 6 mm.

Pa at different impact velocities. The maximum expansion of the sheet increases with increasing impact velocity.

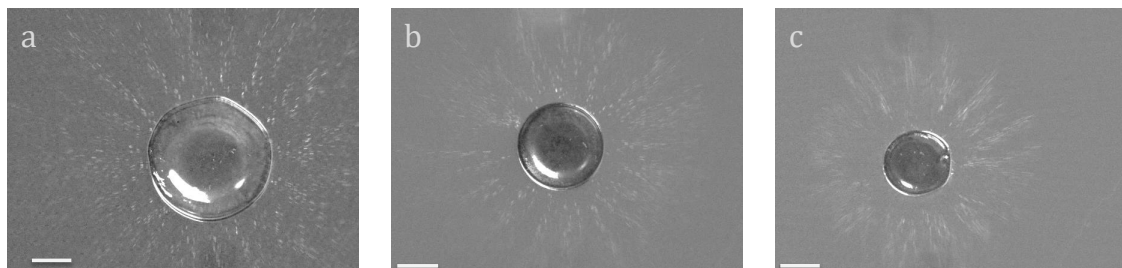


Figure 4.2: Maximum expansion of sheet produced by impacting with a fixed velocity $v_o = 4.35$ m/s for elastic beads with elastic modulus (a) 35 Pa (b) 118 Pa and (c) 334 Pa. The scale bars are 6 mm.

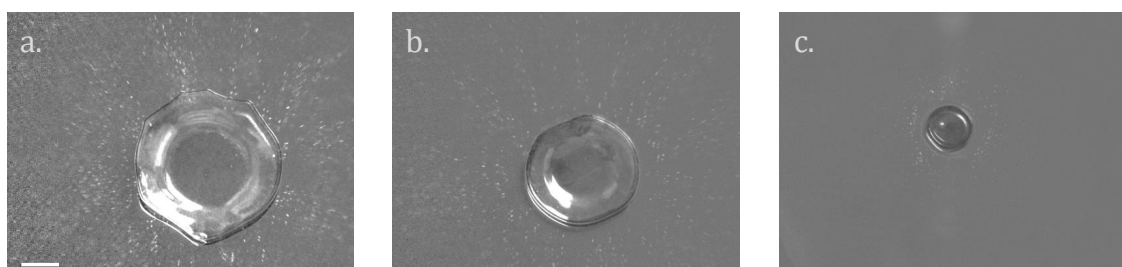


Figure 4.3: Maximum expansion of a sheet produced by impacting an elastic bead of shear modulus $G_0 = 11$ Pa at different impact velocities (a) 4.6 m/s Pa (b) 3.4 m/s and (c) 1 m/s. The scale bars are 6 mm.

4.2.2 Quantitative analysis

4.2.2a Maximum expansion of elastic beads

Here, we examine the case of a large deformation of an elastic bead after the impact on solid surface commonly known as pancake regime [Tanaka 2003, Tanaka 2005]. For a quantitative analysis, we consider that the elastic bead behaves as a neo-Hookean solid and undergoes deformations as shown in Figure 4.4.

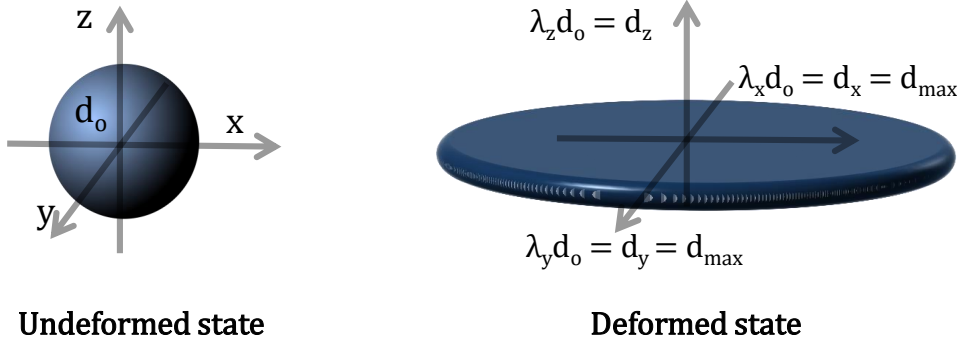


Figure 4.4: Scheme to show the affine deformation of an elastic bead on impacting the solid substrate..

The elastic energy density ξ is given by [Ogden 1997]:

$$\xi = \frac{1}{2}G_0 (\lambda_x^2 + \lambda_y^2 + \lambda_z^2 - 3) \quad (4.1)$$

Here G_0 is the elastic (shear) modulus, λ_x , λ_y and λ_z are the stretching ratios along the three principle axes. For incompressible materials: $\lambda_x \lambda_y \lambda_z = 1$ and in our case we are looking at equibiaxial deformation thus $\lambda_x = \lambda_y = \lambda$. This gives $\lambda_z = \frac{1}{\lambda^2}$. Experimentally, we measure the maximum diameter reached by the sheet d_{max} and thus by definition $\lambda = d_{max}/d_0$. Equation 4.1 reduces to:

$$\xi = \frac{1}{2}G_0(2\lambda^2 + \frac{1}{\lambda^4} - 3) \quad (4.2)$$

Assuming no viscous dissipation, we can write the energy balance equation in terms of initial kinetic energy and elastic energy:

$$\frac{1}{2}mv_o^2 \approx V_{bead}\xi \quad (4.3)$$

In the case of large deformations ($\lambda \gg 1$), $\xi \approx G_0 \lambda^2$ and thus Equation 4.3 is given by:

$$\frac{1}{2} m v_o^2 \approx V_{\text{bead}} G_0 \lambda^2 \quad (4.4)$$

Here m is the mass of the bead $m = \rho V_{\text{bead}}$ with V_{bead} the volume of the bead and ρ the density. Simplifying Equation 4.4 gives the dependence of the maximal spread factor on the Mach number M [Joseph 2013], defined as the ratio of impact velocity v_o to the velocity of transverse sound waves in an elastic medium $U_S = \sqrt{G_0/\rho}$ [Kolsky 1963].

$$\lambda \approx \frac{1}{\sqrt{2}} \frac{v_o}{\sqrt{\frac{G_0}{\rho}}} \approx \frac{1}{\sqrt{2}} M \quad (4.5)$$

In Figure 4.5 we plot the maximal spread factor λ as a function of Mach number M for all the experimental data obtained from elastic beads having different elastic moduli and impact velocities. In our experiments M varies between 2 and 45 and λ between 1.6 and 6.5.

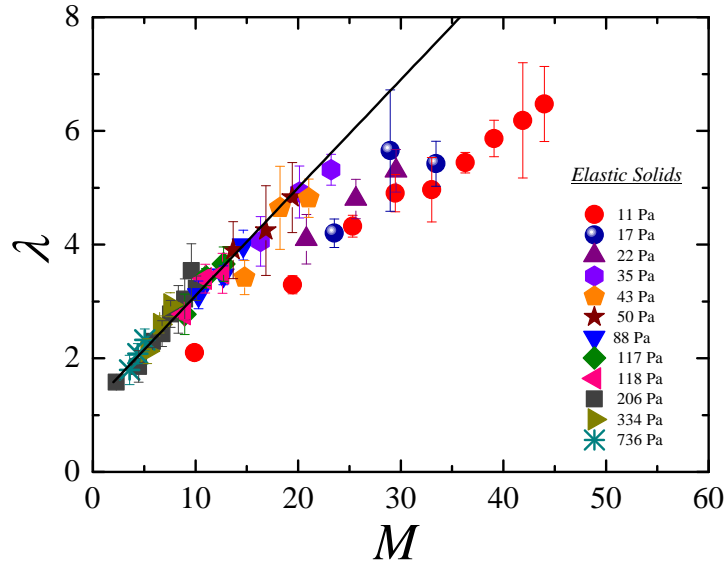


Figure 4.5: Maximal spread factor λ as a function of Mach number M . Symbols are the experimental data points and the solid line is a linear fit of the data at small M to guide the deviation of data above $M \simeq 20$.

We observe that there exists a threshold value $G_{0c} \simeq 35$ Pa above which all the experimental data collapse on a straight line in accordance with the simple prediction of Equation 4.5. We find that λ increases continuously with M . The data are fitted with a

linear equation $a + bx$, yielding a slope $b = 0.2$ while Equation 4.5 predicts a slope equal to 0.7 and an intercept $a = 1.2$. We note that for v_o tending to zero λ should tend to one and not to 0 as predicted by Equation 4.5, because this asymptotic balance equation is not valid for λ close to 1.

On the contrary, for ultra-soft elastic beads ($G_0 \leq G_{0c}$), the expected scaling behavior does not hold anymore. This shows that, for ultra soft elastic beads, we miss another contribution to the elastic energy of the bead in the deformed state, since Equation 4.5 overestimates the stretching of the elastic sheet. To explain the deviation from the classical theoretical expression, for ultra-soft elastic beads, the elastic contribution due to surface tension has to be taken into account along with the bulk elasticity. In our experiments, the kinetic energy of the bead or drop is much higher than the initial surface energy of the bead or drop in the undeformed state. To ensure that, we can equate the kinetic and surface energy of the bead or drop to calculate minimum velocity below which the initial surface energy of the bead or drop cannot be neglected in the energy balance $v_{\min} = \sqrt{\frac{12\gamma}{\rho d_o}}$. Since, the diameter of the bead or drop ($d_o = 3.7$ mm) is fixed and the sample density varies between 1000 kg/m³ and 950 kg/m³, it is easy to inspect for different values of surface tension, v_{\min} varies between 0.5 m/s and 0.3 m/s. Clearly, we are always above this minimal value: the minimum impact velocity in our experiments is 1 m/s. Hence, for quantitative analysis, we can neglect the surface energy of the undeformed bead or drop in an energy balance equation. Thus we can rewrite Equation 4.4 by including the surface energy at maximum expansion $\frac{1}{2}\pi\gamma d_{\max}^2$ in the limit of large deformations:

$$\frac{1}{2}mv_o^2 \approx \frac{1}{2}\pi\gamma d_{\max}^2 + V_{\text{bead}}G_0\lambda^2 \quad (4.6)$$

Simplifying and rearranging Equation 4.6 we obtain,

$$\frac{1}{2}v_o^2 = \frac{3\gamma}{\rho d_o}\lambda^2 + \frac{G_0}{\rho}\lambda^2 \quad (4.7)$$

Considering, $U_S = \sqrt{\frac{G_0}{\rho}}$ as the velocity of transverse sound waves in an elastic medium and $U_L = \sqrt{\frac{3\gamma}{\rho d_o}}$ as the typical velocity of the free oscillations of a drop called Rayleigh velocity [Rayleigh 1879]. Equation 4.7 reduces to:

$$\lambda \approx \frac{1}{\sqrt{2}} \frac{v_o}{\sqrt{U_L^2 + U_S^2}} \approx \frac{1}{\sqrt{2}} \frac{v_o}{U^*} \quad (4.8)$$

Here $U^* = \sqrt{U_L^2 + U_S^2}$ is a typical velocity of the material for generalized elastic deformations. Equation 4.8 demonstrates that λ depends on two elastic contributions, one from the surface tension and the second one from the bulk elasticity of the elastic gel. If

$U_S \gg U_L$, the surface tension effects can be neglected and we observe that the expansion of an elastic bead is purely dominated by its elastic modulus, as observed by Y. Tanaka *et al* [Tanaka 2003]. On the other hand, interestingly, when $U_S \ll U_L$, the bulk elasticity is negligible in comparison to surface elasticity and we recover the prediction of D. Richard *et al* [Richard 2002] for a simple liquid. In the present experimental study, both bulk and surface energies may be important to explain the expansion of elastic sheets. To quantitatively compare the two elastic energies, we define a characteristic elastocapillary length $l_{ec} = 3\gamma/G_0$ that characterizes the relative importance of surface elasticity with respect to the bulk elasticity [Mora 2010b, Jagota 2012]. In terms of l_{ec} Equation 4.8 can be expressed as:

$$\lambda \approx \frac{1}{\sqrt{2}} \frac{v_o}{U_L} \sqrt{\frac{1}{1 + \left(\frac{d_o}{l_{ec}}\right)^2}} \quad (4.9)$$

For our experimental system, we have fixed $d_o = 3.7$ mm and for elastic beads, we have taken $\gamma = 72$ mN/m. Figure 4.6 shows a "state diagram" in the space (characteristic length, elastic modulus) of the material. We can observe that for $l_{ec} < d_o$ ($G_0 > 60$ Pa) bulk elasticity dominates and for $l_{ec} > d_o$ ($G_0 < 52$ Pa) it is the surface elasticity which dominates. If the two lengths are comparable, bulk and surface elasticity are expected to be important to account for the expansion of elastic beads. We have investigated all three regimes in the case of ultra soft elastic beads.

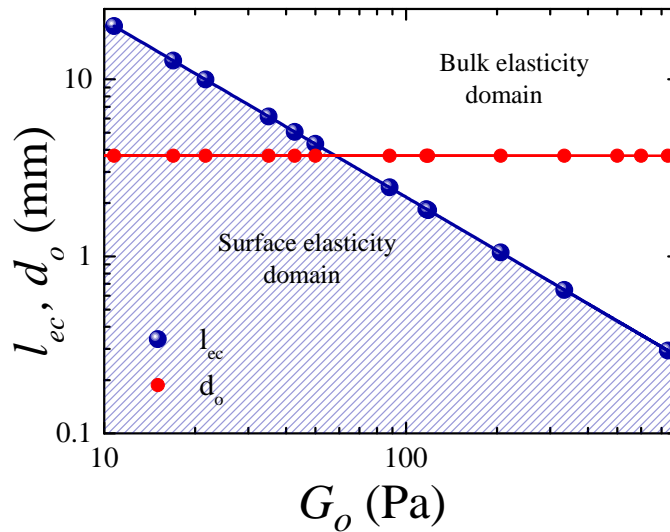


Figure 4.6: Schematic phase diagram of length scale l as a function of G_0 . The symbols are the experimental points. Highlighted area shows the region dominated by surface elasticity and white region by the bulk elasticity.

To emphasize the role of two contributions of elasticity we first plot the maximal spread factor λ as a function of reduced impact velocities for two elastic beads ($G_0 = 11$ Pa, 206 Pa) in Figure 4.7. In the inset a of Figure 4.7 λ is plotted as a function of v_o/U_S taking only bulk elasticity into account. We see that the experimental data do not collapse and the deformation of the elastic bead with $G_0 = 11$ Pa increases more slowly than the deformation of a bead with $G_0 = 206$ Pa with the reduced velocity v_o/U_S . Similarly, if we just take the elasticity due to surface tension into account we observe that the two experimental data sets do not coincide as well (inset b.). This is consistent with the fact, for elastic bead with shear modulus $G_0 = 11$ Pa, $l_{ec} = 19$ mm $\gg d_o = 3.7$ mm. So, in addition to bulk elasticity, one has to take the effect of the surface tension into account for analyzing the maximal deformation of the sheet. We see in Figure 4.7 (main plot) when λ is plotted against v_o/U^* accounting for "generalized elastic deformations", all the data collapse on a single curve.

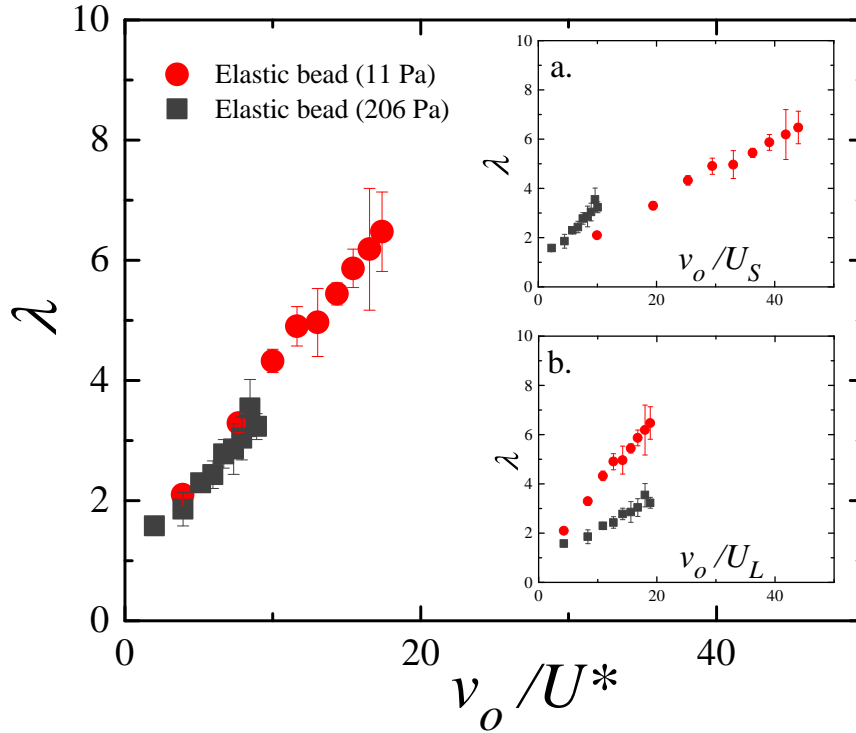


Figure 4.7: Maximal spread factor $\lambda = d_{\max}/d_o$ as a function of the reduced impact velocity taking respectively bulk and surface energy (main plot,) only bulk elasticity (inset a) and only surface elasticity (inset b) into account.

Figure 4.8 shows the maximal spread factor λ as a function of v_o/U^* for all the elastic beads with distinct elastic modulus as indicated in the legend. The solid line is a linear fit of the experimental data yielding a slope $b \approx 0.35$ and $a \approx 0.6$. Theoretical expression

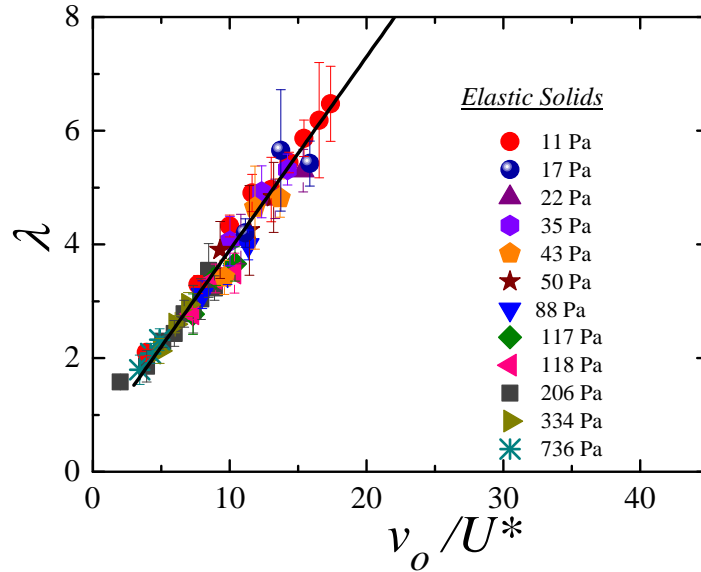


Figure 4.8: Maximal spread factor λ as a function of v_o/U^* where v_o is the impact velocity and U^* is the velocity of generalized elastic deformations (Equation 4.8). The solid symbols are experimental data points for elastic beads with shear modulus as indicated in the legend. The solid line is a linear fit.

predicts the slope equal to 0.7 which is comparable to the slope obtained experimentally. Equation 4.8 predicts for $v_o = 0$, the deformation $\lambda = 0$. This is nonphysical, as Equation 4.8 is only valid for large deformation ($\lambda \gg 1$) and not applicable at very small velocities. Hence, Equation 4.8 should work well only in case of large deformation; however, and surprisingly, this asymptotic linear relation describes the experimental results well even for moderate deformations.

4.2.2b Maximum expansion of elastic beads and liquid drops

Experiments are also performed with Newtonian liquid drops. We use pure water and ethanol-water mixtures to investigate the influence of surface tension, for Newtonian liquids $U_S = 0$ and $U^* = U_L$. We find that all the experimental data from elastic solids and liquids collapse on a single curve (see Fig 4.9). This also establishes a universal scaling behavior for the maximum deformation of both elastic beads and liquid drops under the conditions of negligible viscous dissipation provided the bulk and surface elasticity are correctly taken into account. In spite of neat universal scaling, we find that at high impact velocities for liquids, data tends to deviate from the prediction especially for the liquid with the smallest surface tension $\gamma = 32$ mN/m. This can be attributed to splashing (prompt or corona) and to the ejection of secondary droplets from the destabilization of the rim during the expansion of the sheet and consequently loss of volume in case of liquids [Mundo 1995, Rioboo 2001].

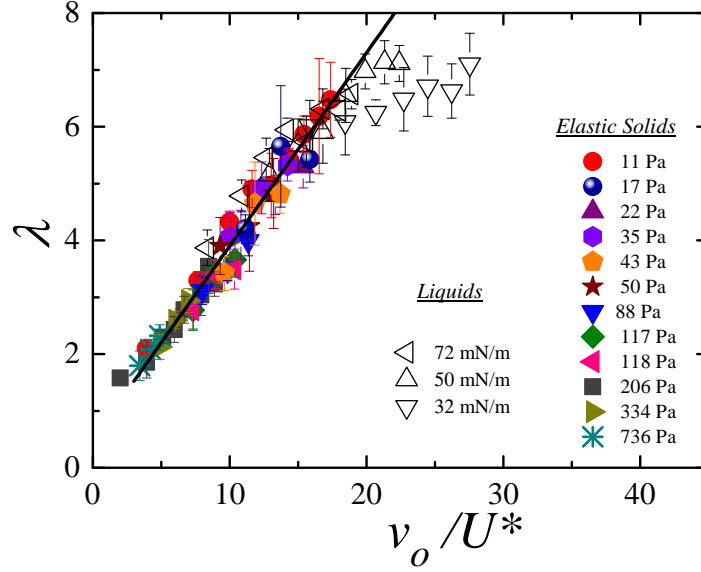


Figure 4.9: Maximal spread factor λ as a function of v_o/U^* where v_o is the impact velocity and U^* is the velocity of generalized elastic deformations (Equation 4.8). The solid symbols are experimental data points for gel beads and empty symbols for liquid droplets as indicated in the legend. The solid line is a linear fit.

4.2.2c Dynamics of expansion

We now describe the full dynamics of the sheet expansion and retraction that can be approximated as a simple harmonic motion. Following the approach of A.L. Bianco *et al* [Bianco 2006], we model the expansion of an elastic sheet as the dynamics of one-dimensional zero-length spring with a mass m and stiffness k . With this elementary approach, we can write the mechanical energy of the sheet expansion as:

$$\frac{1}{2}mv^2 + \frac{1}{2}\pi\gamma d^2 + \frac{1}{2}V_{\text{bead}}2G_0\frac{d^2}{d_o^2} = \text{constant} \quad (4.10)$$

Here $v = \partial d/\partial t$, d is the diameter of the sheet and t is the corresponding time instant. Equation 4.10 can be rewritten as:

$$\frac{1}{2}m\dot{d}^2 + \frac{1}{2}kd^2 = \text{constant} \quad (4.11)$$

Here $k = \pi\gamma + \pi\frac{d_o}{3}G_0$ is the spring constant.

Equation 4.11 is the equation of conservation of mechanical energy of a harmonic oscillator. We can write pulsation $\omega = \sqrt{k/m}$. The maximum deformation is reached at

time $t_{\max} = T/4$, T being the period of oscillation and the origin of time is taken at the impact. Hence,

$$t_{\max} \simeq \frac{\pi}{2} \sqrt{\frac{m}{k}} \quad (4.12)$$

Putting the values of m and k in Equation 4.12, we obtain

$$t_{\max} \simeq \frac{\pi}{2\sqrt{2}} \frac{d_o}{U^*} \quad (4.13)$$

Equation 4.13 shows that t_{\max} does not depend on the impact velocity v_o . This is in good agreement with the experimental data obtained for elastic beads as well as liquid droplets as shown in Figure 4.10a. With increasing impact velocity, t_{\max} changes within 8% error. Interestingly, combining Equation 4.8 and 4.13, we expect $d_{\max}/t_{\max} \sim v_o$. We plot d_{\max}/t_{\max} as a function of v_o in Figure 4.10b, we observe that d_{\max}/t_{\max} is independent of elastic coefficients and indeed is dependent on impact velocity v_o . The solid line just shows the monotonic increase of d_{\max}/t_{\max} with v_o .

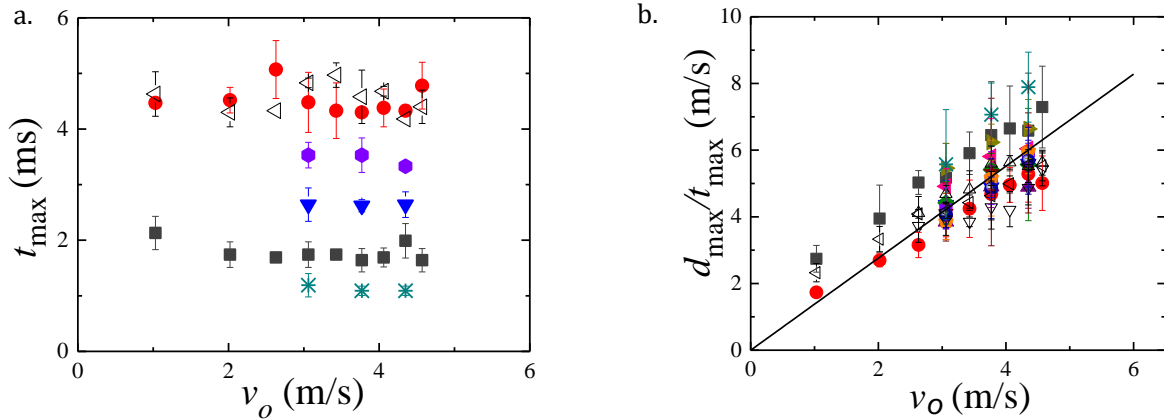


Figure 4.10: (a) t_{\max} as a function impact velocity v_o for elastic beads and liquid drops. (b) d_{\max}/t_{\max} as a function v_o . Solid line shows the linear increase of d_{\max} with v_o . Symbols are the same as in Figure 4.9.

If we rescale Equation 4.13 with the collision time $\tau_{\text{coll}} = d_o/v_o$ we obtain,

$$\frac{t_{\max}}{\tau_{\text{coll}}} \simeq \frac{\pi}{2\sqrt{2}} \frac{v_o}{U^*} \quad (4.14)$$

Equation 4.14 shows a similar dependence of $t_{\max}/\tau_{\text{coll}}$ with the reduced impact velocities v_o/U^* as Equation 4.8 for maximal spread factor. We observe that experimental data for the elastic beads and liquid drops collapse well on a single curve using Equation 4.14 as shown in Figure 4.11b unlike if we plot $t_{\max}/\tau_{\text{coll}}$ as a function of the Mach number

(Figure 4.11a) for solids only. In Figure 4.11a, we observe that the data deviates for shear modulus less than $G_0 = 43$ Pa from the solid line. The difference in the two scaling laws is the contribution of surface elasticity is considered along with bulk elasticity in Figure 4.11b. The solid line is the linear fit bx with intercept $a = 0$. The slopes are roughly similar for the two plots, 0.2 (Figure 4.11a) and 0.3 (Figure 4.11b). We note again in Figure 4.11b at higher impact velocities, the data for liquid samples are slightly lower than predicted from the scaling (Equation 4.14). This may be due also to the splashing and eventually ejection of secondary droplets from the rim.

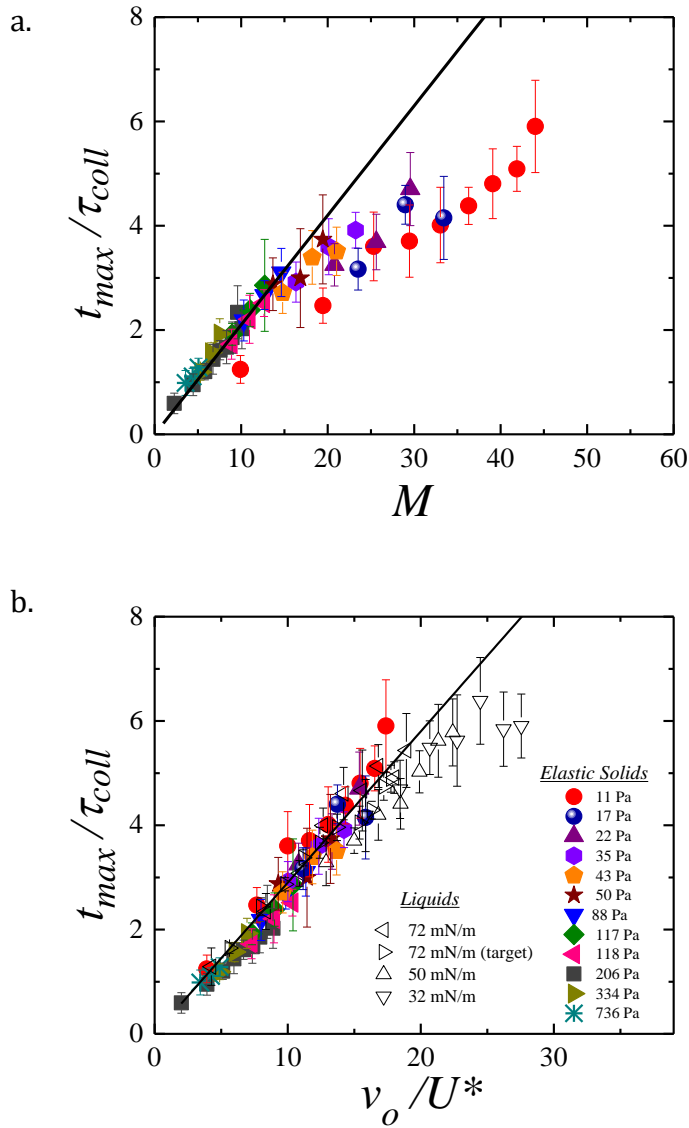


Figure 4.11: t_{max} in reduced units as a function of (a) Mach number M and (b) v_o/U^* . Solid and empty symbols corresponds to elastic beads and liquid drops respectively as indicated in the legend. Solid lines are affine fits.

We also measure the diameter of sheet d as a function of time for elastic beads and liquid drops. For the sake of clarity, we just show data at a fixed velocity $v_o = 4.35$ m/s for all the systems (Figure 4.12a) and for one elastic bead with elastic modulus $G_0 = 11$ Pa for various v_o (Figure 4.12b). All curves show similar features of expansion and retraction. We find that for a fixed impact velocity, the maximum diameter of the sheet reaches earlier in time with increasing elasticity (Figure 4.12a) and the maximum expansion d_{\max} increases with the impact velocity v_o (Figure 4.12b).

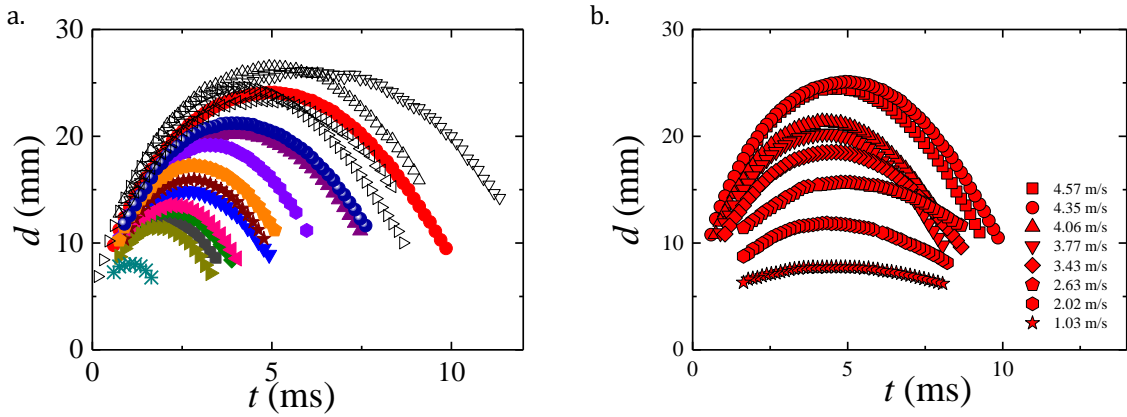


Figure 4.12: Time evolution of the diameter of the sheet d (a) for elastic beads and liquid drops impacting the solid surface with $v_o = 4.35$ m/s (symbols are same as in Figure 4.11) and (b) for an elastic bead of elastic modulus $G_0 = 11$ Pa for various impact velocities as indicated in legend.

We can write the mechanical energy of the dynamics of the sheet in adimensional units using Equation 4.10 by defining $\tilde{t} = \omega t$ and $\tilde{d} = d/d_{\max}$, hence, $\tilde{v} = v/\omega d_{\max}$. Equation 4.10 can be written as:

$$\tilde{v}^2 + \tilde{d}^2 = 1 \quad (4.15)$$

If we now rescale the experimental data $d(t)$ using the adimensional units $\tilde{d} = f(\tilde{t})$, we observe that all experimental curves for different bulk or surface elastic properties of the impacting object as well as various impact velocities collapse very well as shown in Figure 4.13. We note that the collapse of the data in the case of fixed impact velocity v_o for all the systems is quite perfect in case of both the expansion and retraction regimes by contrast in Figure 4.13b where data for one given sample at different velocities are plotted. There is a small deviation in the retraction regime. The retraction at low impact velocity is slightly slower in comparison to higher impact velocities.

Note that the shape of the curve in Figure 4.13a and b is sinusoidal at the higher deformation as shown by the green solid line in Figure 4.13a. The solid line is the sine fit for the experimental data at deformation greater than 0.6. At smaller deformation, data slightly deviates from a sinusoidal form as can be expected from a small deformation regime. Though the perfect collapse of all the data shows that there is no shear

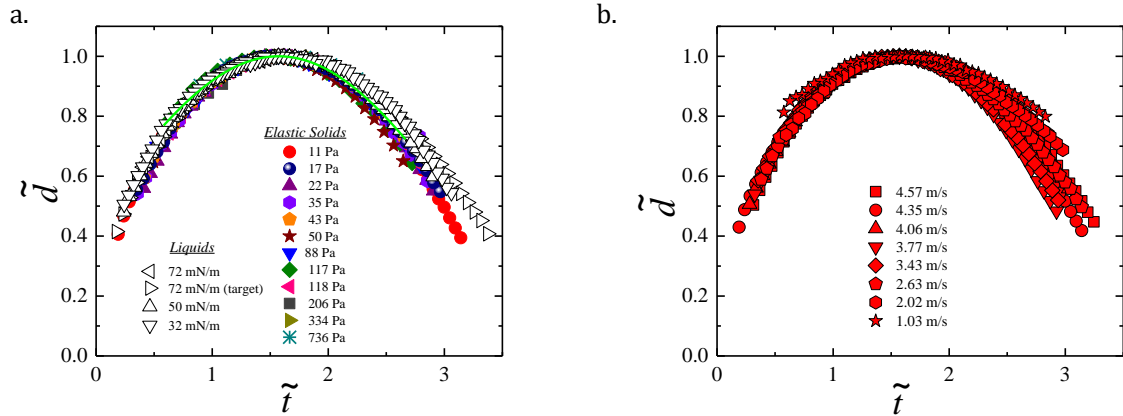


Figure 4.13: Dynamics of the sheet expansion in normalized units, d/d_{max} versus $\omega\tau$. (a) for all elastic beads and liquid drops with a fixed impact velocity $v_o = 4.35$ m/s. (b) for an elastic bead with an elastic modulus $G_0 = 11$ Pa at different impact velocities, as indicated in the legend.

viscous dissipation during expansion and retraction of the sheet, and hence validates the effectiveness of inverse Leidenfrost effect. Recently, M. Andrew *et al* [Andrew 2017] have numerically shown for an axisymmetric drop impacting on solid surfaces, that the expansion and retraction are essentially a simple harmonic motion in absence of viscous dissipation.

Note: C. Clanet *et al* have developed a model based on the pancake thickness which is governed by the capillary wave created by the impact to account for the maximal spread factor for liquids impacting on non-interacting surfaces. In Appendix C we briefly describe this model, provide an extension of this for ultrasoft elastic beads and show that the modified model does not account very well for our experimental data.

4.3 Conclusion

We have investigated freely expanding sheets produced by the impact of ultra soft elastic beads and liquid drops on a solid surface covered with a thin layer of liquid nitrogen. Upon impact, a gaseous cushion of nitrogen is formed due to the evaporation of liquid nitrogen. The cushion acts as a thermal insulator between the solid substrate and the sheet. This substantially eliminates the shear viscous dissipation due to the solid substrate. This has been claimed by T. Tran *et al* and H. Lastakowski *et al* [Tran 2012, Lastakowski 2014] where they studied the impact of liquid drops at Leidenfrost conditions. Also, another configuration was used by C. Antonini *et al* [Antonini 2013] where they studied the impact of a liquid drop on a sublimating surface (dry ice). Experimental configuration of Antonini *et al* [Antonini 2013] is similar to our experimental technique; in their case when the drop impacts on the dry ice (i.e. solid carbon dioxide), the vapor cushion forms due

to the sublimation of the solid surface unlike the case when the drop impacts the hot plate (above Leidenfrost temperature), where the vapor layer forms due the evaporation of droplet.

The impact of liquid drops on solid substrates has been studied extensively. In order to effectively minimize the effect of viscous coupling between the sheet and the substrate, D. Richard *et al* [Richard 2002] used the super-hydrophobic surfaces and A.L. bianche *et al* [Bianche 2006] studied the impact on hot plates i.e. in Leidenfrost condition. Hence as the liquid deforms the kinetic energy transforms into surface energy which then is converted back to kinetic energy, enabling the system to behave like an elastic spring. The impact of elastic beads on a solid surface is less studied. Y. Tanaka *et al* [Tanaka 2003, Tanaka 2005] studied the impact of soft gels on a solid substrate and have shown that the maximal deformation scales as the Mach number M in the case of large deformation. In their case, the elastic modulus is in the range (37 – 140 kPa) and ball diameter $d_o = 14$ mm and 31.5 mm which is much higher in comparison to our elastic system. A similar scaling law has been proposed by L.H. Luu [Luu 2009, Luu 2013] for yield-stress fluids (carbopol) with shear modulus G_0 in the range (28 – 270 Pa) and d_o varies between 7.6 – 25 mm in case of perfect slip condition. For our experiments we have $d_o = 3.7$ mm and shear modulus G_0 in the range (10 – 700 Pa). We have worked with much softer elastic solids compared to Y. Tanaka *et al* [Tanaka 2003]. We have shown that for ultra soft elastic beads in the case of large and moderate deformations, contribution of both the surface and bulk elasticity are important. We have provided a universal scaling to account for the maximal deformation in the large deformation limit by introducing the velocity of generalized elastic deformations U^* . This scaling also provides the asymptotic known behaviors of simple liquids on one side and hard solids on the other side depending on the respective values of elastocapillary length scale and the diameter of the bead or drop. The time needed to reach the maximum deformation can also be described by the same unified scaling prediction for liquids and solids as a function of reduced impact velocities. Moreover, we show that the dynamics of expansion and retraction of sheet produced by the impact of a solid bead and a liquid drop can be understood in terms of simple harmonic motion without viscous dissipation [Bianche 2006, Andrew 2017, Okumura 2003] with characteristic frequency of oscillation being U^*/d_o . Finally, we have also observed, surprisingly a universal scaling behavior that, in principle, is only valid for very large deformations, also reproduces the experimental data in the regime of moderate deformation as well.

Although elastocapillarity has not been exploited much in the case of impact dynamics, it has been taken into account in many studies focused on soft solids. For instance, S. Mora *et al* [Mora 2010b] have shown experimentally the Rayleigh-plateau instability in soft solid cylinders, T. Liu *et al* [Liu 2014] demonstrated the effect of surface tension on crack propagation in soft solids, L. Ducloué *et al* [Ducloué 2014] studied the influence of the softness of an elastic medium by the inclusion of air bubble in the matrix and A. Jagota *et al* [Jagota 2012] studied the effect of surface stresses on the deformation of soft

Chapter 4. Unified Description of the Resilient Behavior of Elastic Beads
80 and Liquid Drops on Impacting Surfaces

solids.

Impact of Viscoelastic Drops on Solid Surfaces

Contents

5.1	Experimental samples and techniques	82
5.2	Expansion of viscoelastic and Newtonian viscous sheets	82
5.2.1	Impact of viscoelastic drops using inverse Leidenfrost effect	82
5.2.2	Impact of viscoelastic drops on a small solid target	85
5.2.3	Impact of Newtonian viscous drops on a small solid target	89
5.3	Instabilities and cracks in viscoelastic sheets	91
5.4	Conclusion	97

In this chapter, we investigate the dynamics of freely expanding thin sheets. The sheets are produced by impacting a drop onto a small solid target or onto a solid surface covered with a layer of liquid nitrogen, in order to suppress any dissipation process. To disentangle the role of capillary, viscous and elastic forces in the dynamics of the sheets, different materials are used whose rheological characteristics can be tuned: viscous liquids, viscoelastic Maxwell fluids characterized by an elastic modulus, G_0 and a relaxation time, τ . From the previous chapters, we know that when τ is shorter than the typical lifetime of the sheet ($\tau_{\text{life}} \sim 10$ ms), the dynamics of viscoelastic sheets is similar to that of Newtonian viscous liquids with equal zero-shear viscosity. When τ is larger than the typical lifetime of the sheet, the behavior differs drastically. The sheet expansion is strongly enhanced as compared to that of viscous samples with comparable zero-shear viscosity η_0 . Here, we investigate bridged microemulsions which are inviscid Newtonian fluids below a percolation threshold, and viscoelastic above the threshold, with a relaxation time $\tau > \tau_{\text{life}}$. We show that the scaling law describing the maximal deformation of elastic beads and liquids drops (Chapter 4) is also valid for viscoelastic drops impacting a solid surface covered with a layer of liquid nitrogen. In addition, we show that the same scaling law also holds for viscoelastic and viscous drops impacting a small solid target, once viscous dissipation on the small target is quantitatively taken into account. Furthermore, on impacting viscoelastic drops we observe a heterogeneous expansion of the sheet with the occurrence of cracks, revealing the elastic nature of the viscoelastic fluid. This is in sharp contrast with previous observations (Chapter 4) with sheets produced with ultra-soft solids which expand but never break.

5.1 Experimental samples and techniques

We use surfactant stabilized oil droplets (microemulsions) that are suspended in water and reversibly linked by telechelic polymers with an aliphatic chain length C_{18} . For sample preparation, we fix the average number of telechelic stickers per oil droplet $r = 4$, and vary the mass fraction of oil droplets ϕ in the range (0.5% – 3.5%). The samples are similar to those used in Chapter 3.

Shear rheology is performed to investigate the sample viscoelasticity as explained in Chapter 2 (section 2.2.1). The composition of the sample is varied to tune its viscoelasticity. Above a critical ϕ , the sample behaves as a pure Maxwell fluid and is characterized by a unique shear plateau modulus G_0 and a unique characteristic relaxation time τ . These parameters are obtained by fitting the frequency dependence of the storage modulus G' and loss modulus G'' with the corresponding theoretical expressions for Maxwell fluids. We measure a percolation threshold $\phi_c = 2\%$ (Chapter 3). For $\phi > \phi_c$, the shear plateau modulus G_0 is in the range (2 Pa - 34 Pa) and the characteristic time τ ranges between 100 ms and 425 ms. Note that the relaxation time for all viscoelastic systems is much higher than the total duration of the experiment ($\tau_{\text{life}} \sim 10$ ms). We define Deborah number $De = \tau/\tau_{\text{life}}$ and in our experiments it lies in the range (10 - 42).

The surface tension γ is measured with a pendant drop tensiometer (SINTERFACE PAT-1M) for dilute bridged microemulsions below percolation ($\phi = 0.5\%$). We find $\gamma = 28$ mN/m. We assume that this value is valid for all bridged microemulsions even above percolation.

Here we use two techniques, (i) drop impact on a solid surface covered with a layer of liquid nitrogen (as in Chapter 4) and (ii) impact on a small solid target (as in Chapter 3). We vary the impact velocity v_o between 1.7 m/s and 4.0 m/s. We use data presented in Chapter 3 for bridged microemulsions and viscous samples and perform some additional drop impact experiments on a solid target by varying the impact velocity v_o between 1.3 m/s and 4.3 m/s for a viscoelastic sample with an elastic modulus $G_0 = 19$ Pa. Time series of images of the sheets are recorded using a fast camera as detailed in Chapter 2 (section 2.3.1 and 2.3.2). The images are analyzed as explained in Chapter 2 (section 2.4).

5.2 Expansion of viscoelastic and Newtonian viscous sheets

5.2.1 Impact of viscoelastic drops using inverse Leidenfrost effect

We perform similar experiments with viscoelastic samples as the ones described in Chapter 4 for elastic solids and inviscid Newtonian liquids. In brief, a viscoelastic drop

impacts a solid surface covered with a thin layer of liquid nitrogen. On impacting the solid surface, a vapor cushion forms that thermally insulates the radially expanding drop. The main objective of this part is to experimentally investigate whether the scaling law for the maximal deformation of elastic beads and liquid drops is also valid in the case of viscoelastic drops for which we expect elasticity, surface tension, and viscosity to play a role. Figure 5.1 shows snapshots of a sheet at its maximum expansion produced with drops of microemulsion with different shear moduli G_0 (b,c) and of a microemulsion below percolation $G_0 = 0$ (a) but at a fixed impact velocity $v_o = 3.8$ m/s. We observe a slight decrease in the maximum expansion with the increase of G_0 . Also, the maximum deformation of the drop decreases with decreasing impact velocity v_o .

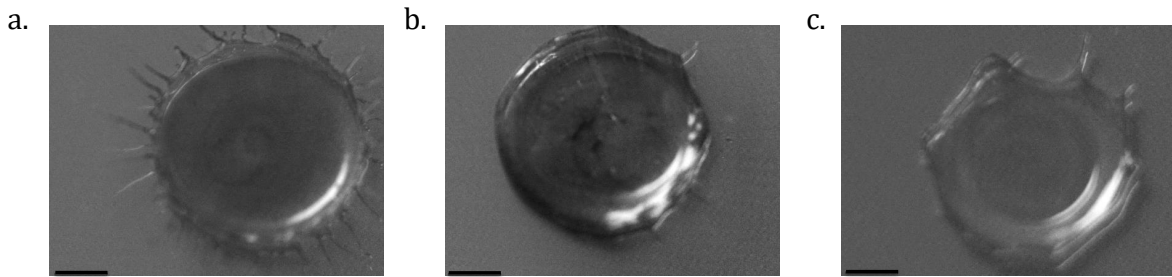


Figure 5.1: Images of the sheets at the maximum expansion for microemulsions produced by impacting drops at a fixed impact velocity $v_o = 3.8$ m/s for (a) below percolation ($G_0 = 0$) (b) and (c) above percolation ($G_0 = 10$ Pa) and ($G_0 = 21$ Pa). The scale bars are 6 mm.

Experimentally we measure the maximum diameter reached by the sheet, d_{\max} and define the maximal spread factor $\lambda = d_{\max}/d_o$, where d_o is the initial diameter of the drop. In our experiments, the relaxation time of the viscoelastic samples is always higher than the time scale of the experiment i.e. $De \gg 1$. Hence, we expect the elastic nature of the sample to largely dominate their behavior. The elasticity of a viscoelastic sample is characterized by the shear plateau modulus G_0 . In the literature, the maximal spread factor for yield stress fluids has been shown to be proportional to the elastic Mach number $M = v_o/U_S$ [Luu 2009, Luu 2013] in the case of perfect slip. $U_S = \sqrt{\frac{G_0}{\rho}}$ is the velocity of transverse sound waves in an elastic medium [Kolsky 1963] with ρ the sample density. In Figure 5.2a we plot the maximal spread factor λ as a function of the Mach number M for all viscoelastic drops. In our experiments M varies between 10 and 90 and λ between 3.5 and 7.5. For all samples, we find that λ increases monotonically with M . However one does not measure a linear evolution of λ with M . Furthermore, one finds that data with different elastic moduli do not collapse.

For pure elastic beads (Chapter 4), we have explained the deviation of the experimental data from the simple theoretical expectation, $\lambda \sim M$, by taking into account the surface tension of the beads. λ is calculated by balancing the initial kinetic energy with

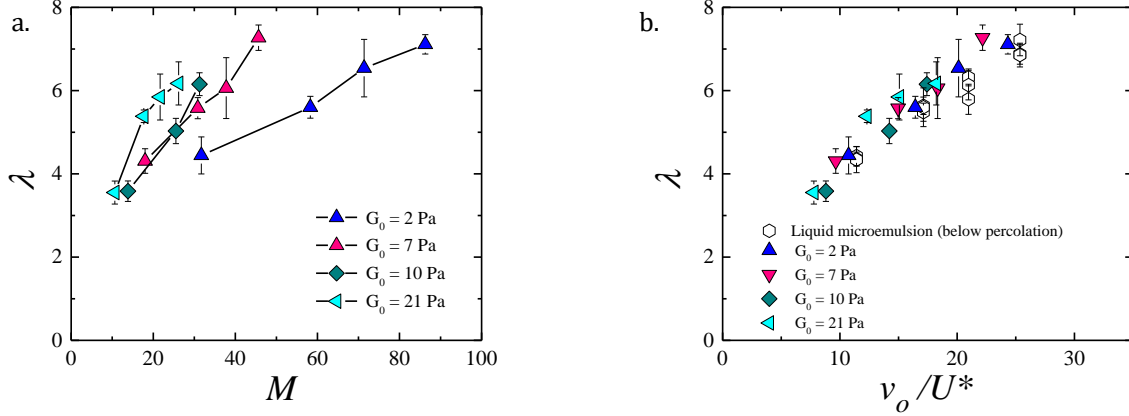


Figure 5.2: (a) Maximal spread factor λ as a function of Mach number M . (b) λ as a function of v_o/U^* where v_o is the impact velocity and U^* is the characteristic velocity for generalized elastic deformations. The filled symbols are the experimental data points for viscoelastic samples with different shear plateau modulus G_0 as indicated in the legend. The solid lines are guides to the eye. The open symbols correspond to liquid microemulsion samples (below percolation).

the surface energy and bulk elastic energy at maximum expansion, under the assumption of zero dissipation one obtains:

$$\lambda \approx \frac{1}{\sqrt{2}} \frac{v_o}{\sqrt{U_L^2 + U_S^2}} \approx \frac{1}{\sqrt{2}} \frac{v_o}{U^*} \quad (5.1)$$

Here, $U_S = \sqrt{\frac{G_0}{\rho}}$ is the velocity of transverse sound waves in an elastic medium and $U_L = \sqrt{\frac{3\gamma}{\rho d_o}}$ is the typical velocity of the free oscillations of a drop called Rayleigh velocity [Rayleigh 1879] with γ the surface tension and $U^* = \sqrt{U_L^2 + U_S^2}$ is the velocity of generalized elastic deformations. We plot the maximal spread factor λ as a function of v_o/U^* for the viscoelastic bridged microemulsions ($\phi > 2\%$) and also for liquid samples (bridged microemulsion below percolation threshold). We find that all data collapse on a same unique curve.

We next compare the experimental data obtained by the impact of drops of bridged microemulsion with those obtained with elastic beads and liquid drops. The elastic modulus of the elastic beads varies between 10 and 700 Pa (Chapter 4). Several Newtonian liquids are considered (Chapter 4) in addition to microemulsion below the percolation threshold yielding four liquids with surface tension ($\gamma = 72, 50, 32, 28$ mN/m). We plot λ as a function of v_o/U^* in Figure 5.3 for elastic beads, viscoelastic drops and liquid drops together. For simplicity we use a unique symbol for each class of sample. We observe that all data collapse on one single curve. Furthermore, for $\lambda \lesssim 7$ and $v_o/U^* \lesssim 20$, we find a linear variation of λ with v_o/U^* as theoretically expected from Equation 5.1. The

best fit yields $a = 0.6$ and a slope $b = 0.35$ which is twice smaller than the theoretical expectation (Equation 5.1).

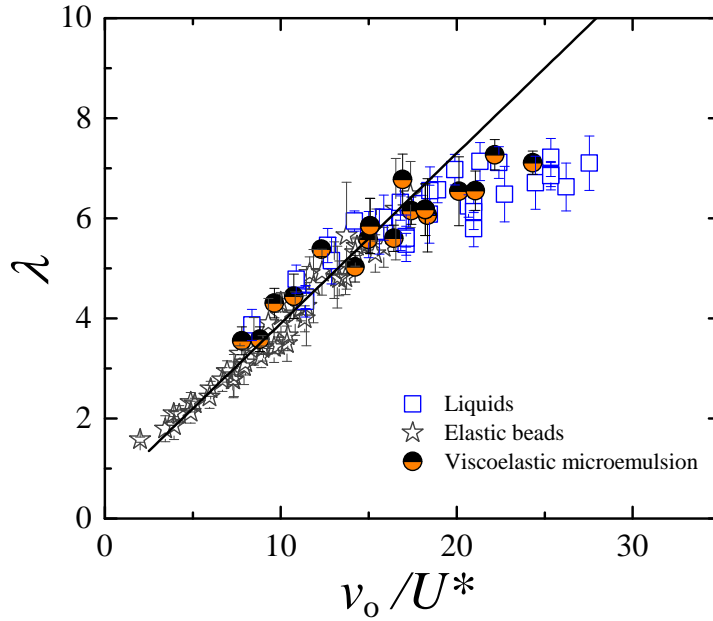


Figure 5.3: Maximal spread factor λ as a function of v_o/U^* where v_o is the impact velocity and U^* is the velocity of generalized elastic deformations. The symbols are experimental points for viscoelastic drops, elastic beads and liquid drops.

For simple liquids and viscoelastic fluids there is some deviation at higher velocities, the maximum spread factor being smaller than the theoretically expected value. This can be attributed to splashing [Mundo 1995, Rioboo 2001] and the formation of small ligaments in the case of viscoelastic samples with very low elastic modulus ($G_0 \approx 2$ Pa) that are not accounted in the measurement of the sheet area leading to an underestimation of the diameter of the sheet.

Our experiments demonstrate that Maxwell fluid drops with a characteristic relaxation time higher than experimental time obey the same scaling law for maximal deformation as elastic solids and simple liquids.

5.2.2 Impact of viscoelastic drops on a small solid target

We use the experimental data for the maximal spread factor of bridged microemulsions as in Chapter 3 (liquid microemulsions (below percolation, $\gamma = 28$ mN/m and $\eta_0 = 1.2 - 120$ mPa.s) and viscoelastic microemulsions (above percolation, $\gamma = 28$ mN/m, $G_0 = 2 - 34$ Pa and $\tau = 100 - 425$ ms). We also perform some additional experiments at

different impact velocities in the range (1.3 m/s - 4.3 m/s) for water ($\gamma = 72$ mN/m, and $\eta_0 = 1$ mPa.s) and a viscoelastic microemulsion ($\gamma = 28$ mN/m, $G_0 = 19$ Pa, and $\tau = 270$ ms). Figure 5.4 shows the images at the maximum expansion for microemulsion drops with different shear modulus G_0 and relaxation time τ but at a fixed impact velocity $v_o = 4$ m/s. We observe that the maximum diameter of the sheet slightly decreases with increasing G_0 . We also note that the ejection of secondary droplets and the formation of ligaments are almost suppressed for viscoelastic samples as compared to liquid ones.

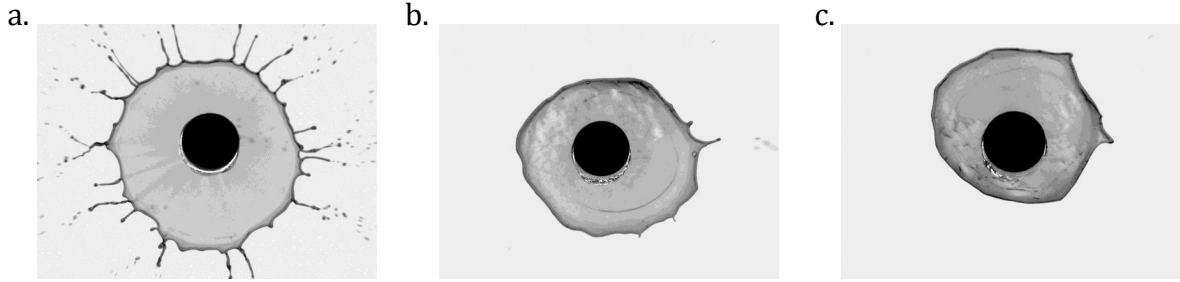


Figure 5.4: Images of the sheet at maximum expansion produced by impacting drops of microemulsion at a fixed impact velocity $v_o = 4$ m/s onto a small solid target. In (a) sample (below percolation) is liquid ($\eta_0 = 4$ mPa.s), (b) and (c) samples (above percolation) are viscoelastic with $G_0 = 7$ Pa and $\tau = 190$ ms (b) and $G_0 = 32$ Pa and $\tau = 333$ ms (c). The scale bar is set by the solid black disc of diameter 6 mm.

Figure 5.5 shows snapshots of images at the maximal expansion of the sheet for bridged microemulsion ($G_0 = 19$ Pa, $\tau = 270$ ms) and for water at different impact velocities. We observe that the ejection of secondary droplets is suppressed in the case of viscoelastic microemulsions compared to water. Also, at a fixed velocity the maximum expansion of water drops is larger than for viscoelastic microemulsions. For both samples, we also measure that the maximum expansion increases with the impact velocity.

To quantify the maximum deformation produced by the impact of bridged microemulsion drops on a small solid target, we first attempt to use the same scaling law for λ as in the case of impact on the solid surface covered with liquid nitrogen layer. We, therefore, plot the experimental data obtained from pure water and microemulsion drops on impacting the solid target in Figure 5.6 along with the data for the samples impacting the surface covered with liquid nitrogen as shown previously in (Figure 5.3).

We observe that the data for pure water drops, collapse with previous experimental data obtained from inverse Leidenfrost experiments. By contrast, there is a significant deviation in the case of liquid microemulsions (below percolation) and an even more apparent deviation for data above percolation. The maximal spread factor is systematically smaller for the impact on solid target than for the impact on the surface covered with liquid nitrogen. This deviation may be attributed to shear viscous dissipation that occurs due to the interaction between the microemulsion drop and the solid surface of the target.

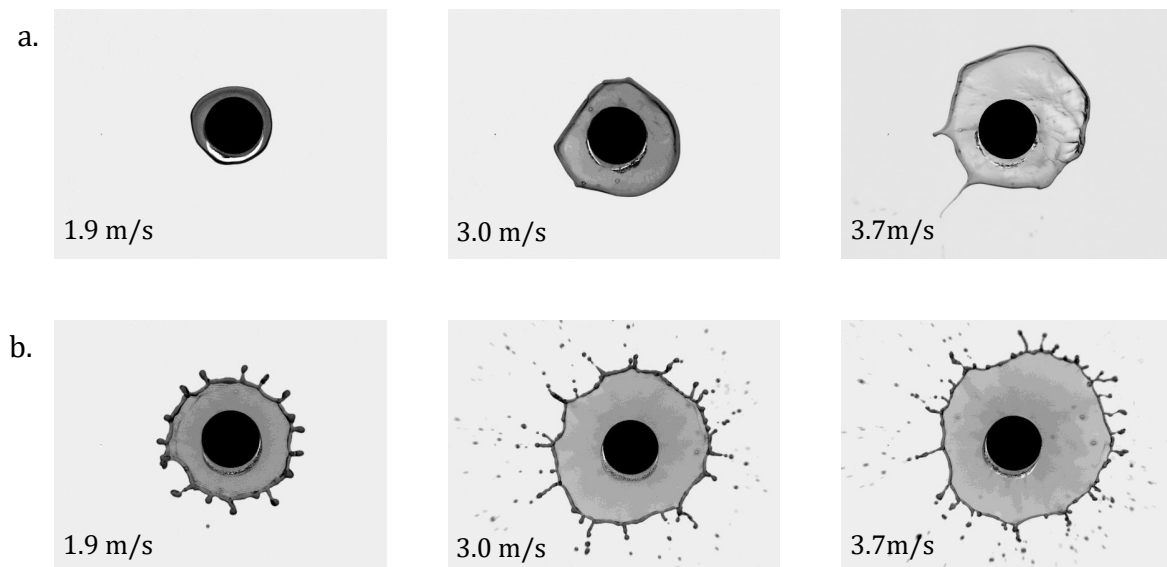


Figure 5.5: Snapshots of images at maximum expansion for (a) viscoelastic microemulsion ($G_0 = 19$ Pa $\tau = 270$ ms) and (b) water, at different impact velocities as indicated on the images. The scale bar is set by the black solid disc of diameter 6 mm.

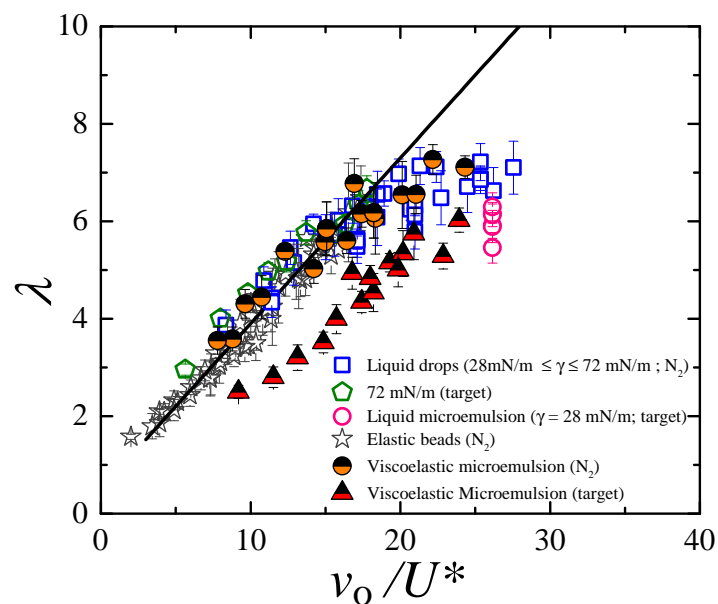


Figure 5.6: Maximal spread factor λ as a function of v_o/U^* where v_o is the impact velocity and U^* is the velocity of generalized elastic deformations. The symbols are experimental data points for elastic beads, liquid drops and viscoelastic drops for experiments performed using inverse Leidenfrost set-up referred to as " N_2 " and on a small solid target referred to as "target" as indicated.

Indeed Equation 5.1 holds only in the case of a complete absence of shear dissipation. Zero shear viscous dissipation conditions have been achieved in the experiments done with help of inverse Leidenfrost effect. On the other hand, in Chapter 3 we have shown that viscous dissipation occurs in the boundary layer at the interface between the surface of the target and the liquid. To quantitatively account for this viscous dissipation at the maximum expansion we have introduced an effective impact velocity v_{eff} which is reduced compared to the real one. The effective velocity is defined as the velocity of the sheet as it expands out of the target. We measure v_{eff} by taking the time derivative of the diameter of the sheet d at short time, i.e. when the size of the sheet becomes larger than the size of the target: $v_{\text{eff}} = \frac{1}{2} \frac{\partial d}{\partial t} \Big|_{t \rightarrow 0}$.

To show the effect of viscous dissipation on the solid target we plot in Figure 5.7 v_{eff} as a function of v_o for pure water and bridged microemulsions (varying ϕ at fixed impact velocity $v_o = 4$ m/s and varying v_o for a given sample with $G_0 = 19$ Pa and $\tau = 270$ ms). We find that for water, $v_{\text{eff}} = v_o$, over the whole range of impact velocity explored. By contrast, for microemulsions v_{eff} is systematically smaller than v_o . Interestingly, we note that even for microemulsions below percolation ($\eta_0 = 1.2 - 120$ mPa.s) viscous dissipation is present as v_{eff} is smaller than v_o and lies below the data of water drops.

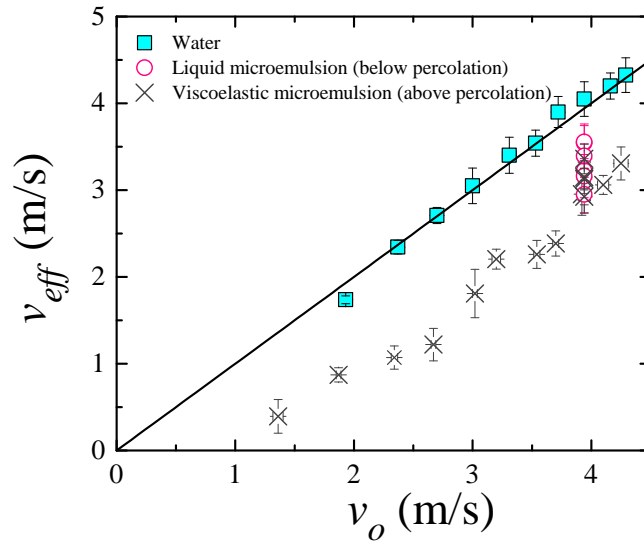


Figure 5.7: Effective velocity v_{eff} of the sheet measured at short time as a function of impact velocity v_o . The solid line corresponds to $v_{\text{eff}} = v_o$.

Interestingly, we find that replacing the impact velocity v_o by the effective velocity v_{eff} which corresponds to the effective viscosity of a drop when dissipation can be neglected, all experimental data points collapse on a single curve as shown in Figure 5.8. The data acquired in the experiments using inverse Leidenfrost effect are also shown for which one expects $v_{\text{eff}} = v_o$. The solid line is a linear fit as in Figure 5.3.

Hence, we demonstrate that the scaling law derived for samples impacting a solid surface without interaction is also valid for the impact on a small solid target once viscous dissipation is accounted.

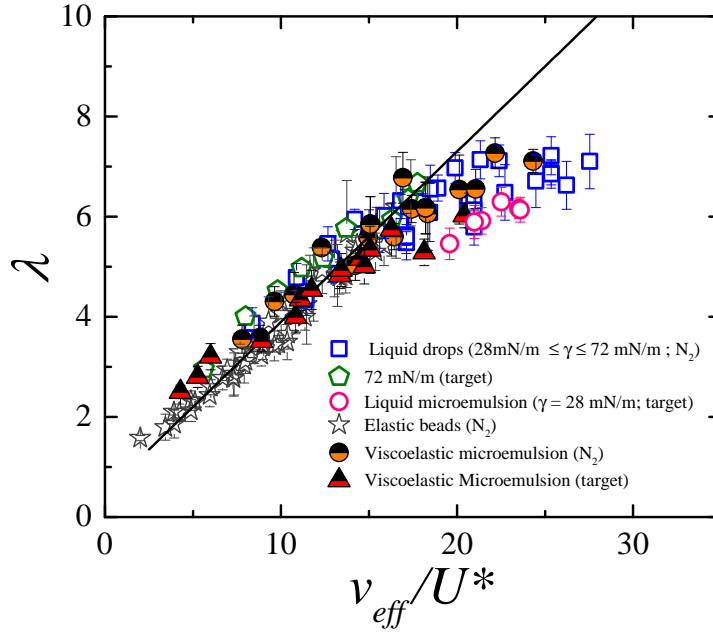


Figure 5.8: Maximal spread factor λ as a function of v_{eff}/U^* where v_{eff} is the effective velocity measured for the experiments on a small target (for inverse Leidenfrost experiments $v_{\text{eff}} = v_o$) and U^* is the velocity of generalized elastic deformations. The symbols are experimental data points for elastic beads, liquid drops and viscoelastic drops for experiments performed using inverse Leidenfrost set-up referred to as " N_2 " and on a small solid target referred to as "target" as indicated.

5.2.3 Impact of Newtonian viscous drops on a small solid target

To further check the above scaling law, we investigate drops of Newtonian liquids impacting on a small solid target. We use here glycerol/water mixtures (these samples have been already studied in detail in Chapter 3). Their surface tension is $\gamma = (66.9 \pm 3.4)$ mN/m but the viscosity varies over a broad range (1.8 mPa.s - 700 mPa).

We plot in Figure 5.9 the experimental data for glycerol/water mixtures together with all the data of previous samples and experimental conditions (Figure 5.8). Figure 5.9a shows the variation of λ with v_o/U^* : we observe that the scaling is totally ineffective in interpreting the behavior of λ for viscous samples on a small solid target. Since, for a given impact velocity, and for a given surface tension, the model predicts a given maximal spread factor, whereas one measures that λ strongly depends on the sample

viscosity. However, if we use v_{eff} which accounts for the viscous effects, we observe the collapse of experimental data on the previously obtained curve Figure 5.8. Hence, all viscous dissipation effects can be incorporated by replacing the impact velocity of the drop by the velocity of the simple or viscoelastic liquid at the edge of the target. So, in this case the maximum expansion of the sheet results from a balance between the kinetic energy of the sheet at the edge of the target and the surface elastic energy of the sheet at maximal expansion.

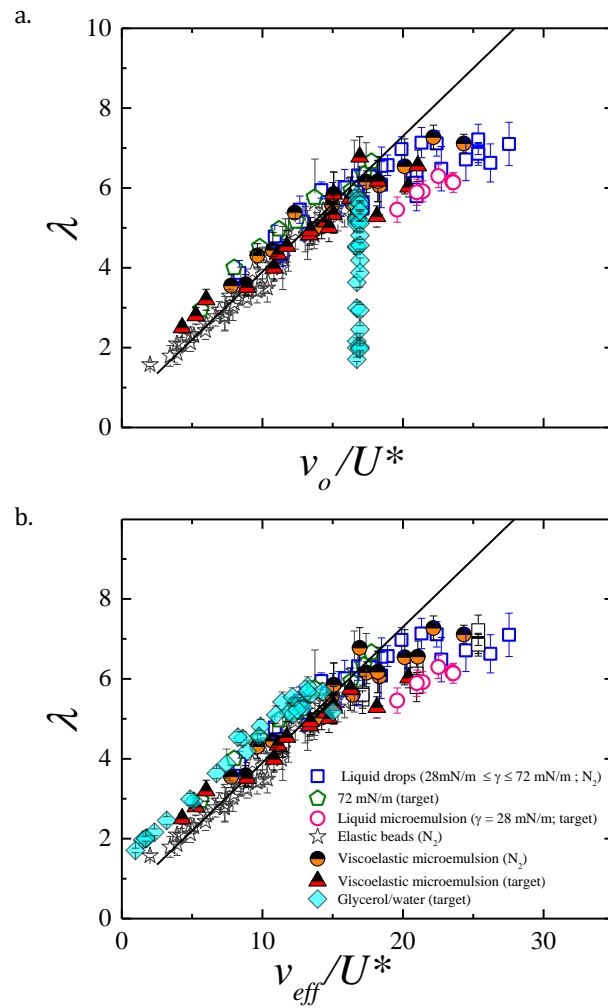


Figure 5.9: Maximal spread factor λ as a function of (a) v_o/U^* (b) v_{eff}/U^* where v_o is the impact velocity, v_{eff} is the effective velocity and U^* is the velocity of generalized elastic deformations. The symbols are experimental data points for elastic beads, liquid drops, Newtonian viscous drops, and viscoelastic drops for experiments performed using inverse Leidenfrost set-up referred to as " N_2 " ($v_{\text{eff}} = v_o$) and on a small solid target referred to as "target" as indicated ($v_{\text{eff}} \leq v_o$).

5.3 Instabilities and cracks in viscoelastic sheets

When a liquid drop impacts on a solid surface covered with liquid nitrogen or on a small solid target, a uniform sheet forms, which exhibits a smoothly varying thickness. Similarly, upon impact, an elastic bead expands smoothly. By contrast upon impact, a viscoelastic drop produces a radially expanding sheet that may exhibit instabilities. These instabilities are visible for viscoelastic samples for which the intrinsic relaxation time is much higher than the lifetime of the sheet ($De \gg 1$). We suspect these instabilities to arise from fluctuations in the thickness of the sheet. To check this hypothesis, we have dissolved a dye (eriolglaucine salt (2.5 g/L)) in bridged microemulsions to have a better contrast in the sheet. Previous experiments [Vernay 2015c] have shown that the grey scale of the image of the sheet is quantitatively correlated with the thickness of the sheet. A thicker sheet appears darker as compared to thinner sheets. For illustration Figure 5.10 displays the expansion of a viscoelastic sheet produced by (a) a sample with shear modulus $G_0 = 7$ Pa and relaxation time $\tau = 200$ ms impacting on a small solid target, and (b) a sample with $G_0 = 10$ Pa and $\tau = 400$ ms impacting on a solid surface covered with a thin layer of liquid nitrogen. In both cases, we observe that, as the sheet expands radially, some internal ruptures occur within the sheet that grows with time while a thick rim sustains the overall integrity of the sheet.

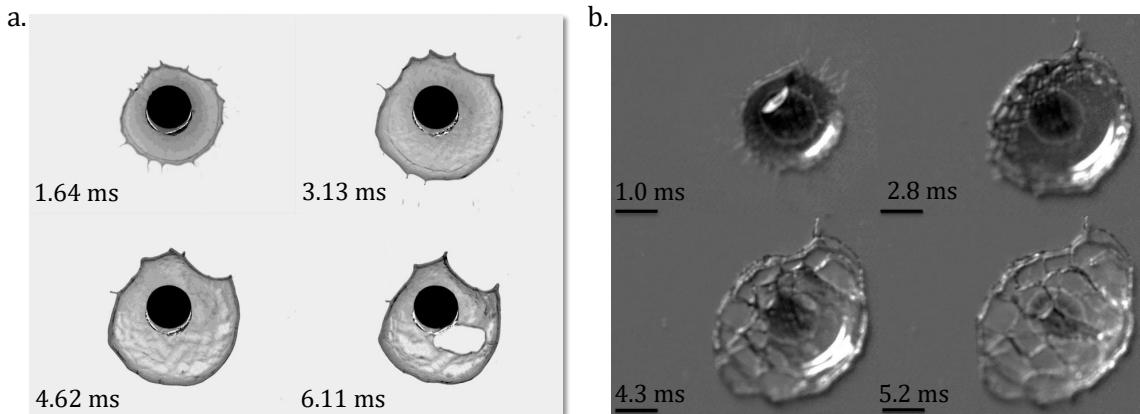


Figure 5.10: Images of the sheet at different times and at a fixed impact velocity $v_o = 3.9$ m/s for a viscoelastic drop (a) with an elastic modulus $G_0 = 7$ Pa impacting on a small solid target. The scale bar is set by the black solid disc of diameter 6 mm and (b) with $G_0 = 10$ Pa impacting on a solid surface covered with liquid nitrogen. The scale bars are 6 mm.

These irregularly shaped instabilities can occur at any point of time during the lifetime of the sheet, i.e. before or after the maximum expansion of the sheet, and thus seems stochastic in nature. This is shown in Figure 5.11 where we plot the time of occurrence of first rupture events within the sheet as a function of the shear plateau modulus G_0 of the viscoelastic samples. The star-shaped symbols show the time corresponding to the

maximum expansion and the square mark the time when the first rupture event occurs within the sheet. The time for the rupture is evaluated by the defined intensity cut-off value. Time $t = 0$ is the time when the drop hits the solid target.

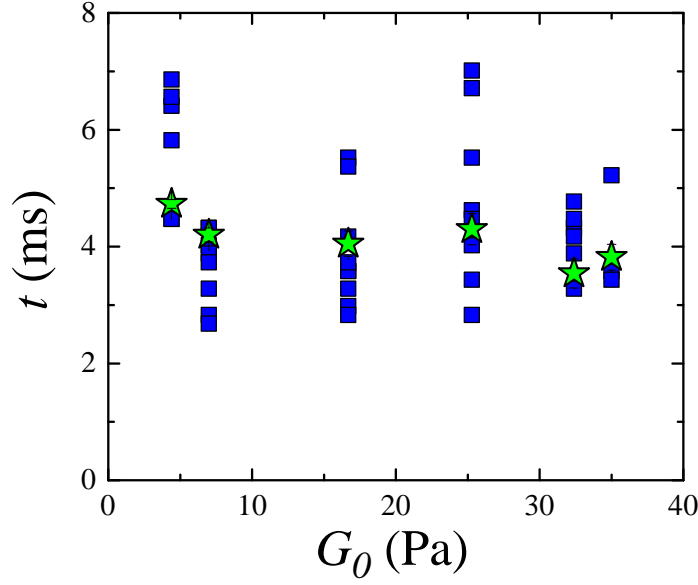


Figure 5.11: Time of occurrence of the first rupture event (square symbols) plotted against the elastic modulus for the microemulsion drop impacting a small solid target. Stars indicate the time at the maximum expansion of the sheet with error bars smaller than the symbol size.

Figure 5.12 shows snapshots taken at the maximal expansion for viscoelastic samples with an elastic modulus $G_0 \simeq 20$ Pa, for two kinds of experiment (impact on a small solid target and impact on a solid surface covered with liquid nitrogen) for impact velocities v_o in the range (1.7 m/s - 3.9 m/s). At high velocity, the sheet expands much more than at small velocity owing to the higher initial kinetic energy. With the decrease in the impact velocity rupturing of the sheet does not occur. Nevertheless, the sheet thickness is not homogeneous during the expansion or retraction at lower impact velocities. Notably, the images obtained from experiments using a small solid target have a much better contrast in comparison to experiments performed using inverse Leidenfrost effect due to the expansion in air.

To quantitatively investigate the homogeneity of the sheet in the case of experiments performed on a small solid target, we measure the mean intensity I and the standard deviation ΔI in time as explained in detail in Chapter 2 (section 2.4). In brief, four regions of interest (ROIs), each corresponding to an area 5mm^2 are selected close to the target, as shown by the black lines on the images of the sheets (Figure 5.13). We use ImageJ to independently measure I and ΔI for the four ROIs. The coefficient of

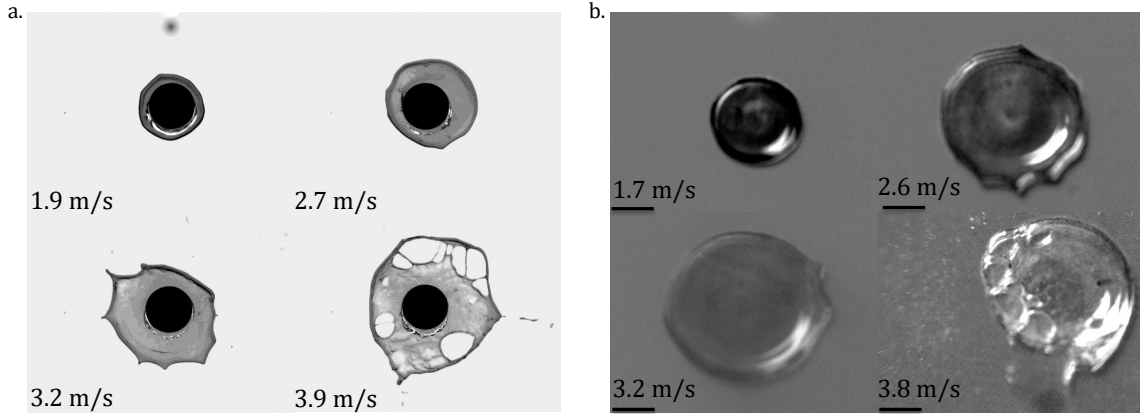


Figure 5.12: Snapshot at maximum expansion for sheets produced with viscoelastic samples at different impact velocities as indicated, impacting (a) on a small solid target for a sample with $G_0 = 19$ Pa (the scale bar is set by the black solid disc of diameter 6 mm) and (b) on a solid surface covered with liquid nitrogen for a sample with $G_0 = 21$ Pa. (The scale bars are 6 mm).

variation $\Delta I/I$ is calculated for the four ROIs and finally average over four ROIs. For clarity we show in Figure 5.13 the time evolution of $\Delta I/I$ for one measurement, in case of a viscoelastic sample ($G_0 = 19$ Pa and $\tau = 270$ ms) in the main plot, and for liquid samples (water and bridged microemulsion below percolation) in the inset. The shaded area shown is the error bar resulting from the average over the four ROIs and the symbols are the mean values.

For liquid samples, we measure that $\Delta I/I$ stays roughly constant in time, i.e. whole thickness of the sheet during expansion and retraction is homogeneous. Images taken at the maximum expansion are shown in Figure 5.13. We measure $\Delta I/I = 0.030 \pm 0.004$ for water and $\Delta I/I = 0.025 \pm 0.004$ for bridged microemulsion below percolation as averaged over the lifetime of the sheet. Our observation can be generalized for experiments performed with liquid samples at different impact velocities. Data are acquired for water samples with various impact velocities v_o and for several bridged microemulsion below percolation (several ϕ). We find that $\Delta I/I$ does not depend on v_o and ϕ . An average over different experimental conditions yield $\Delta I/I = 0.040 \pm 0.007$ as averaged over v_o for water and $\Delta I/I = 0.030 \pm 0.005$ as averaged over ϕ for bridged microemulsion (below percolation).

In the case of a viscoelastic sample, we measure that, at shorter times, i.e. before the occurrence of rupture events, $\Delta I/I$ is comparable although slightly larger than liquid samples ($\Delta I/I = 0.06 \pm 0.003$). However, as the sheet ruptures (within one of the ROI) there is a sharp increase by a five fold in $\Delta I/I$ is recorded. Images are shown with the guided arrows for the corresponding time.

Previous analysis suffers from the fact that the result might depend on the choice of

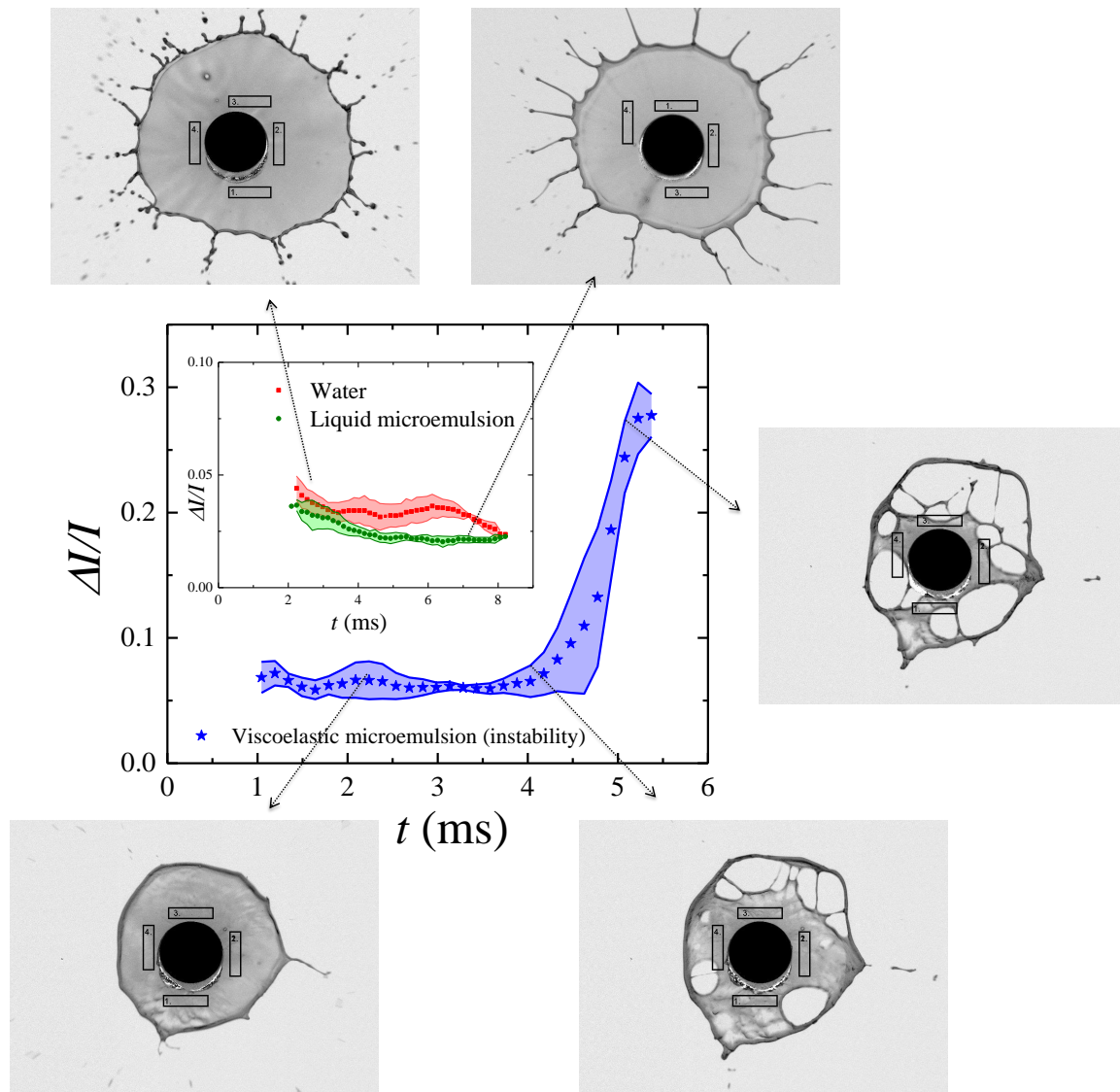


Figure 5.13: $\Delta I/I$ as a function of time for a viscoelastic sample with $G_0 = 19$ Pa (main plot). The inset shows the same for pure water and bridged microemulsion below percolation. The shaded area shows the error bars and symbols are the mean values. The sheets are produced for a fixed impact velocity $v_o = 4$ m/s. Images are shown at the corresponding time and samples.

ROIs. To overcome this limitation, we perform complimentary analysis for which the intensity fluctuations are measured over the whole area of the sheet. However, because this has to be done manually, we restrict our analysis to the maximal expansion of the sheet. Figure 5.14a shows $\Delta I/I$ as a function of ε for bridged microemulsions. As explained in Chapter 3, we define ε as the normalized distance from the percolation threshold $\varepsilon = \frac{\phi - \phi_c}{\phi_c}$, ϕ is the mass fraction of oil droplets and $\phi_c = 2\%$ is the critical mass fraction of droplets above which the system behaves as viscoelastic. The error bar on each symbol is the result of averaging over three experiments done for the same sample under the same experimental conditions. We observe that, below percolation ($\varepsilon < 0$), $\Delta I/I$ stays constant. On averaging over different liquid samples we measure $\Delta I/I = 0.05 \pm 0.005$, hence numerically comparable to the values measured for liquids previously with the analysis in time over different ROIs (shown by the highlighted band in Figure 5.14).

Interestingly, we find that $\Delta I/I$ continuously increases above percolation, i.e. for viscoelastic samples up to $\varepsilon_c = 0.35$ ($\Delta I/I = 0.17 \pm 0.023$) and then slightly decreases but is always much larger than below percolation ($\Delta I/I \cong 0.11 \pm 0.011$). Similarly, we also plot $\Delta I/I$ as a function of the impact velocity v_o in Figure 5.14b for water and for the bridged microemulsion with $G_0 = 19$ Pa which exhibits the highest heterogeneities as measured in Figure 5.14a. We find that $\Delta I/I$ does not depend on the impact velocity: $\Delta I/I = 0.050 \pm 0.005$ for water and $\Delta I/I = 0.13 \pm 0.04$ for bridged microemulsion (as averaged over all investigated velocities). Hence, the results of Figure 5.14 strongly suggest that heterogeneity in the sheet are governed by the sample elasticity and independent of impact velocity studied here.

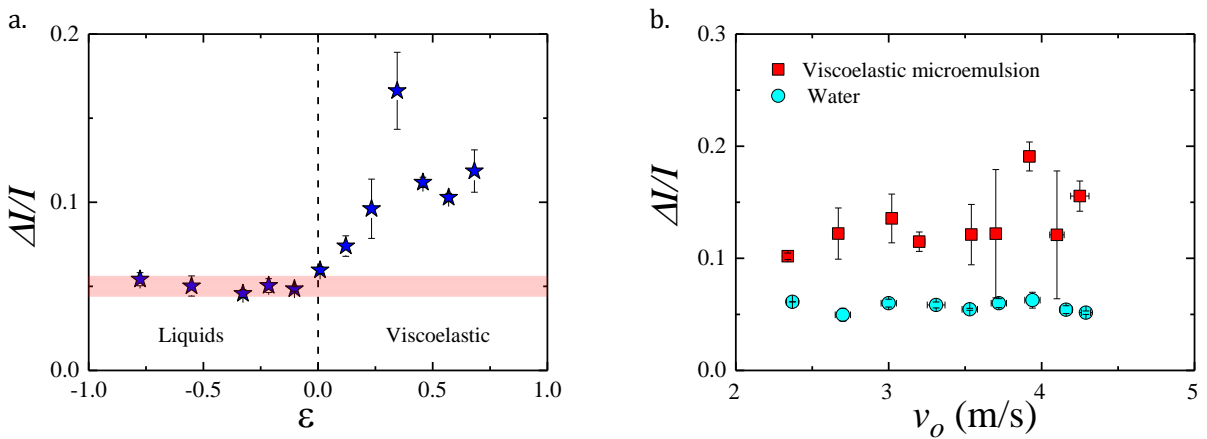


Figure 5.14: (a) $\Delta I/I$ averaged over the whole area of the sheet at maximum expansion is plotted as (a) a function of ε (normalized distance from the percolation threshold) for bridged microemulsion below ($\varepsilon < 0$) and above percolation ($\varepsilon > 0$) for an impact velocity $v_o = 4$ m/s. (b) $\Delta I/I$ as a function of impact velocity for water and bridged microemulsion above percolation ($\varepsilon = 0.35$). Symbols are the mean value of $\Delta I/I$.

Further, a calibration curve has been previously derived by correlating the grey level of each pixel I of the image of a dyed liquid sheet to the local thickness h of the sheet: $h = L \exp(-BI)$ with $L = 2207 \mu\text{m}$ and $B = 6.187$ [Vernay 2015c]. Note that h is not constant over the whole surface of the sheet, but decays from the center to the edge of the sheet [Vernay 2015c]. Here, we measure an average value of h .

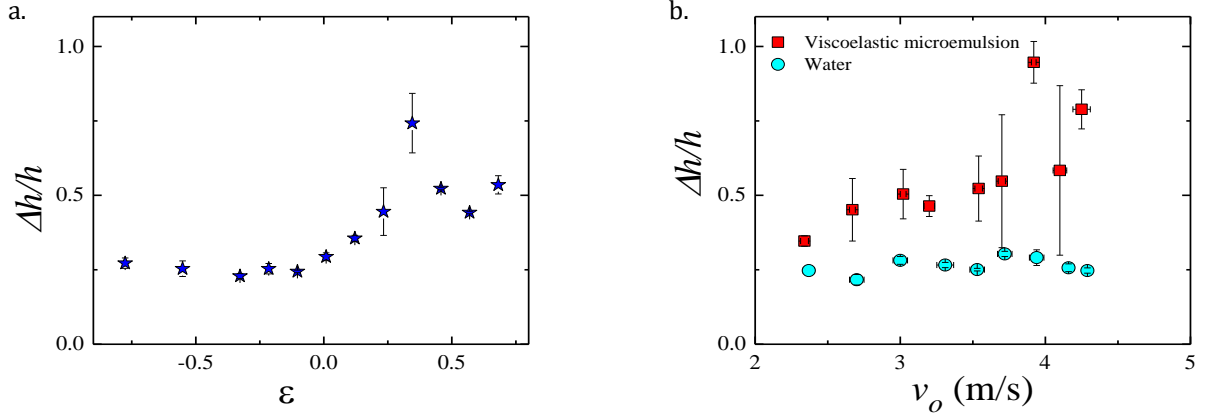


Figure 5.15: (a) $\Delta h/h$ is plotted as (a) a function ε (normalized distance from the percolation threshold) for the impact velocity $v_o = 4$ m/s. (b) $\Delta h/h$ as a function of the impact velocity for water and bridged microemulsion ($\varepsilon = 0.35$). Symbols are the mean value of $\Delta h/h$. The data are same as in Figure 5.14.

We used the above relation between the thickness and intensity and plot the data of Figure 5.14 in terms of the relative fluctuations of $\Delta h/h = B\Delta I$ (Figure 5.15). We observe that for viscoelastic samples the relative fluctuations of the thickness increases with increasing elasticity and marginally increases with increasing impact velocity. For water, $\Delta h/h$ stays constant with increasing impact velocity. Thus the occurrence of cracks is essentially intrinsic to elasticity rather than impact velocity.

Figure 5.16a shows an example of the spatial fluctuation (guided by an arrow) in the sheet produced by impacting viscoelastic microemulsion drop on a small solid target followed by the emergence of the crack. In comparison, we can see that in the case of a sheet produced by the impact of water drop, the sheet is homogeneous during the expansion. At present, it is not clear how to analyze and rationalize those spatial fluctuations.

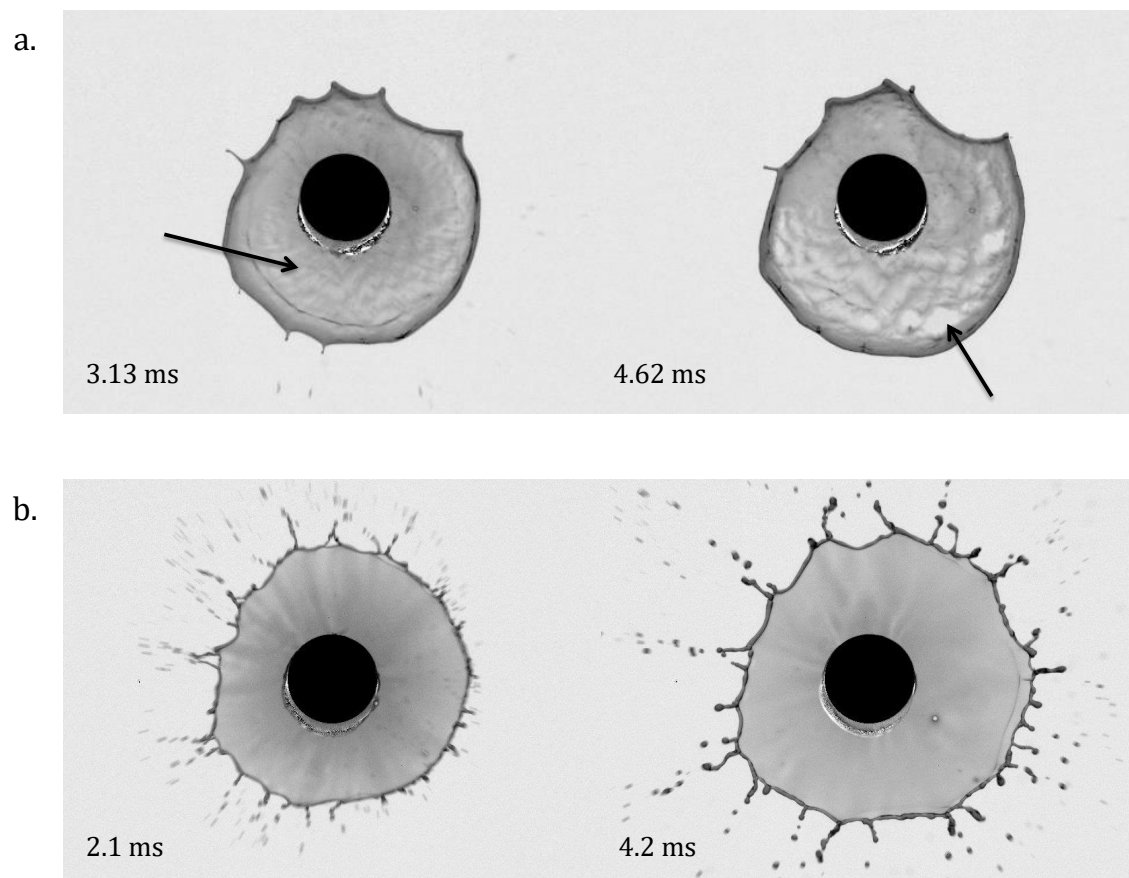


Figure 5.16: Images of the sheet at different times at fixed impact velocity $v_o = 4$ m/s for (a) viscoelastic bridged microemulsion $G = 19$ Pa (b) water. The scale bar is set by black solid disc of diameter 6 mm.

5.4 Conclusion

We have investigated freely expanding sheets produced by the impact of viscoelastic drops on a solid surface using inverse Leidenfrost effect and on a small solid target. There are few studies available in the literature regarding the impact of viscoelastic drops compared to studies dealing with Newtonian systems. There have been experiments performed to investigate the effect of polymer on the dynamics of thin sheets. The main focus of these studies was to investigate the suppression of the drop rebound. Many hypotheses have been proposed: for instance, V. Bergeron *et al* [Bergeron 2000] claimed that the retraction of the sheet is impeded due to the elongational viscosity. By performing the experiments with polymeric drops on a hot plate above the Leidenfrost temperature and on a small solid target V. Bertola [Bertola 2009] and A. Rozhkov *et al* [Rozhkov 2003] respectively showed that the role of elongational viscosity is negligible. D. Bartolo *et al* [Bartolo 2007] alternatively suggested that the retraction of the sheet can be curtailed by the non-Newtonian normal stresses that developed due to the presence of polymer. But more recent studies have shown that inhibition in the rebound may be due to the

interaction of polymer chains with the substrate that enhances the friction at the contact line during the retraction [Smith 2010, Zang 2013, Smith 2014, Bertola 2015, Huh 2015]. In addition, there have been studies on yield-stress fluids by L.H. Luu *et al* [Luu 2009, Luu 2013] to study the maximum expansion of microgel suspension (carbopol) on impacting a smooth glass surface, a rough hydrophobic surface, and a small solid target. They found that for impact on a smooth glass substrate, the maximal spread factor λ scales as $M^{1/3}$, M being the Mach number and for an impact on small solid target (perfect slip condition) $\lambda \sim M$. In another study using yield stress fluids, S. Chen *et al* [Chen 2016] explain that the maximum diameter of the sheet is dominated by the inertial force and thus scales as Weber number We . They also showed that, for higher yield stress, the deformation of the sheet becomes permanent due to the inability of the surface forces to retract the sheet.

We have used two experimental set-ups to investigate the maximum deformation of a sheet produced by the impact of viscoelastic drops. The first set-up is based on drop impacting a small solid target and the sheet freely expands in air. Despite the diameter of the target is comparable to the drop diameter we have shown that viscous dissipation occurs due to the finite contact between the expanding sheet and solid target [Arora 2016]. The second set-up is based on the principle of inverse Leidenfrost effect and the gaseous vapor layer that forms when a drop impacts the surface covered with a layer of liquid nitrogen leads to a substantial suppression of shear dissipation [Antonini 2013]. We have shown that if the impact velocity is replaced by the effective velocity, the maximal spread factor obeys the scaling law $\lambda \sim v_{\text{eff}}/U^*$, which is analogous to the one we have previously and experimentally checked for elastic beads (Chapter 4). Here, v_{eff} is the velocity of the sheet measured at the exit of the target and U^* is the velocity of generalized elastic deformations. We have also checked the validity of the scaling for viscous fluids. In the case of minimal dissipation, $v_{\text{eff}} = v_o$ and when shear dissipation occurs $v_{\text{eff}} < v_o$. Overall, we have quantitatively rationalized the spreading dynamics of impacting drops and beads for viscous, viscoelastic and elastic materials by taking surface elasticity, bulk elasticity, and viscous dissipation into account.

We have also observed cracks in the interior of the sheet produced by the impact of viscoelastic drops whose relaxation time is higher than the experimental time. Fracture occurs when the sample is deformed at rates larger than the inverse of its relaxation time. This has been shown in previous experiments for the same type of samples but in different experimental conditions [Ligoure 2013]. Cracks have been observed in the gap of a shear cell (pure shear flow [Tabuteau 2009]), in a pendant drop experiment (pure extensional flow [Tabuteau 2008]) and in Hele-Shaw cell (complex flow involving both shear and extensional flows [Foyart 2013]). Interestingly, E. Miller *et al* [Miller 2005] and J.C. Thompson *et al* [Thompson 2007] have observed similar internal failures within viscoelastic fluid sheets produced by impinging jets. For their experiments, they used wormlike micelles and observed that, with the increase of sample elasticity and above a critical flow rate, the number and growth of holes increase. They referred these multiple

rupture events as fluid webs. Viscoelasticity also affects the symmetry of impacting jets, unlike Newtonian fluids that preserve the radial symmetry [Lhuissier 2014]. In our case, the rupture in the sheet occurs above the percolation threshold of bridged microemulsions and we have observed the fracture in the sheet in both kinds of experiments (Inverse Leidenfrost condition and solid target). Initiation of the cracks is a stochastic process and can occur during expansion or retraction of the sheet. As an attempt to rationalize the cracks within the sheet, we have quantified the heterogeneity of the thickness of the sheet by measuring the relative fluctuations of the thickness of the sheet. Although this approach seems promising at this stage, it is unfortunately not sufficient to fully understand the occurrence of cracks in the freely expanding sheets of viscoelastic fluids having relaxation time higher than the lifetime of the sheet.

Brittle Fracture of Polymer Transient Networks

Contents

6.1	Experimental samples and techniques	101
6.2	Linear viscoelasticity	102
6.3	Modes of rupture of the filaments	105
6.3.1	State diagram	105
6.3.2	Non-linear extensional rheology	105
6.3.3	Crack imaging	108
6.3.4	Crack opening profiles	110
6.4	Discussion	110
6.5	Conclusion	113

In this chapter, we study the fracture of reversible double transient networks, constituted of a water suspension of entangled surfactant wormlike micelles reversibly linked by various amounts of telechelic polymers. We provide a state diagram that delineates the regime of fracture without necking of the filament from the regime where no fracture or break-up has been observed. We show that filaments fracture when stretched at a rate larger than the inverse of the slowest relaxation time of the networks. We quantitatively demonstrate that dissipation processes are not relevant in our experimental conditions and that, depending on the density of nodes in the networks, fracture occurs in the linear viscoelastic regime or in a non-linear regime. In addition, analysis of the crack opening profiles indicates deviation from a parabolic shape close to the crack tip for weakly connected networks. We demonstrate a direct correlation between the amplitude of the deviation from the parabolic shape and the amount of non-linear viscoelasticity.

6.1 Experimental samples and techniques

We investigate self-assembled transient networks consisting of a semi-dilute solution of surfactant wormlike micelles eventually reversibly cross-linked by telechelic polymers. We use a mixture of cetylpyridinium chloride (CpCl) and sodium salicylate (NaSal) with

a NaSal/CpCl molar ratio of 0.5 dispersed in brine (0.2 M NaCl). This mixture is known to form long and flexible surfactant cylindrical micelles. The sample eventually comprises home-synthesized triblock telechelic polymer, which has a poly(ethylene oxide) (PEO) hydrophilic backbone (molecular weight 10,000 g mol^{-1}) with hydrophobic aliphatic chains grafted at both ends, C_nH_{2n+1} , where $n = 23$. The samples are prepared by weight and mass fraction of micelles φ is fixed at 10%, with the amount of polymer β varied between 0 and 55%.

Shear rheology is used to investigate the sample viscoelasticity as explained in Chapter 2 (section 2.2.1). To measure the mechanical response of the samples under an extensional deformation flow field, a VADER 1000 (versatile accurate deformation extensional rheometer) from Rheo Filament ApS [Huang 2016b] is used. This has been explained in detail in Chapter 2 (section 2.2.2). In our experiments, different strain rates, in the range (0.03 – 2) s^{-1} , are applied to measure the response of the viscoelastic materials in the viscous and elastic regimes. The maximum Hencky strain reported is about 3. The main reason for this limitation is the noise in the force signal for values less than about 10^{-3} N (corresponding to 0.1 g). All experiments are performed at $T \approx 25^\circ\text{C}$.

The imaging of a filament during its stretching is performed using a high-speed camera (Photron Mini UX100) coupled with the VADER 1000 rheometer [Huang 2016a] as explained in Chapter 2 in section 2.2.2. The images are analyzed using the technique explained in section 2.4.

6.2 Linear viscoelasticity

The composition of the samples is varied to tune their viscoelasticity. A simple wormlike micelles solution (without telechelic polymer, $\beta = 0$) behaves as a pure Maxwell fluid and is characterized by a shear plateau modulus G_0 and a unique characteristic relaxation time τ . G_0 is related to the mesh size of the network of wormlike micelles, and τ is the geometric mean of the characteristic time for breaking/recombination and the characteristic time for reptation [Cates 1987]. These parameters are obtained by fitting the frequency dependence of the storage, G' and loss modulus G'' with their theoretical expressions for a Maxwell fluid. Samples comprising telechelic polymers behave as two-mode Maxwell fluids, resulting from the coexistence of two coupled networks [Nakaya-Yaegashi 2008], one related to the bridging of the micelles by the telechelic polymers (elastic plateau G_{fast} , relaxation time τ_{fast}) and another related to the micelle entanglement (elastic plateau G_{slow} , relaxation time τ_{slow} with $\tau_{\text{slow}} > \tau_{\text{fast}}$). Here, the elastic plateau modulus is the sum of the elastic moduli of the fast and slow modes, $G_0 = G_{\text{slow}} + G_{\text{fast}}$.

Figure 6.1a shows the frequency dependence of G' and G'' together with the Maxwell fits (one-mode Maxwell fluid for pure wormlike micelles, $\beta = 0$, and two-mode Maxwell fluid otherwise), which account very well for the experimental data. Figure 6.1b summarizes the evolution with the amount of telechelic polymer, β , of the rheological character-

istics of the samples as extracted from the fits. The shear plateau modulus, G_0 , increases monotonically with the amount of telechelic polymer, β , from 170 Pa in the absence of polymer to 4600 Pa for $\beta = 55\%$. Similarly, both relaxation times continuously increase with β . The characteristic relaxation time τ_{slow} of the micelles network increases from 0.6 s without polymer up to 7 s, for $\beta = 55\%$. The faster relaxation time, related to the network of telechelic polymers, is systematically about one order of magnitude smaller

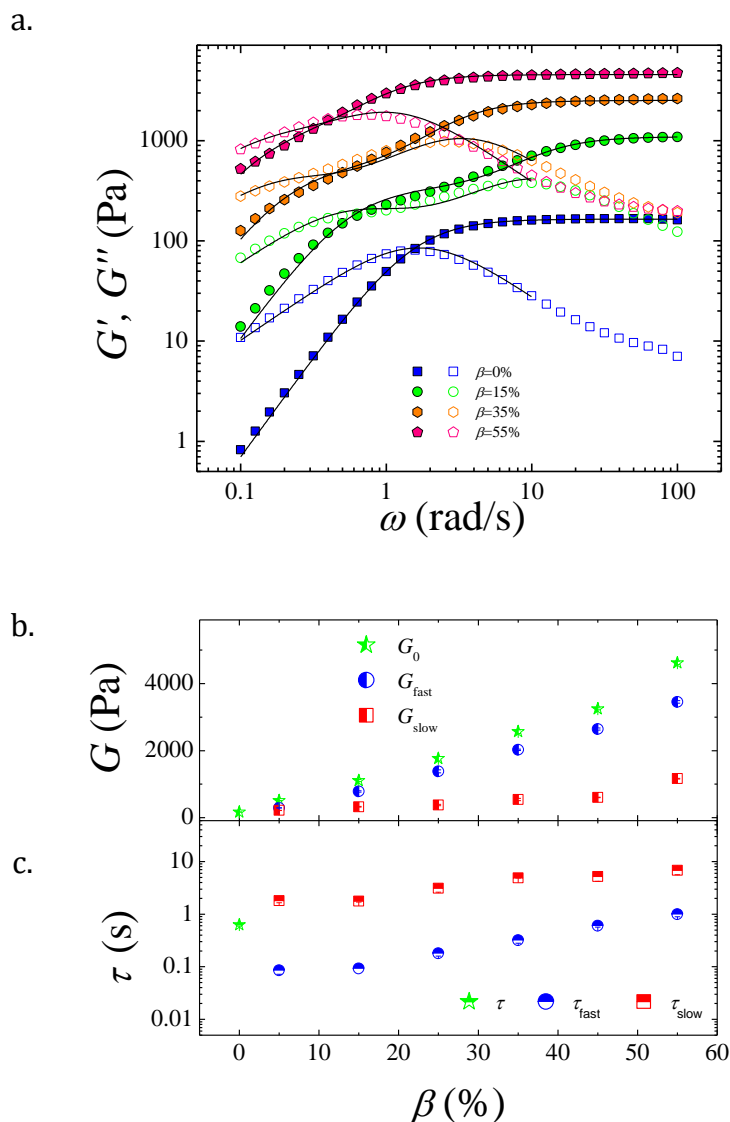


Figure 6.1: Linear shear rheology for samples with various polymer concentrations, β , as indicated in the legend. (a) evolution of the storage and loss moduli with frequency. The symbols are the experimental data points and the continuous lines are the fit with a one-mode (for $\beta = 0$) and a two-mode (for $\beta \neq 0$) Maxwell fluid models. (b,c) Fit parameters, (b) elastic moduli and (c) characteristic relaxation times as a function of β .

than the slower one. Note that, although the slow mode is related to the network of wormlike micelles, its rheological characteristics (G_{slow} , τ_{slow}) are measured to continuously increase with the amount of telechelic polymer, demonstrating a coupling between the two networks.

On the other hand, the Young modulus can be measured using extensional rheology. This requires data to be acquired at a sufficiently large extensional rate $\dot{\varepsilon}$ as compared to the slowest relaxation time so that viscous dissipation is not relevant. Figure 6.2a shows the growth of the measured stress σ as a function of the strain $\varepsilon = \dot{\varepsilon}t$, with $\dot{\varepsilon}$ the imposed extension rate and t the time elapsed since the sample is strained. In the limit of small deformation, σ is found to be proportional to ε , as expected from linear elasticity: $\sigma = E\varepsilon$, where the proportionality constant is the Young modulus E (Figure 6.2a). The Young modulus is measured by fitting the experimental data at small deformation. We find that E increases from 850 to 11600 Pa as β increases (Figure 6.2b). We measure that $E \simeq 3G_0$ as expected for an isotropic incompressible material.

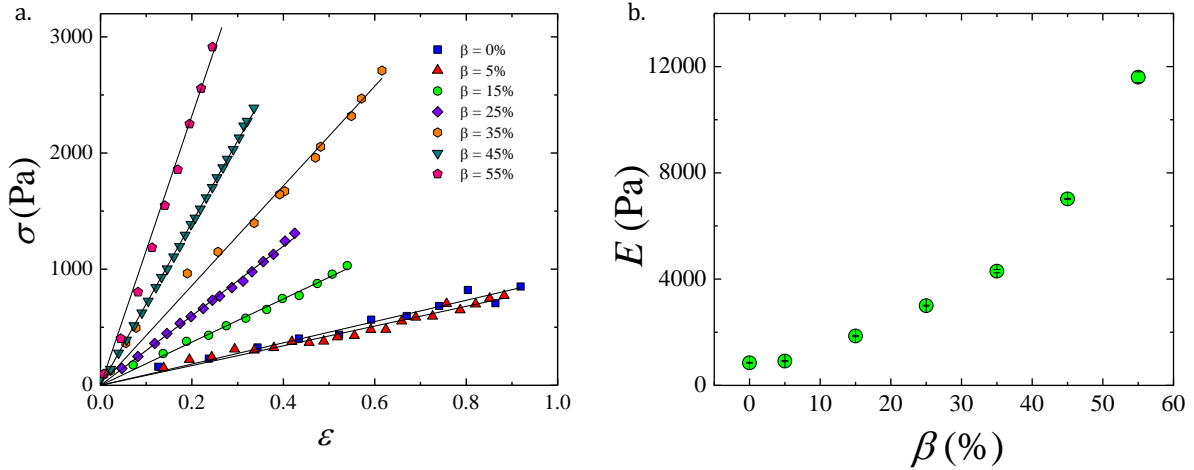


Figure 6.2: (a) Extensional stress as a function of the Hencky strain, ε , in the linear regime (small ε), for samples with various polymer concentrations, β , as indicated in the legend. The symbols are experimental data points and the lines are linear fits whose proportionality constant is the elastic modulus, E . Data have been acquired in the elastic regime (with Wi in the range (1-4) depending on the samples). (b) Young's modulus E , as a function of β is plotted.

6.3 Modes of rupture of the filaments

6.3.1 State diagram

We perform extensional rheology measurements using the feedback loop to ensure constant extensional rates, $\dot{\epsilon}$, for samples with various copolymer contents, β . Because samples differ by their characteristic relaxation times (as shown in Figure 6.1c), the relevant quantity is not $\dot{\epsilon}$ but the Weissenberg number, defined as $Wi = \dot{\epsilon}\tau$ for one-mode Maxwell fluid and as $Wi = \dot{\epsilon}\tau_{\text{slow}}$, for two-mode Maxwell fluids. In our experiments, Wi is varied over about two orders of magnitude (from 0.1 to 9.5). Visualization of the filament during its extension indicates two distinct types of material behavior: either a continuous liquid-like thinning up to the maximum Hencky strain $\epsilon_{\text{max}} \approx 3$ or by solid-like fracturing without necking [Tripathi 2006, Tabuteau 2009] at a Hencky strain below ϵ_{max} . Note that elastocapillary break-up [Eggers 1997, Anna 2001] is not observed for Hencky strains less than 3. Clearly the thinning cannot continue to arbitrarily large Hencky strains since capillary forces must ultimately dominate as the radius tends to zero. However, the resulting capillary break-up is not the object of the present study. For all experimental conditions, therefore, the behavior of the filament under a constant elongation rate is categorized into one of these two classes, liquid-like (thinning) or solid-like (fracture).

All data are reported in a schematic state diagram (Figure 6.3) where Wi is plotted as a function of β . We observe that the filament thins continuously at low Wi and cracks at a finite thickness (without necking) at higher Wi . The transition from continuous flow to filament rupture is similar to previous experimental observations on wormlike micelle [Bhardwaj 2007] and associating polymer [Tripathi 2006] viscoelastic solutions. Remarkably, for all samples investigated here, the transition from thinning to fracturing occurs for a comparable critical Weissenberg number $Wi_c \approx (0.5-0.6)$. This experimental result follows remarkably well with the theoretical Weissenberg criterion [Malkin 1997] for the rupture of polymeric liquids in extension with a constant strain rate that predicts $Wi_c = 0.5$ for an elastic (upper convected Maxwell) liquid, and $Wi_c = 0.5/(1 - \mathcal{E})$ with $0 \leq \mathcal{E} < 1$ that parameterizes non-affinities.

6.3.2 Non-linear extensional rheology

To assess the importance of non-linearity, we compare the time dependence of the transient extensional viscosity, or tensile stress growth coefficient, η_E^+ , to the linear viscoelasticity expectations. As an illustration, data acquired at different extensional rates for two samples differing by their amount of copolymer, $\beta = 5\%$ (Figure 6.4a) and $\beta = 55\%$ (Figure 6.4b), are displayed together with the linear viscoelastic expectations computed thanks to the linear viscoelastic parameters determined using a shear rheometer. For a two-mode Maxwell fluid, linear viscoelasticity predicts that η_E^+ continuously increases

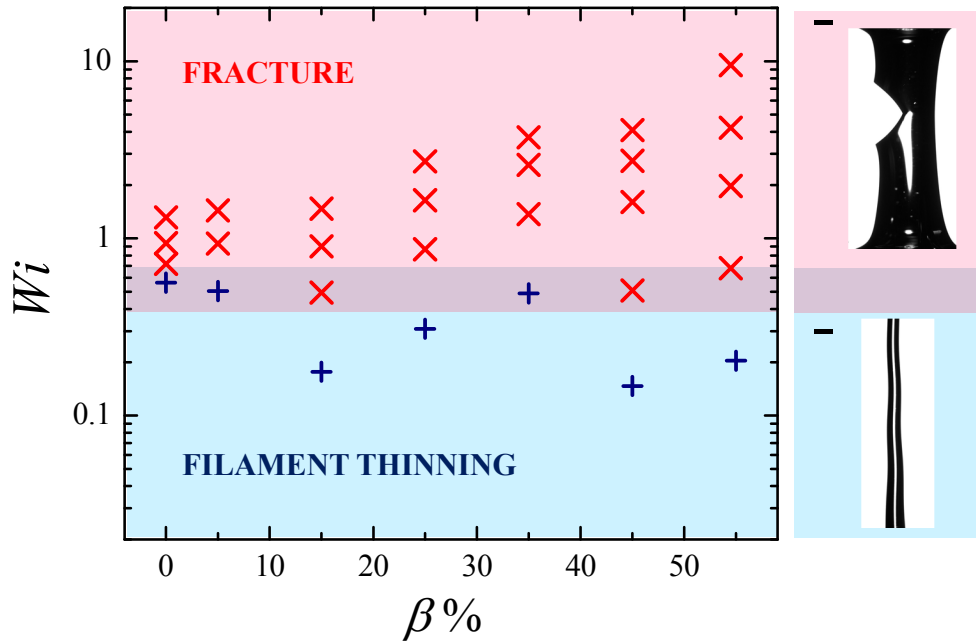


Figure 6.3: Schematic state diagram, Weissenberg number, Wi , as a function of the amount of telechelic polymers in the sample. The symbols correspond to the experimental configurations investigated. The two regimes, continuous thinning at low Wi , and fracturing without necking at high Wi , are shown. Representative images of the filament corresponding to the two regimes are displayed. For the top image (crack), $\beta = 25\%$ and $\dot{\epsilon} = 1\text{ s}^{-1}$, and for the bottom image (capillary thinning), $\beta = 0$ and $\dot{\epsilon} = 1\text{ s}^{-1}$. Scale bars: 1 mm.

with time until reaching a plateau for a time larger than the inverse of the slowest relaxation time, τ_{slow} . We measure that, at an early stage of time, the extensional rheology data follow the expected linear viscoelastic behavior. The nice quantitative agreement ensures the reliability of the two sets of measurements. In addition, we measure that crack occurs at a time t_c that decreases as the imposed extensional rate $\dot{\epsilon}$ increases, such that the cumulated strain experienced by the sample, $\dot{\epsilon} t_c$, is roughly constant (of the order of 1). The marked difference between the two samples lies in the fact that for one sample the fracture occurs nearly in the linear regime ($\beta = 55\%$, Figure 6.4b), whereas the other sample exhibits a significant departure from the linear behavior before fracturing ($\beta = 5\%$, Figure 6.4a).

The crucial role of the sample structure on the non-linear viscoelastic behavior is also clearly seen in Figure 6.5, where data for samples with different amounts of telechelic polymers are plotted together. To account for the varying elasticities, the measured stress, σ , is normalized by the modulus, E , as measured in the short time regime, at small strain ϵ . By definition, data collapse at smaller strains. Although all samples crack at a similar strain of the order of 1, they do so in very different manner: the sample with

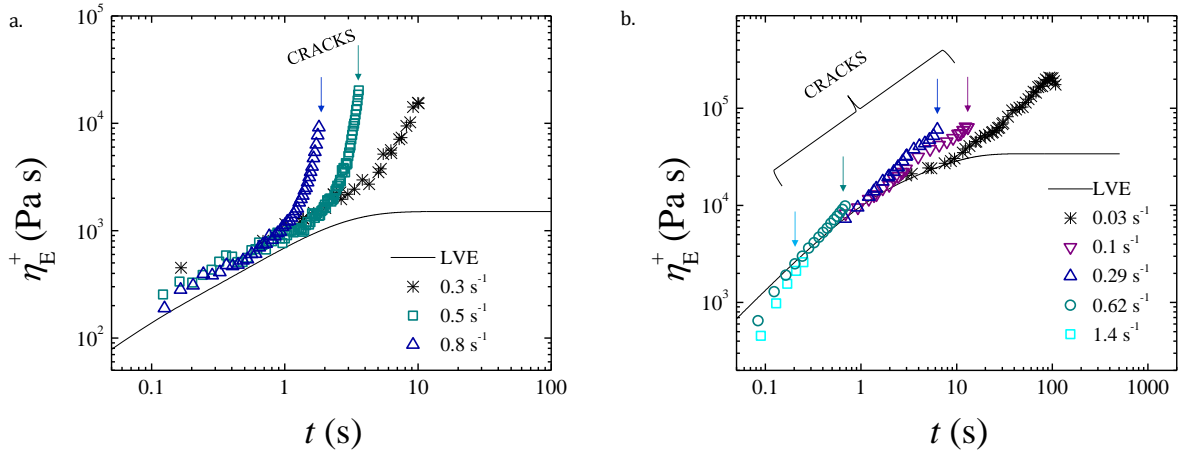


Figure 6.4: Extensional stress growth coefficient, for two samples with (a) $\beta = 5\%$ and (b) $\beta = 55\%$ and for various extensional rates, as indicated in the legends. The symbols are experimental data points and the continuous lines are the theoretical expectations for linear viscoelasticity. Black crosses correspond to filament thinning and colored symbols correspond to cracks. The arrows indicate the time when fracture occurs.

a large amount of polymer seems to fracture more or less in the linear viscoelastic regime whereas the sample comprising of a small quantity of polymer exhibits large deviation from the linear regime before fracturing. More quantitatively, we measure the stress, σ_c , and the strain, ε_c , at which the sample fractures. For a given sample, we find that in the range of extensional rates $\dot{\varepsilon}$ investigated, ε_c and σ_c only weakly depend on $\dot{\varepsilon}$, as previously observed for pure wormlike micelles solutions [Rothstein 2003, Bhardwaj 2007]. We define $\chi = \frac{\sigma_c}{E\varepsilon_c}$, which quantifies non-linearity. For a sample that breaks in the linear viscoelastic regime, one expects $\sigma_c = E\varepsilon_c$, hence $\chi = 1$. For a sample that strain-hardens, $\chi > 1$. We report in the inset of Figure 6.5 the evolution of χ with the amount of telechelic polymer, β , where data acquired at different $\dot{\varepsilon}$ are averaged. We find that χ decreases as β increases, from values larger than 5 for the sample with a small amount of polymer down to values in the order of 1 for $\beta \geq 45\%$.

Thus, weakly connected samples (i.e. sample containing low amount of telechelic polymers) exhibit significant strain-hardening before fracture, whereas more connected samples break in the linear viscoelastic regime. Note that the numerical value found here for a sample without telechelic polymer is in agreement with the one measured in [Bhardwaj 2007] for a comparable system.

Hence, extensional rheology demonstrates that, although all samples display qualitatively similar linear viscoelastic behavior (which can be well accounted by a Maxwell model), they present very different non-linear viscoelastic behaviors and fracture processes can occur in the linear regime ($\chi \approx 1$) or after a significant strain-hardening ($\chi > 1$) depending on the sample connectivity.

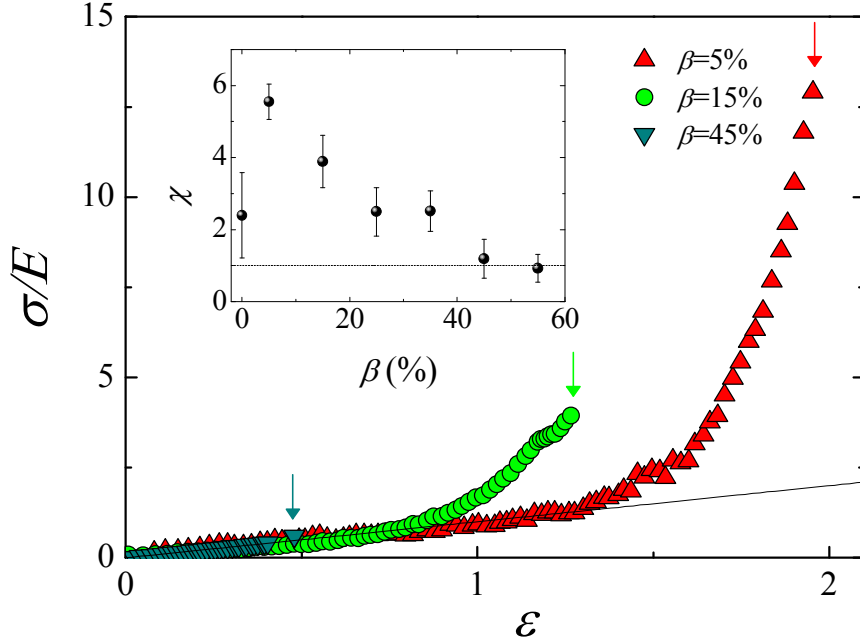


Figure 6.5: Extensional stress normalized by the Young modulus measured in the linear regime at low strain (Figure 6.2a) as a function of the strain, for samples with different amount of telechelic polymers, β , as indicated in the legend. For all samples, the strain rates have been adjusted such that $Wi \sim 1$. The symbols are the experimental data points and the continuous line is the linear regime expectation $\sigma/E = \epsilon$. Fracture occurs at σ_c and ϵ_c . Inset: Variation of $\chi = \frac{\sigma_c}{E\epsilon_c}$ with β . The dotted line indicates the linear viscoelastic regime.

6.3.3 Crack imaging

To better understand the links between the sample structure, the non-linear extensional rheology, and the fracture process, we use a fast camera to image the cracks during the extension of a filament at a prescribed rate. Figure 6.6 displays a representative time series during the crack propagation of a sample with $\beta = 25\%$. Cracks are imaged for various samples with β ranging from 15 to 55%. In all cases, a single crack is formed that systematically propagates straight, perpendicularly to the extension direction.

By tracking the crack tip, the instantaneous velocity of the crack, U_C , can be measured. To account for the various elastic moduli of the samples considered here, data have to be compared with the shear wave sound velocity, U_S , of each sample. For a solid of shear modulus G_0 , $U_S = \sqrt{G_0/\rho}$, with ρ the sample density. For the samples investigated here, U_S varies between 1 and 2 m/s. Figure 6.7 displays for all samples the crack velocity normalized by the sound velocity, U_C/U_S . U_C/U_S increases steadily and reaches a plateau value more or less when the crack length becomes comparable to half the filament diameter ($\zeta = 0.5$). The cracks propagate fast as the steady state value

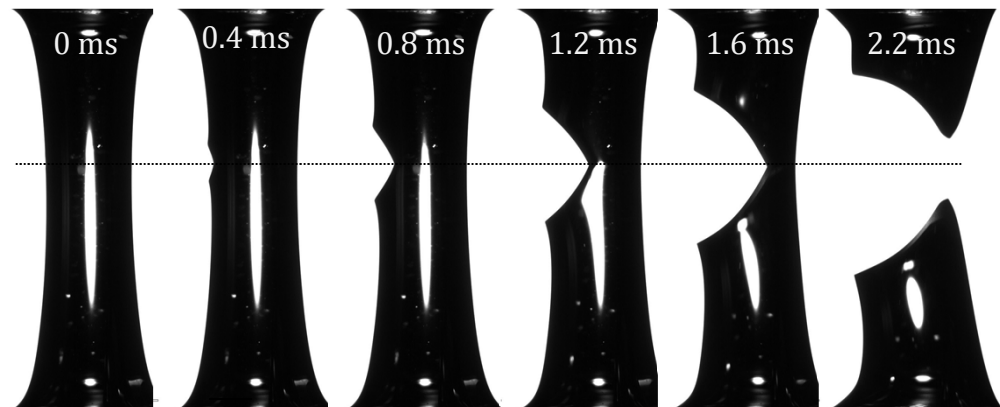


Figure 6.6: Time series of a crack propagating in a sample with $\beta = 25\%$ and strain $\dot{\epsilon} = 1\text{ s}^{-1}$. The scale bar is 1 mm.

is comparable to the shear wave velocity (U_C/U_S ranges between 0.5 and 1). Finally, we mention that cracks propagate fast but do not oscillate (as opposed to the finding of [Deegan 2001, Livne 2007]) probably because cracks travel over very short distances in our experiments.

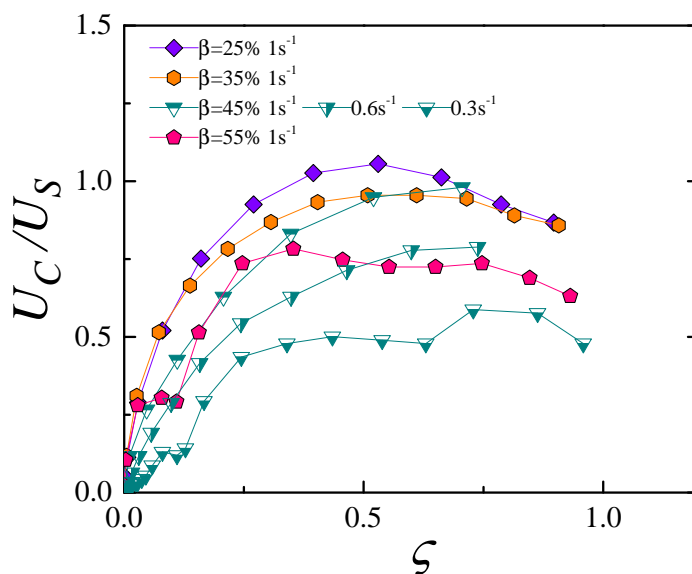


Figure 6.7: Velocity of the crack tip as a function of the run distance, for samples with different amounts of telechelic polymers and different strain rates, as indicated in the legend. The velocity is normalized by the shear wave sound velocity and the distance by the total thickness of the filament, such that $\zeta = 0.5$ correspond to the mid-filament.

6.3.4 Crack opening profiles

An interesting feature concerns the crack opening profiles. As shown in Figure 6.8, the crack shape might depart significantly from the parabolic shape theoretically expected with the use of finite elasticity theory required for such soft materials [Tabuteau 2011], and displays close to its tip a wedge profile. The deviation from the parabolic shape is quantified by the length ℓ extracted from a fit of the profile of a crack (whose tip is positioned at $x = 0, y = 0$) with the functional form $y = \ell + ax^2$. The fit shown as red lines in Figure 6.8 account very well for the experimental data and yield numerical values for ℓ between 0.017 and 0.2 mm, and for a between 0.42 and 0.76 mm⁻¹.

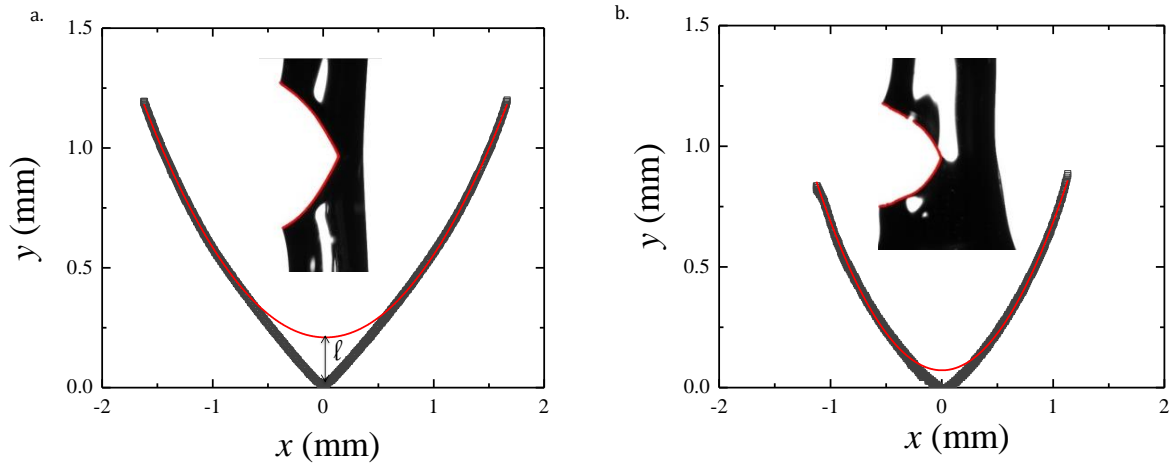


Figure 6.8: Crack opening profiles are measured when the cracks have propagated over a distance equal to half the filament thickness for a sample with $\beta = 15\%$ (a) and 55% (b). The grey symbols are the experimental data points and the thin red lines correspond to the fit of the profile with a parabola, allowing the determination of the distance ℓ .

This type of profile has already been observed experimentally in elastomers and permanent gels [Deegan 2001, Livne 2008, Goldman 2012, Morishita 2016]. Similarly, to the previous works, we find that overall ℓ increases as the propagation velocity of the crack increases (Figure 6.9).

6.4 Discussion

The samples investigated here are viscoelastic fluids, characterized by one (or two) relaxation times. We observe (Figure 6.3) that they fracture only if they are submitted to an extensional strain larger than the inverse of their longest relaxation time ($Wi \geq 1$). Hence we expect that for the large strain rates viscous dissipations are negligible. This is in accordance with the fact that the cracks propagate at very large speed, comparable

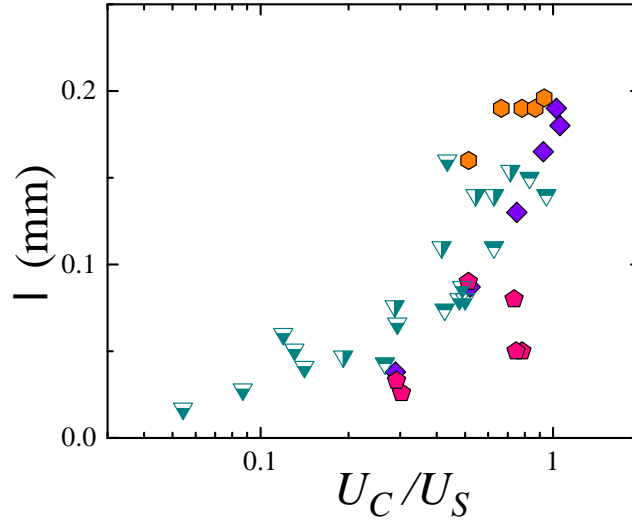


Figure 6.9: Length l as a function of the velocity of the crack tip normalized with the speed of the shear wave, for samples with different amounts of telechelic polymers and different strain rate. The symbols are the same as in Figure 6.7.

to the shear wave velocity for a solid. More quantitatively, to check whether viscoelastic effects do play a role or not in the crack propagation, one has to compare the length over which the crack propagates L and the length $l = U_C \tau_{\text{slow}}$ over which viscoelastic effects are relevant [De Gennes 1988, De Gennes 1996]. In our experiments, the crack velocity in the steady state (at mid-filament) U_C is typically in the order of 1 m/s and the slow relaxation time of the network τ_{slow} is in the range (2 – 7) s. These values yield a length $l = U_C \tau_{\text{slow}}$ that ranges between 2.5 and 11 m, while the radius of the filament, that dictates the length L over which the crack propagates, is typically of 1 mm. Hence in all cases, l is several orders of magnitude larger than L , ensuring that viscous effects are not relevant. This is consistent with the fact that at large distance the crack is parabolic and does not exhibit the $x^{3/2}$ scaling predicted by the viscoelastic trumpet model [De Gennes 1996] and experimentally measured in the adhesive fracture of a polymer melt [Saulnier 2004] and in polymer liquid under tension [Huang 2016a]. In addition, because the samples investigated here are very soft and strained elastically over very large deformation, they can be considered as hyperelastic. The importance of hyperelasticity in the vicinity of the crack tip may play an important role in the dynamics of fracture [Buehler 2003, Buehler 2006]. The characteristic size over which very large strains are involved close to the crack tip reads $R_{\text{tip}} \approx \Gamma/G_0$ with G_0 the shear modulus and Γ the fracture energy which can be approximated in the framework of finite elasticity as $\frac{\pi G_0}{4a}$ [Hui 2003] (with a the radius of curvature of the crack tip, extracted from the parabolic fit of the crack profile). Hence $R_{\text{tip}} \approx 1/a$, and ranges in our experiments between 1.3 and 2.4 mm. In addition to the criterion given above, the

generalization of the viscoelastic trumpet model to hyperelastic materials dictates that $\frac{R_{\text{tip}}}{L} \frac{L}{l}$ must be small [Tabuteau 2011] to ensure that viscous dissipations are negligible. In our experiment R_{tip} is comparable to L and $L \ll l$, hence $\frac{R_{\text{tip}}}{L} \frac{L}{l} \ll 1$, and viscous dissipation is expected to be negligible. All these experimental facts show that filaments always fracture in the elastic limit and that dissipation is not relevant in the process. Hence, despite the samples being viscoelastic, the fractures are brittle in the experimental conditions considered here.

Our results can therefore, be put in parallel with experiments on solid samples. The peculiar opening profile of the cracks that we measure has been previously observed, but only in elastomers [Deegan 2001, Livne 2008, Goldman 2012, Morishita 2016]. Livne *et al* pointed out the importance of non-linear elasticity close to the crack tip for the investigated soft incompressible elastomers (elastic moduli in the range 33 – 190 kPa). They demonstrated that the length ℓ is not related to dissipative processes, i.e. ℓ cannot be regarded as a characteristic length of a process zone, and argued indirectly that ℓ is related to finite elasticity. More recently, a correlation has been experimentally shown between ℓ and the hyperelasticity measured independently for elastomers filled with various amounts of carbon black [Morishita 2016].

Our data allows us to check for a direct correlation between the shape of the opening profile and the sample non-linear viscoelasticity. As discussed above, the non-linear viscoelasticity can be quantified with $\chi = \frac{\sigma_c}{E \varepsilon_c}$, where σ_c , resp. ε_c , is the stress, resp. the strain at which a crack nucleates and E is the sample modulus. We show in Figure 6.10a that ℓ is rather small (of the order of 0.08 mm) when the samples cracks in the linear viscoelastic regime ($\chi \approx 1$) and continuously increases with χ , directly demonstrating the correlation between the amount of non-linear viscoelasticity and the departure from the parabolic shape of the crack profile. It is interesting to compare ℓ to the characteristic length of the fracture process, $\mathcal{L} = \frac{U_C}{\dot{\varepsilon}}$, where U_C is the speed of the crack and $\dot{\varepsilon}$ is the rate at which the filament is strained. The plot of the non-dimensional length $\frac{\ell}{\mathcal{L}}$ varies monotonically with χ (Figure 6.10b). Intriguingly, we find that $\frac{\ell}{\mathcal{L}}$ varies as a power law with $\chi - 1$ with an exponent 1/3, suggesting a critical phenomenon (inset Figure 6.10b).

As a final remark, we wish to discuss our results in light of the sample structure. On the time and length scales considered here, the samples can be considered as blends of two coupled networks. One network is formed by the entangled wormlike micelles and the other one is formed by the telechelic polymers that link the wormlike micelles. We have investigated a family of samples such that the network of wormlike micelles is kept constant and the density of the network of telechelic polymers is varied, as β changes. Our results show that double networks with a loose telechelic network strain hardens before fracturing. By contrast, when the telechelic polymer network is denser, the sample does not strain harden but fractures in the linear regime. Our findings, therefore, suggest that the capacity to strain harden is a specific feature of the worm-

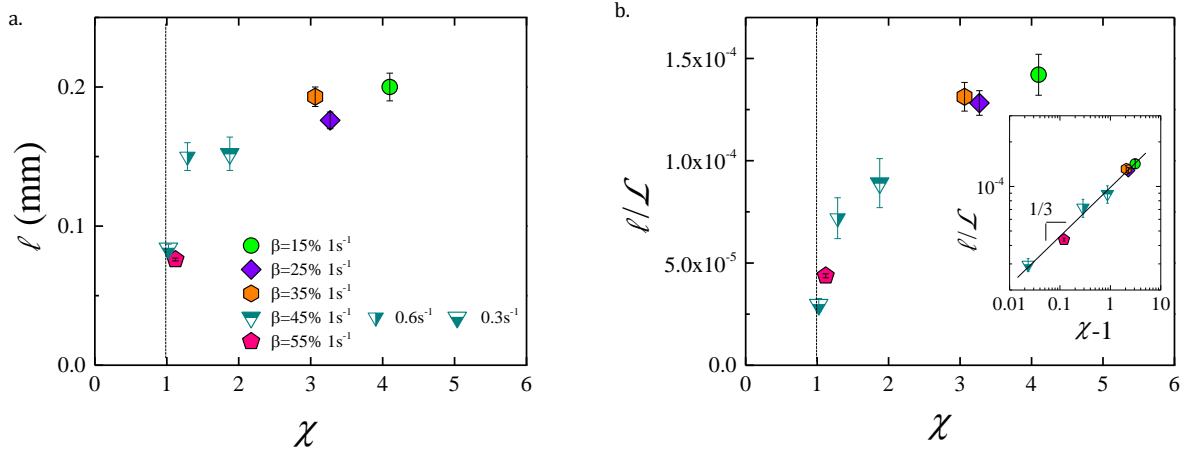


Figure 6.10: Correlation between the non-linear viscoelasticity quantified by $\chi = \frac{\sigma_c}{E\epsilon_c}$ and the departure from the parabolic shape quantified by (a) the length l , (b) the normalized length $\frac{l}{L}$. The dotted lines indicate linear viscoelasticity. Inset: normalized length as a function of $\chi - 1$ in a log-log plot. The best fit yields a powerlaw with an exponent $1/3$.

like micelles network, which may be impeded to do so due to the strong coupling with the telechelic network. This physical picture is consistent with experiments on various wormlike micelle systems. Indeed, for entangled wormlike micelles solutions, considerable strain hardening has been measured and modeled by the finitely extensible nonlinear elastic (FENE-PM) model which accounts for the finite extensibility of the wormlike micelles regarded as Gaussian chains [Walker 1996, Rothstein 2003]. Interestingly, Rothstein et al. [Rothstein 2003, Bhardwaj 2007] have also measured a decrease of the strain hardening when the concentration of wormlike increases, in agreement with our experimental observations, due to the increase in the density of elastic nodes.

6.5 Conclusion

We have investigated the fracture processes in self-assembled double transient networks by combining fast imaging to a filament stretching rheometer. The networks break elastically without necking when deformed at a rate larger than the inverse of their lowest characteristic relaxation time. We have rationalized the non-relevance of viscous dissipation effects and from the analysis of the crack opening profile, we have evidenced for the first time, for viscoelastic fluids and in filament breaking experiments a departure at the crack tip from the parabola expected from linear viscoelasticity. Thanks to the unique coupling in one single experiment between rheological measurements and crack opening profile characterization, we have provided a direct evidence of a correlation between the non-linear viscoelasticity and the shape of the crack profile close to the tip. By varying the composition, we have tuned the sample viscoelasticity and have found that samples

with dense networks of elastic nodes break in the linear regime whereas samples with a loose network of nodes exhibit significantly strain-hardening before fracturing.

General Conclusions and Perspectives

During my PhD project, I have performed two different kinds of experiments to study the effect of large deformations on various gels. One class of experiments aims to study freely expanding sheets produced by the impact of liquid drops, viscoelastic drops and elastic beads on solid surfaces. These expanding sheets undergo large extensional deformations. The second class of experiments aims to investigate the extensional stretching deformation and fracture of viscoelastic fluids using a filament stretching rheometer coupled to a fast camera.

Freely expanding sheets

We have investigated freely expanding sheets produced by impacting viscous and viscoelastic drops on a small solid target of size comparable to that of the drops. To do so, we used Newtonian fluids of glycerol/water mixtures and viscoelastic fluids that consist of self-assembled transient networks (surfactant spherical micelles and surfactant-stabilized oil droplets suspended in water reversibly linked by telechelic polymers). The sample composition is varied to tune the viscoelastic behavior. Below a percolation threshold micelles and microemulsions behave as Newtonian fluids. Above the percolation they are viscoelastic and behave as simple Maxwell fluids. We have characterized the percolation threshold, the zero shear viscosity η_0 , the shear plateau modulus G_0 and characteristic relaxation time τ of the Maxwell fluids by standard linear rheological measurements.

The Ohnesorge number that compares the viscous forces to inertial and surface forces, $Oh = \frac{\eta_0}{\sqrt{\rho\gamma d_o}}$ is the relevant parameter to classify the behavior of viscous drops upon impact. Here ρ is the sample density, η_0 is the zero-shear viscosity, γ is the surface tension and d_o is the drop diameter. Figure A summarizes our main experimental findings. We have found that, for viscous droplets and for small Oh , the maximal spread factor λ is governed by the balance between inertia and surface tension, whereas for higher Oh viscous effects play an important role. We have used a simple model of the sheet expansion where inertia, surface tension and viscosity are considered to explain the maximal deformation of the sheet. To take into account the viscous effects on λ , we have defined an effective impact velocity v_{eff} which is reduced compared to the real impact velocity. We have measured v_{eff} by taking the time derivative of the diameter of the sheet d at short time i.e. when the size of the sheet becomes larger than the size of the target. A simple model based on an effective energy conservation where the impact velocity has been replaced by the effective velocity has been successfully used to account for our experimental results. The quantitative agreement between the model and the experiments shows that the dissipation mainly originates from viscous shear on the small surface of the target and that, when the sheet freely expands in air, extensional viscous dissipation is negligible.

In the case of viscoelastic fluids a relevant parameter is the Deborah number, De , defined as the ratio between the characteristic relaxation time τ , and the lifetime of the sheet ($\tau_{\text{life}} \sim 10$ ms). When $De \ll 1$, we find that upon impact Maxwell fluids, behave as simple Newtonian fluids with zero-shear viscosity $G_0\tau$. For samples for which $De > 1$, the departure from the Newtonian case can be accounted for by the sample viscoelasticity. Interestingly, the dynamics of viscoelastic sheets produced with Maxwell fluids whose characteristic relaxation time is much larger than the lifetime of the sheet ($De \gg 1$), the expansion drastically differs from those of other samples. The sheet expands much more than viscous sheets with comparable zero shear viscosity. In addition, the expansion of the sheet is highly heterogeneous and displays cracks and holes, revealing the sample elasticity. We have shown that the cracks observed in viscoelastic sheets for $De \gg 1$ are the consequence of the sample elasticity. A more quantitative analysis would however be needed to fully understand and model the nucleation and growth of the cracks.

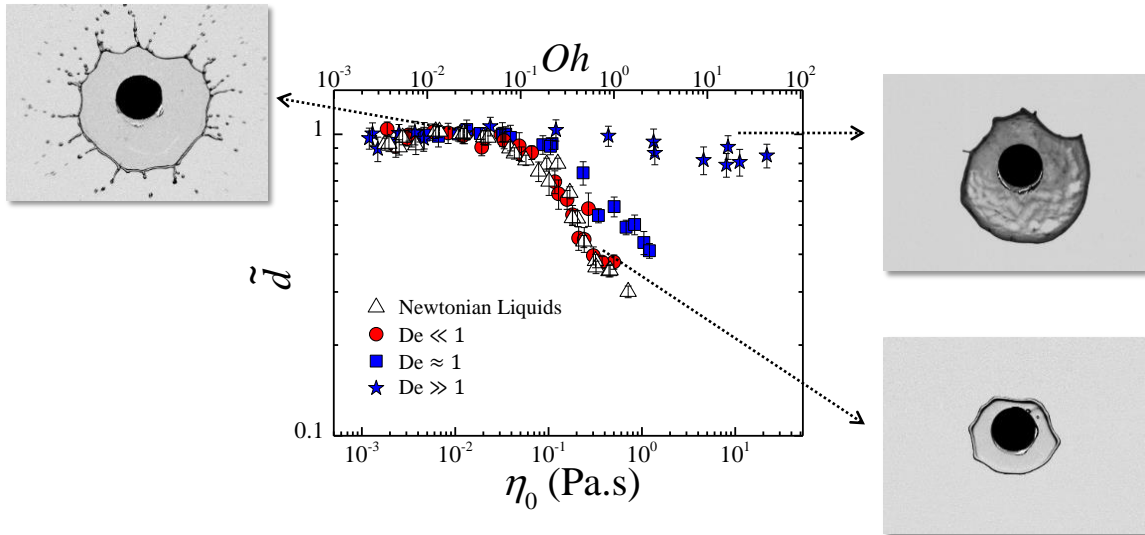


Figure A: Maximum diameter (normalized by its value at low viscosity), as a function of zero-shear viscosity (bottom x-axis) and Ohnesorge number (top x-axis). Images are shown for inviscid regime, viscous regime and viscoelastic regime ($De \gg 1$). The scale is set by the black solid discs of diameter 6 mm.

The results are reported in the publication, *Interplay between viscosity and elasticity in freely expanding liquid sheets*, S. Arora, C. Ligoure and L. Ramos, Phys. Rev. Fluids, 1, 083302, 2016 [Arora 2016].

To investigate the maximal deformation in more detail and also to elucidate the role of elasticity, we have designed a new and original set-up to avoid any viscous dissipation that occurs even when using a small solid target. We have used a solid substrate covered with liquid nitrogen (-196°C). On impacting the surface, a gaseous cushion of nitrogen forms between the drop or bead and the surface due to the evaporation of liquid

nitrogen. The cushion acts as a thermal insulator between the solid substrate and the sheet. The sheet while expanding or retracting is supported by the vapor layer. We have provided a universal scaling model for the maximal spread factor λ that depends on two elastic contributions: the surface elasticity due to surface tension that is quantified by the characteristic velocity $U_L = \sqrt{3\gamma/\rho d_o}$ and the bulk elasticity, quantified by the characteristic velocity $U_S = \sqrt{G_0/\rho}$. Here, γ is the surface tension, ρ is the density, d_o is the initial diameter of drop, and G_0 is the elastic modulus. A simple argument of energy conservation yields $\lambda \approx v_o/U^*$ with $U^* = \sqrt{U_L^2 + U_S^2}$ and v_o the impact velocity. This scaling also provides the asymptotic known behaviors for simple liquids ($\lambda \approx v_o/U_L$) and elastic solids ($\lambda \approx v_o/U_S$).

To check the validity of the theoretical model, we have performed experiments on a large variety of samples and have impacted drops and beads at different velocity in the range (1 m/s - 5 m/s). We have also used original ultra-soft beads with elastic modulus in the range (10 – 700 Pa) made of a loose permanently crosslinked polymer network. We have also used liquids with various surface tensions ($30 \leq \gamma \leq 72$ mN/m), and viscoelastic samples with $De \gg 1$. We find that the data for all the samples collapse on a single master curve when λ is plotted as a function of v_o/U^* and that λ varies linearly with v_o/U^* as predicted theoretically. Our data also demonstrates that for ultra-soft elastic beads, it is necessary to take surface elasticity into account in order to model their spreading. We have also shown that the time needed to reach the maximum deformation can be described by the same unified scaling prediction for liquids and solids as a function of the reduced impact velocity. Moreover, the dynamics of expansion and retraction of the sheets produced by the impact of a solid bead or a liquid drop can be understood in terms of simple harmonic motion without viscous dissipation and with a characteristic frequency of oscillation $\sim U^*/d_o$.

Interestingly, we have also shown that the impact experiments done on a small solid target using viscoelastic fluids (with $De \gg 1$) and viscous Newtonian fluids follow a similar scaling law once the impact velocity v_o is replaced by the effective velocity v_{eff} defined as above. Figure B shows the data acquired for liquid, viscous, viscoelastic, and elastic samples impacting on a small solid target as well as on a surface covered with liquid nitrogen. This master curve reveals a universal feature of all impacting materials.

In **perspective**, the present study can be extended to viscoelastic systems whose characteristic relaxation time is close to the experimental time scale in order to rationalize the subtle interplay between viscous dissipation and elasticity. Furthermore, more experiments would be required to better understand quantitatively the manifestations of cracks observed in sheets produced by impacting viscoelastic drops (with $De \gg 1$).

Filament stretching

We have investigated the uniaxial extensional deformation of self-assembled transient

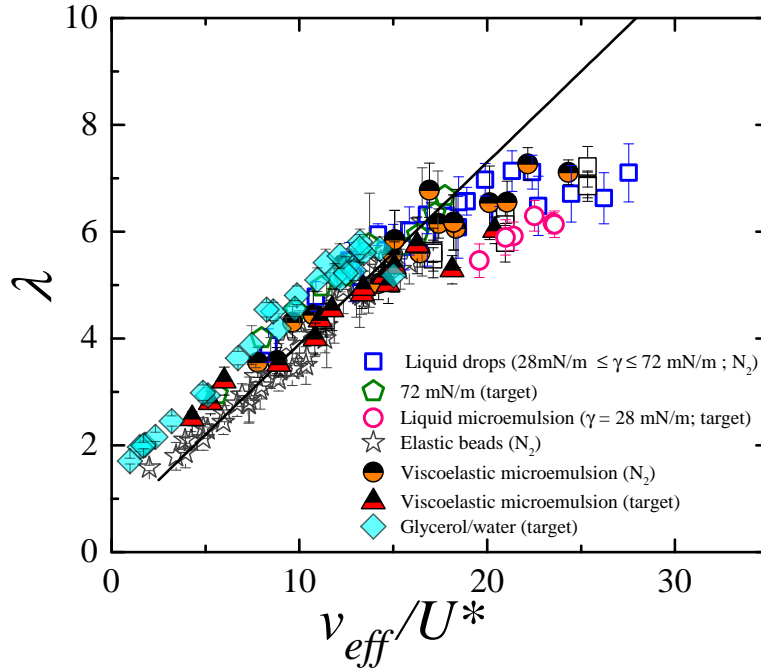


Figure B: Maximal spread factor λ as a function of v_{eff}/U^* where v_{eff} is the effective velocity with $v_{\text{eff}} = v_o$ for the experiments performed using inverse Leidenfrost effect and U^* is the velocity of generalized elastic deformations. The symbols are experimental data points for several classes of sample as indicated in the legend.

networks comprising surfactant wormlike micelles reversibly crosslinked by telechelic polymers using an extensional rheometer coupled to a fast camera. We have found that the networks break elastically without necking when deformed at a rate larger than the inverse of their lowest characteristic relaxation time. Figure C presents a state diagram of the viscoelastic filament under extensional stress. By varying the amount of copolymer, we have tuned the sample viscoelasticity and have found that samples with a dense network of elastic nodes break in the linear regime whereas samples with a loose network of nodes exhibit significantly strain hardening before fracturing. With the advantage of coupling the extensional rheometer with the fast camera, we have provided a direct evidence of a correlation between the non-linear elasticity and the shape of the crack profile close to the tip. We have rationalized the non-relevance of viscous dissipation effects. We have evidenced, for the first time for viscoelastic fluids, a departure from linear elasticity in the crack propagation as shown by a deviation from the parabolic shape at the crack tip. This amplitude of deviation increases with the decrease in node density. We have defined a non-dimensional length ℓ/\mathcal{L} , where ℓ is the amplitude of deviation from parabolic shape and $\mathcal{L} = V_c/\dot{\epsilon}$ is the characteristic length of fracture process with V_c the velocity of the crack tip and $\dot{\epsilon}$ the extensional rate. We have found that ℓ/\mathcal{L} varies as $(\chi - 1)^{1/3}$, $\chi = \sigma_c/E\varepsilon_c$ quantifies the non-linearity of the sample. Here σ_c is the extensional stress

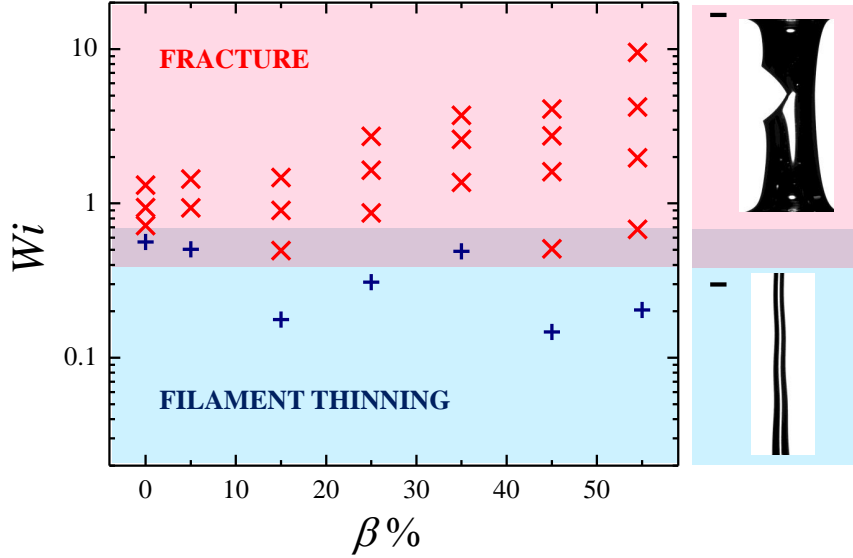


Figure C: Schematic state diagram of stretched viscoelastic filament, Weissenberg number, $Wi = \dot{\epsilon}\tau$ as a function of the amount of telechelic polymers β in the sample. Here $\dot{\epsilon}$ is the extensional rate and τ is the rheological relaxation time of the sample. The symbols correspond to the experimental configurations investigated. The two regimes, (i) continuous thinning at low Wi , and (ii) fracturing without necking at high Wi , are shown. Representative images of the filament corresponding to the two regimes are displayed. For the top image (crack) crack, $\beta = 25\%$ and $\dot{\epsilon} = 1\text{ s}^{-1}$, and for the bottom image (capillary thinning), $\beta = 0$ and $\dot{\epsilon} = 1\text{ s}^{-1}$. The scale bars are 1 mm.

at which fracture occurs, E is the Young's modulus, and ε_c is the strain at which fracture occurs.

The results are reported in the manuscript *Brittle fracture of polymer transient networks*, S. Arora, A. Shabbir, O. Hassager, C. Ligoure and L. Ramos, submitted to special issue of *J. Rheol.* 2017.

In **perspective**, first it would be interesting to elucidate the physical meaning of the simple scaling behavior of the characteristic length, $\ell/\mathcal{L} = (\chi - 1)^{1/3}$ that we have observed. We have focused on very long entangled wormlike micelles bridged by telechelic polymers. These samples are expected to align under stress (as shown in [Foyart 2016]). It would therefore be interesting to investigate how the structural rearrangement of these networks is coupled with the formation, shape and propagation of the cracks under extensional deformation. It would be also interesting to study other samples where the shape of the micelles varies (it can be tuned from spherical to rodlike to wormlike) in order to

study its influence on crack propagation. Indeed, previous experiments from our group have suggested that this factor controls the brittle-like to ductile-like fracture transition [Ramos 2011, Foyart 2016].

APPENDIX A

Chemical Compounds

Numerous chemical constituents are used for the sample preparation. All the chemicals are purchased from Sigma-Aldrich except the telechelic polymers which are home-synthesized by Ty Phou. Cetylpyridinium chloride (CpCl) is purified by successive recrystallisation in acetone and water before usage. The rest of the chemicals are used as received.

Table A.1 and A.2 summarize the chemicals used with their chemical formula and molecular weight.

Chemical Compound	Chemical Formula	Molar Mass (g mol ⁻¹)
Cetylpyridinium chloride (CpCl)	$C_{21}H_{38}ClN$	339.99
Sodium Salicylate (NaSal)	$C_7H_5NaO_3$	160.10
Sodium chloride (NaCl)	NaCl	58.44
Octanol	$C_8H_{17}OH$	130.23
Decane	$C_{10}H_{22}$	142.29
Telechelic Polymer C_{12}	$[CH_3(CH_2)_{11}]NHCO(OCH_2CH_2)_{795}O(CO)NH[(CH_2)_{11}CH_3]$	35,400
Telechelic Polymer C_{18}	$[CH_3(CH_2)_{17}]NHCO(OCH_2CH_2)_{795}O(CO)NH[(CH_2)_{17}CH_3]$	35,600
Telechelic Polymer C_{23}	$[CH_3(CH_2)_{22}]NHCO(OCH_2CH_2)_{239}O(CO)NH[(CH_2)_{22}CH_3]$	10,540

Table A.1: Chemical formula and molecular mass of the different compounds used for sample preparation.

Chemical Compound	Chemical Formula	Molar Mass (g mol^{-1})
Acrylamide	C_3H_5NO	71.08
N,N'-methylenebisacrylamide	$C_7H_{10}N_2O_2$	154.17
Sodium persulfate	$Na_2S_2O_8$	238.1
Tetramethylethylenediamine (TEMED)	$C_6H_{16}N_2$	116.21
poly(methylhydrosiloxane)	$(CH_3(H)SiO)_n$	-
Glycerol	$C_3H_8O_3$	92.09
Ethanol	C_2H_6O	46.08
Silicone Oil	$(Si(CH_3)_2O)_n$	-
Erioglaurine disodium salt	$C_{37}H_{34}N_2Na_2O_9S_3$	792.84

Table A.2: Chemical formula and molecular mass of the different compounds used for sample preparation.

Extensional Viscous Dissipation During the Expansion of a Liquid Sheet

We take into account the fact that dissipation occurs in the whole volume of the expanding sheet. This dissipation is due to the elongation stresses that develop in the liquid sheet during its expansion. We can write the energy dissipation at a scaling level as:

$$E_{\text{extension}} \simeq \int_0^{t_{\text{max}}} \int_V \sigma \dot{\epsilon} dV dt \quad (\text{B.1})$$

Here t_{max} is the time at the maximum expansion of the sheet, V_{drop} is the volume of the drop, σ is the extensional stress and $\dot{\epsilon}$ is the strain rate. The integration is over time and volume. σ can be written as $\eta_{be}\dot{\epsilon}$ where η_{be} is the biaxial extensional viscosity. Equation B.1 thus reads:

$$E_{\text{extension}} \simeq \int_0^{t_{\text{max}}} \int_V \eta_{be} \dot{\epsilon}^2 dV dt \quad (\text{B.2})$$

In the case of biaxial extensional flow, the strain rate is given by:

$$\dot{\epsilon} = \frac{1}{d} \frac{dd}{dt} \quad (\text{B.3})$$

here, d is the diameter of the sheet at time t and d_o is the initial diameter of the drop. Substituting for the strain rate using Equation B.3 in Equation B.2 and assuming volume conservation yields:

$$E_{\text{extension}} \simeq \eta_{be} V_{\text{drop}} \int_0^{t_{\text{max}}} \left(\frac{1}{d(t)} \right)^2 \left(\frac{dd}{dt} \right)^2 dt \quad (\text{B.4})$$

here, $V_{\text{drop}} = \frac{\pi d_o^3}{6}$ is the volume of the drop.

Using a simple scaling approach, at maximal expansion of a sheet d_{max} we can write:

$$\frac{dd}{dt} \approx \frac{d_{\text{max}} - d_o}{t_{\text{max}}} \quad \text{and} \quad d \approx \sqrt{d_{\text{max}} d_o} \quad (\text{B.5})$$

Using Equation B.5 in Equation B.4 we obtain:

$$E_{\text{extension}} \simeq \eta_{be} V_{\text{drop}} \left(\frac{1}{t_{\text{max}}} \right) \left(\frac{(d_{\text{max}} - d_o)^2}{d_{\text{max}} d_o} \right) \quad (\text{B.6})$$

Equation B.6 gives the expression for the dissipation energy due to biaxial extension flow in the expanding sheet.

An Alternative Model for the Maximal Spread Factor?

C. Clanet *et al* [Clanet 2004] have proposed an alternative model to predict the maximal spread factor $\lambda = d_{\max}/d_o$ (with d_{\max} the maximum diameter of expanded sheet and d_o the initial drop diameter) of a drop of low viscosity impacting a superhydrophobic surface. The model predicts $\lambda \sim We^{1/4}$ rather than the more classical result $\lambda \sim We^{1/2}$ derived from energy conservation approach. Here, Weber number $We = \rho v_o^2 d_o / \gamma$ with ρ the density, v_o the impact velocity and γ the surface tension.

The scaling law $\lambda \sim We^{1/4}$ has been shown to be in good quantitative agreement with experimental data [Josserand 2016]. The physical picture behind this scaling is that, during the impact, the drop is submitted to a high acceleration $a \sim v_o^2/d_o$ leading to an effective capillary length $l_c^* = \sqrt{\gamma/\rho a}$ much larger than the classical capillary length of a drop at rest in the gravitational field of earth $l_c = \sqrt{\gamma/\rho g}$. The shape of the sheet should result from a balance between the effective gravity and surface forces. Thus its thickness h necessarily scales as l_c^* . Using simple volume conservation, $d_o^3 \approx h d_{\max}^2$, gives $\lambda \sim We^{1/4}$.

Using a similar approach and assuming thickness scales as l_{ec}^* , we calculate an effective elasto-capillary length l_{ec}^* for soft elastic solids and liquids in the gravitational field a using Free energy F_E of the incompressible system in the limit of large deformation and then minimizing it with respect to l_{ec}^* :

$$d_{\max}^2 \rho a l_{ec}^{*2} + \gamma d_{\max}^2 + d_o^3 G_0 \frac{d_{\max}^2}{d_o^2} = F_E \quad (C.1)$$

Here G_0 is the elastic modulus and $a \sim v_o^2/d_o$ as in [Clanet 2004]. Using simple volume conservation $d_{\max}^2 l_{ec}^* \approx d_o^3$, we obtain:

$$\rho a l_{ec}^* d_o^3 + \gamma \frac{d_o^3}{l_{ec}^{*2}} + d_o^3 G_0 \frac{d_o^3}{d_o^2 l_{ec}^*} = F_E \quad (C.2)$$

Minimizing the above Equation C.2 with respect to l_{ec}^* , we obtain:

$$\rho a d_o^3 - \gamma \frac{d_o^3}{l_{ec}^{*2}} - G_0 \frac{d_o^4}{l_{ec}^{*2}} = 0 \quad (C.3)$$

By solving Equation C.3,

$$l_{ec}^* \approx \sqrt{\frac{\gamma}{\rho a} + \frac{G_0 d_o}{\rho a}} \quad (\text{C.4})$$

Using $a \sim v_o^2/d_o$ in Equation C.4,

$$l_{ec}^* \approx \sqrt{\frac{\gamma d_o}{\rho v_o^2} + \frac{G_0 d_o^2}{\rho v_o^2}} \quad (\text{C.5})$$

Writing Equation C.5 in terms of characteristic velocity, we obtain:

$$l_{ec}^* = \frac{d_o}{v_o} \sqrt{U_L^2 + U_S^2} \quad (\text{C.6})$$

with $U_S = \sqrt{\frac{G_0}{\rho}}$ as the velocity of transverse sound waves in an elastic medium [Kolsky 1963] and $U_L = \sqrt{\frac{3\gamma}{\rho d_o}}$ as the typical velocity of the free oscillations of a drop called Rayleigh velocity [Rayleigh 1879]. Thus Equation C.6 can be written as:

$$l_{ec}^* = \frac{d_o}{v_o} U^* \quad (\text{C.7})$$

with $U^* = \sqrt{U_L^2 + U_S^2}$ a typical velocity of the material for generalized elastic deformations.

Using simple volume conservation, $d_o^3 \approx l_{ec}^* d_{max}^2$ one obtains a simple scaling for the maximal spread factor,

$$\lambda \sim \sqrt{\frac{v_o}{U^*}} \quad (\text{C.8})$$

Equation C.8 shows that λ is predicted to vary linearly with $(v_o/U^*)^{1/2}$ rather than with v_o/U^* using an energy approach developed in Chapter 4 and 5.

We check the agreement of our experimental data with the prediction of Equation C.8. We first plot in Figure C.1a data for soft elastic beads impacting a non-interacting solid surface (using inverse Leidenfrost effect, Chapter 4). We find that all the data fairly collapse on a single curve. However, we find that the linear variation of λ with $(v_o/U^*)^{1/2}$ predicted by Equation C.8 only holds at small $\lambda \leq 3$. By contrast Figure C.1b clearly shows that λ varies linearly with (v_o/U^*) over the whole range of λ as demonstrated in Chapter 4.

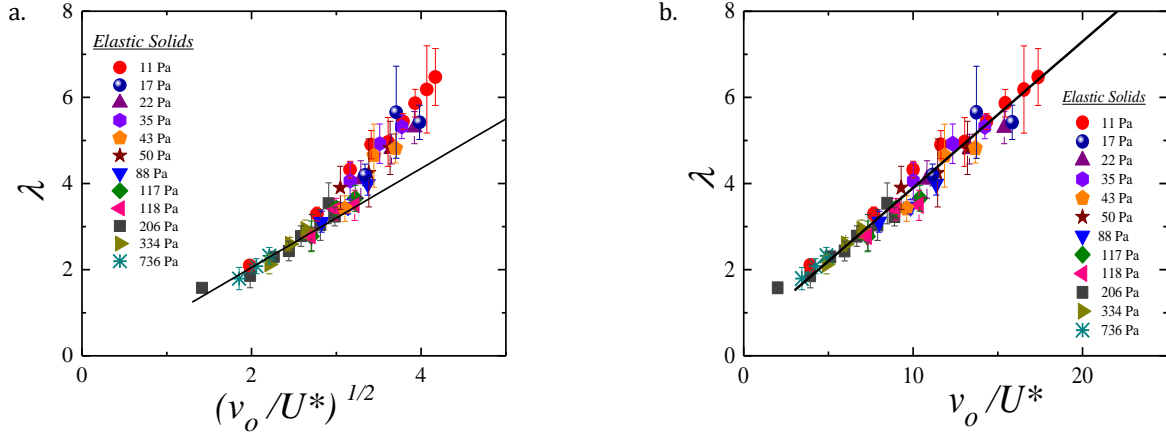


Figure C.1: Maximal spread factor λ as a function of (a) $(v_o/U^*)^{1/2}$ (b) (v_o/U^*) where v_o is the impact velocity and U^* is the velocity of generalized elastic deformations (Equation C.8). The solid symbols are experimental data points for elastic beads with different shear modulus as indicated in the legend. The solid lines are linear fits.

We also plot in Figure C.2a data obtained with the same experimental set-up for liquid drops, viscoelastic drops and elastic beads (Chapter 4 and 5). Similarly, we find that $(v_o/U^*)^{1/2}$ does not provide a nice account of the experimental data in contrast with the scaling derived from energy argument (Chapter 4 and 5) shown in Figure C.2b.

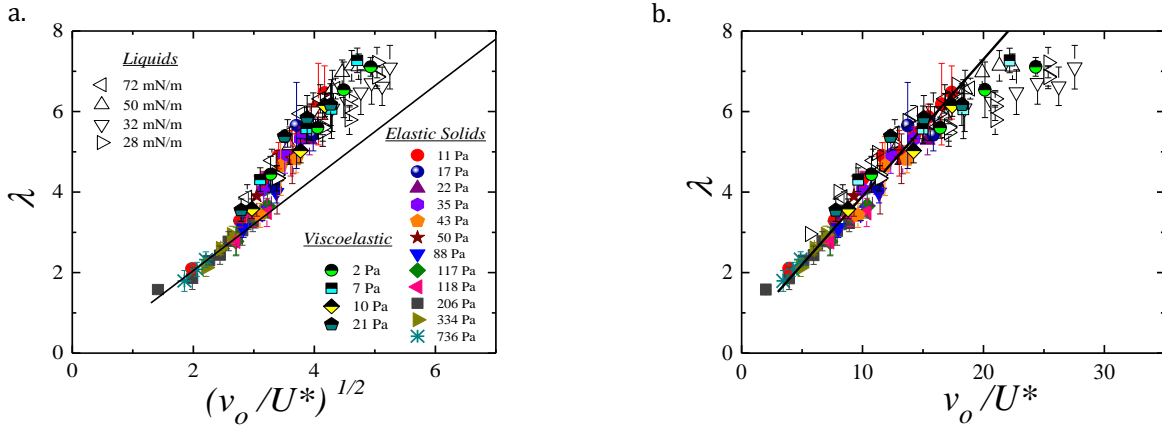


Figure C.2: Maximal spread factor λ as a function of (a) $(v_o/U^*)^{1/2}$ (b) (v_o/U^*) where v_o is the impact velocity and U^* is the velocity of generalized elastic deformations. The solid symbols are experimental data points for elastic beads with different shear modulus, empty symbols for liquids with different surface tension and semi black symbols for viscoelastic drops with different shear modulus as indicated in the legend. The solid lines are linear fits at small λ .

Bibliography

- [An 2012] S. M. An and S. Y. Lee. *Maximum spreading of a shear-thinning liquid drop impacting on dry solid surfaces*. *Experimental Thermal and Fluid Science*, vol. 38, pages 140–148, 2012. (Cited on page 9.)
- [Andrew 2017] M. Andrew, J. M. Yeomans and D. O. Pushkin. *A solvable model of axisymmetric and non-axisymmetric droplet bouncing*. *Soft Matter*, vol. 13, pages 985–994, 2017. (Cited on pages 78 and 79.)
- [Anna 2001] S. L. Anna and G. H. McKinley. *Elasto-capillary thinning and breakup of model elastic liquids*. *Journal of Rheology*, vol. 45, pages 115–138, 2001. (Cited on page 105.)
- [Antonini 2013] C. Antonini, I. Bernagozzi, S. Jung, D. Poulikakos and M. Marengo. *Water drops dancing on ice: How sublimation leads to drop rebound*. *Physical Review Letters*, vol. 111, pages 1–5, 2013. (Cited on pages 10, 11, 38, 66, 78 and 98.)
- [Arora 2016] S. Arora, C. Ligoure and L. Ramos. *Interplay between viscosity and elasticity in freely expanding liquid sheets*. *Physical Review Fluids*, vol. 1, page 083302, 2016. (Cited on pages 45, 98 and 116.)
- [Aziz 2000] S. D. Aziz and S. Chandra. *Impact, recoil and splashing of molten metal droplets*. *International Journal of Heat and Mass Transfer*, vol. 43, pages 2841–2857, 2000. (Cited on page 7.)
- [Barnes 1989] H. A. Barnes, J. F. Hutton and K. Walters. *An introduction to rheology*, volume 3. Elsevier, 1989. (Cited on page 32.)
- [Barnes 2000] H. A. Barnes. *A handbook of elementary rheology*. 2000. (Cited on page 28.)
- [Bartolo 2007] D. Bartolo, A. Boudaoud, G. Narcy and D. Bonn. *Dynamics of non-newtonian droplets*. *Physical Review Letters*, vol. 99, pages 1–4, 2007. (Cited on page 97.)
- [Bergeron 2000] V. Bergeron, D. Bonn, J. Y. Martin and L. Vovelle. *Controlling droplet deposition with polymer additives*. *Nature*, vol. 405, pages 772–775, 2000. (Cited on page 97.)
- [Berret 2001] J. F. Berret and Y. S  r  ro. *Evidence of Shear-Induced Fluid Fracture in Telechelic Polymer Networks*. *Physical Review Letters*, vol. 87, pages 048303–4, 2001. (Cited on page 14.)

- [Bertola 2009] V. Bertola. *An experimental study of bouncing Leidenfrost drops: comparison between Newtonian and viscoelastic liquids*. International Journal of Heat and Mass Transfer, vol. 52, pages 1786–1793, 2009. (Cited on page 97.)
- [Bertola 2015] V. Bertola and M. Wang. *Dynamic contact angle of dilute polymer solution drops impacting on a hydrophobic surface*. Colloids and Surfaces A: Physicochemical and Engineering Aspects, vol. 481, pages 600–608, 2015. (Cited on pages 9 and 98.)
- [Bhardwaj 2007] A. Bhardwaj, E. Miller and J. P. Rothstein. *Filament stretching and capillary breakup extensional rheometry measurements of viscoelastic wormlike micelle solutions*. Journal of Rheology, vol. 51, pages 693–719, 2007. (Cited on pages 2, 16, 105, 107 and 113.)
- [Biance 2003] A. L. Biance, C. Clanet and D. Quéré. *Leidenfrost drops*. Physics of Fluids, vol. 15, pages 1632–1637, 2003. (Cited on page 9.)
- [Biance 2006] A. L. Biance, F. Chevy, C. Clanet, G. Lagubeau and D. Quéré. *On the elasticity of an inertial liquid shock*. Journal of Fluid Mechanics, vol. 554, page 47, may 2006. (Cited on pages 9, 11, 74 and 79.)
- [Bird 2013] J. C. Bird, R. Dhiman, H. M. Kwon and K. K. Varanasi. *Reducing the contact time of a bouncing drop*. Nature, vol. 503, pages 385–388, 2013. (Cited on page 11.)
- [Bonfillon 1994] A. Bonfillon, F. Sicoli and D. Langevin. *Dynamic surface tension of ionic surfactant solutions*. Journal of Colloid and Interface Science, vol. 168, pages 497–504, 1994. (Cited on page 51.)
- [Buehler 2003] M. J. Buehler, F. F. Abraham and H. Gao. *Hyperelasticity governs dynamic fracture at a critical length scale*. Nature, vol. 426, pages 141–146, 2003. (Cited on page 111.)
- [Buehler 2006] M. J. Buehler and H. Gao. *Dynamical fracture instabilities due to local hyperelasticity at crack tips*. Nature, vol. 439, pages 307–310, 2006. (Cited on page 111.)
- [Cates 1987] M. E. Cates. *Reptation of living polymers: dynamics of entangled polymers in the presence of reversible chain-scission reactions*. Macromolecules, vol. 20, pages 2289–2296, 1987. (Cited on page 102.)
- [Chakrabarti 2013] A. Chakrabarti and M. K. Chaudhury. *Direct measurement of the surface tension of a soft elastic hydrogel: Exploration of elastocapillary instability in adhesion*. Langmuir, vol. 29, no. 23, pages 6926–6935, 2013. (Cited on page 66.)

- [Chandra 1991] S. Chandra and C. T. Avedisian. *On the collision of a droplet with a solid surface*. In Proceedings of the Royal Society of London A: Mathematical, Physical and Engineering Sciences, volume 432, pages 13–41. The Royal Society, 1991. (Cited on pages 7 and 9.)
- [Chen 2016] S. Chen and V. Bertola. *The impact of viscoplastic drops on a heated surface in the Leidenfrost regime*. Soft Matter, vol. 12, pages 7624–7631, 2016. (Cited on pages 12 and 98.)
- [Clanet 2001] C. Clanet. *Dynamics and stability of water bells*. Journal of Fluid Mechanics, vol. 430, pages 111–147, 2001. (Cited on page 53.)
- [Clanet 2002] C. Clanet and E. Villermaux. *Life of a smooth liquid sheet*. Journal of Fluid Mechanics, vol. 462, pages 307–340, 2002. (Cited on pages 53 and 56.)
- [Clanet 2004] C. Clanet, C. Béguin, D. Richard and D. Quéré. *Maximal deformation of an impacting drop*. Journal of Fluid Mechanics, vol. 517, pages 199–208, 2004. (Cited on pages 10, 12, 13, 52 and 125.)
- [Clasen 2012] C. Clasen, P. M. Phillips, L. Palangetic and J. Vermant. *Dispensing of rheologically complex fluids: the map of misery*. AIChE Journal, vol. 58, pages 3242–3255, 2012. (Cited on page 62.)
- [De Gennes 1988] P. G. De Gennes. *Fracture of a lightly crosslinked adhesive*. P. G. C. R. Hebd. Seances Acad. Sci., vol. 307, pages 1949–1953, 1988. (Cited on pages 60 and 111.)
- [De Gennes 1996] P. G. De Gennes. *Soft adhesives*. Langmuir, vol. 12, pages 4497–4500, 1996. (Cited on pages 18, 60 and 111.)
- [Deegan 2001] R. D. Deegan, P. J. Petersan, M. Marder and H. L. Swinney. *Oscillating fracture paths in rubber*. Physical Review Letters, vol. 88, page 014304, 2001. (Cited on pages 109, 110 and 112.)
- [Ducloué 2014] L. Ducloué, O. Pitois, J. Goyon, X. Chateau and G. Ovarlez. *Coupling of elasticity to capillarity in soft aerated materials*. Soft matter, vol. 10, pages 5093–5098, 2014. (Cited on page 79.)
- [Eggers 1997] J. Eggers. *Nonlinear dynamics and breakup of free-surface flows*. Reviews of Modern Physics, vol. 69, page 865, 1997. (Cited on page 105.)
- [Filali 1999] M. Filali, R. Aznar, M. Svenson, G. Porte and J. Appell. *Swollen Micelles Plus Hydrophobically Modified Hydrosoluble Polymers in Aqueous Solutions: Decoration versus Bridging. A Small Angle Neutron Scattering Study*. The Journal of Physical Chemistry B, vol. 103, pages 7293–7301, 1999. (Cited on page 20.)

- [Filali 2001] M. Filali, M. J. Ouazzani, E. Michel, R. Aznar, G. Porte and J. Appell. *Robust phase behavior of model transient networks*. The Journal Of Physical Chemistry B, vol. 105, pages 10528–10535, 2001. (Cited on page 21.)
- [Foyart 2013] G. Foyart, L. Ramos, S. Mora and C. Ligoure. *The fingering to fracturing transition in a transient gel*. Soft Matter, vol. 9, page 7775, 2013. (Cited on pages 15, 16, 61 and 98.)
- [Foyart 2016] G. Foyart, C. Ligoure, S. Mora and L. Ramos. *Rearrangement zone around a crack tip in a double self-assembled transient network*. ACS Macro Letters, vol. 5, pages 1080–1083, 2016. (Cited on pages 15, 119 and 120.)
- [Goldman 2012] T. Goldman, R. Harpaz, E. Bouchbinder and J. Fineberg. *Intrinsic nonlinear scale governs oscillations in rapid fracture*. Physical Review Letters, vol. 108, page 104303, 2012. (Cited on pages 110 and 112.)
- [Guémas 2012] M. Guémas, Á. G. Marín and D. Lohse. *Drop impact experiments of non-Newtonian liquids on micro-structured surfaces*. Soft Matter, vol. 8, pages 10725–10731, 2012. (Cited on pages 11 and 12.)
- [Hall 1969] R. S. Hall, S. J. Board, A. J. Clare, R. B. Duffey, T. S. Playle and D. H. Poole. *Inverse Leidenfrost Phenomenon*. Nature, vol. 224, pages 266–267, 1969. (Cited on page 38.)
- [Hartmann 1999] P. Hartmann, A. Collet and M. Viguiier. *Synthesis and characterization of model fluoroacylated poly(ethylene oxide)*. Journal of Fluorine Chemistry, vol. 95, pages 145–151, 1999. (Cited on page 20.)
- [Hertz 1881] H. Hertz. *On the contact of elastic solids*. Journal für die reine und angewandte Mathematik, vol. 92, page 110, 1881. (Cited on page 12.)
- [Hertz 1895] H. Hertz. *Gesammelte werke, vol. 1*. Johann Ambrosius Barth, Leipzig, vol. 155, 1895. (Cited on pages 35 and 66.)
- [Huang 2016a] Q. Huang, N. J. Alvarez, A. Shabbir and O. Hassager. *Multiple Cracks Propagate Simultaneously in Polymer Liquids in Tension*. Physical Review Letters, vol. 117, page 087801, 2016. (Cited on pages 2, 102 and 111.)
- [Huang 2016b] Q. Huang, M. Mangnus, N. J. Alvarez, R. Koopmans and O. Hassager. *A new look at extensional rheology of low-density polyethylene*. Rheologica Acta, vol. 55, pages 343–350, 2016. (Cited on pages 17, 18, 32 and 102.)
- [Huang 2017] Qian Huang and Ole Hassager. *Polymer liquids fracture like solids*. Soft Matter, vol. 13, pages 3470–3474, 2017. (Cited on pages 2 and 15.)

- [Huh 2015] H. K. Huh, S. Jung, K. W. Seo and S. J. Lee. *Role of polymer concentration and molecular weight on the rebounding behaviors of polymer solution droplet impacting on hydrophobic surfaces*. *Microfluidics and Nanofluidics*, vol. 18, pages 1221–1232, 2015. (Cited on page 98.)
- [Hui 2003] C. Y. Hui, A. Jagato, S. J. Bennison and J. D. Londono. *Crack blunting and the strength of soft elastic solids*. *Proceedings of the Royal Society A: Mathematical, Physical and Engineering Sciences*, vol. 459, pages 1489–1516, 2003. (Cited on page 111.)
- [Ignes-Mullol 1995] J. Ignés-Mullol, H. Zhao and J. V. Maher. *Velocity fluctuations of fracturelike disruptions of associating polymer solutions*. *Physical Review E*, vol. 51, page 1338, 1995. (Cited on page 15.)
- [Jagota 2012] A. Jagota, D. Paretkar and A. Ghatak. *Surface-tension-induced flattening of a nearly plane elastic solid*. *Physical Review E*, vol. 85, page 051602, 2012. (Cited on pages 71 and 79.)
- [Johnson 1987] K. L. Johnson. *Contact mechanics*. Cambridge university press, 1987. (Cited on pages 35 and 66.)
- [Joseph 2013] D. D. Joseph. *Fluid dynamics of viscoelastic liquids*, volume 84. Springer Science & Business Media, 2013. (Cited on page 69.)
- [Josserand 2016] C. Josserand and Sigurdur T. Thoroddsen. *Drop Impact on a Solid Surface*. *Annual Review of Fluid Mechanics*, vol. 48, pages annurev–fluid–122414–034401, 2016. (Cited on pages 1, 6, 8, 11 and 125.)
- [Khattab 2012] I. S. Khattab, F. Bandarkar, M. A. A. Fakhree and A. Jouyban. *Density, viscosity, and surface tension of water+ethanol mixtures from 293 to 323K*. *Korean Journal of Chemical Engineering*, vol. 29, pages 812–817, 2012. (Cited on page 26.)
- [Kolsky 1963] H. Kolsky. *Stress waves in solids*, volume 1098. Courier Corporation, 1963. (Cited on pages 69, 83 and 126.)
- [Lastakowski 2014] H. Lastakowski, F. Boyer, A. L. Bianco, C. Pirat and C. Ybert. *Bridging local to global dynamics of drop impact onto solid substrates*. *Journal of Fluid Mechanics*, vol. 747, pages 103–118, 2014. (Cited on pages 9 and 78.)
- [Leidenfrost 1756] J. G. Leidenfrost. *De aquae communis nonnullis qualitatibus tractatus*. Ovenius, 1756. (Cited on page 38.)
- [Lhuissier 2014] H. Lhuissier, B. Néel and L. Limat. *Viscoelasticity breaks the symmetry of impacting jets*. *Physical Review Letters*, vol. 113, page 194502, 2014. (Cited on page 99.)

- [Ligoure 2013] C. Ligoure and S. Mora. *Fractures in complex fluids: The case of transient networks*. *Rheologica Acta*, vol. 52, pages 91–114, feb 2013. (Cited on pages 2, 13, 19, 61 and 98.)
- [Liu 2014] T. Liu, R. Long and C. Y. Hui. *The energy release rate of a pressurized crack in soft elastic materials: effects of surface tension and large deformation*. *Soft Matter*, vol. 10, pages 7723–7729, 2014. (Cited on page 79.)
- [Livne 2007] A. Livne, O. Ben-David and J. Fineberg. *Oscillations in rapid fracture*. *Physical Review Letters*, vol. 98, page 124301, 2007. (Cited on page 109.)
- [Livne 2008] A. Livne, E. Bouchbinder and J. Fineberg. *Breakdown of linear elastic fracture mechanics near the tip of a rapid crack*. *Physical Review Letters*, vol. 101, page 264301, 2008. (Cited on pages 110 and 112.)
- [Luu 2009] L. H. Luu and Y. Forterre. *Drop impact of yield-stress fluids*. *Journal of Fluid Mechanics*, vol. 632, pages 301–327, 2009. (Cited on pages 9, 12, 79, 83 and 98.)
- [Luu 2013] L. H. Luu and Y. Forterre. *Giant drag reduction in complex fluid drops on rough hydrophobic surfaces*. *Physical Review Letters*, vol. 110, pages 1–5, 2013. (Cited on pages 9, 12, 13, 79, 83 and 98.)
- [Macosko 1994] C. W. Macosko and R. G. Larson. *Rheology: principles, measurements, and applications*. 1994. (Cited on page 57.)
- [Malkin 1997] A. Y. Malkin and C. J. S. Petrie. *Some conditions for rupture of polymer liquids in extension*. *Journal of Rheology*, vol. 41, pages 1–25, 1997. (Cited on page 105.)
- [Marín 2013] J. M. R. Marín, J. K. Huusom, N. J. Alvarez, Q. Huang, H. K. Rasmussen, A. Bach, A. L. Skov and O. Hassager. *A control scheme for filament stretching rheometers with application to polymer melts*. *Journal of Non-Newtonian Fluid Mechanics*, vol. 194, pages 14–22, 2013. (Cited on pages 32 and 33.)
- [Marmottant 2000] P. Marmottant, E. Villermaux and C. Clanet. *Transient Surface Tension of an Expanding Liquid Sheet*. *Journal of Colloid and Interface Science*, vol. 230, pages 29–40, 2000. (Cited on page 52.)
- [McKinley 2002] G. H. McKinley and T. Sridhar. *Filament-stretching rheometry of complex fluids*. *Annual Review of Fluid Mechanics*, vol. 34, pages 375–415, 2002. (Cited on page 2.)
- [Menter 2000] P. Menter. *Acrylamide Polymerization—A Practical Approach*. *Bio-Rad Tech Note*, vol. 1156, 2000. (Cited on page 24.)

- [Michel 2000] E. Michel, M. Filali, R. Aznar, G. Porte and J. Appell. *Percolation in a model transient network: Rheology and dynamic light scattering*. Langmuir, vol. 16, pages 8702–8711, 2000. (Cited on pages 21 and 46.)
- [Miller 2005] E. Miller, B. Gibson, E. McWilliams and J. P. Rothstein. *Collision of viscoelastic jets and the formation of fluid webs*. Applied Physics Letters, vol. 87, pages 50–52, 2005. (Cited on pages 60 and 98.)
- [Molino 1999] F. Molino, J. Appell, M. Filali, E. Michel, G. Porte, S. Mora and E. Sunyer. *A transient network of telechelic polymers and microspheres : structure and rheology*. Journal of Physics: Condensed Matter, vol. 12, page 9, 1999. (Cited on pages 13 and 20.)
- [Mora 2010a] S. Mora and M. Manna. *Saffman-Taylor instability of viscoelastic fluids: From viscous fingering to elastic fractures*. Physical Review E, vol. 81, page 026305, 2010. (Cited on pages 15 and 61.)
- [Mora 2010b] S. Mora, T. Phou, J. M. Fromental, L. M. Pismen and Y. Pomeau. *Capillarity driven instability of a soft solid*. Physical review letters, vol. 105, page 214301, 2010. (Cited on pages 71 and 79.)
- [Mora 2012] S. Mora and M. Manna. *From viscous fingering to elastic instabilities*. Journal of Non-Newtonian Fluid Mechanics, vol. 173, pages 30–39, 2012. (Cited on page 15.)
- [Morishita 2016] Y. Morishita, K. Tsunoda and K. Urayama. *Velocity transition in the crack growth dynamics of filled elastomers: Contributions of nonlinear viscoelasticity*. Physical Review E, vol. 93, page 043001, 2016. (Cited on pages 110 and 112.)
- [Mundo 1995] C. Mundo, M. Sommerfeld and C. Tropea. *Droplet-wall collisions: Experimental studies of the deformation and breakup process*. International Journal of Multiphase Flow, vol. 21, pages 151–173, 1995. (Cited on pages 73 and 85.)
- [Nakaya-Yaegashi 2008] K. Nakaya-Yaegashi, L. Ramos, H. Tabuteau and C. Ligoure. *Linear viscoelasticity of entangled wormlike micelles bridged by telechelic polymers: an experimental model for a double transient network*. Journal of Rheology, vol. 52, pages 359–377, 2008. (Cited on pages 30 and 102.)
- [Ogden 1997] R. W. Ogden. *Non-linear elastic deformations*. Courier Corporation, 1997. (Cited on page 68.)
- [Okumura 2003] Ko Okumura, Frédéric Chevy, Denis Richard, David Quéré and Christophe Clanet. *Water spring: A model for bouncing drops*. Europhysics Letters, vol. 62, page 237, 2003. (Cited on pages 9, 11 and 79.)

- [Pasandideh-Fard 1996] M. Pasandideh-Fard, Y. M. Qiao, S. Chandra and J. Mostaghimi. *Capillary effects during droplet impact on a solid surface*. *Physics of Fluids*, vol. 8, pages 650–659, 1996. (Cited on pages 7 and 8.)
- [producers association 1963] Glycerine producers association *et al.* *Physical properties of glycerine and its solutions*. Glycerine Producers Association, 1963. (Cited on page 26.)
- [Ramos 2011] L. Ramos, A. Laperrousaz, P. Dieudonné and C. Ligoure. *Structural signature of a brittle-to-ductile transition in self-assembled networks*. *Physical Review Letters*, vol. 107, pages 1–5, 2011. (Cited on pages 23 and 120.)
- [Rayleigh 1879] L. Rayleigh. *On the Capillary Phenomena of Jets*. *Proceedings of the Royal Society of London*, vol. 29, pages 71–97, 1879. (Cited on pages 70, 84 and 126.)
- [Rehage 1988] H. Rehage and H. Hoffman. *Rheological Properties of Viscoelastic Surfactant Systems*. *Journal of Physical Chemistry*, vol. 92, pages 4712–4719, 1988. (Cited on page 22.)
- [Rehage 1991] H. Rehage and H. Hoffmann. *Viscoelastic surfactant solutions: model systems for rheological research*. *Molecular Physics*, vol. 74, pages 933–973, dec 1991. (Cited on page 22.)
- [Rein 1993] M. Rein. *Phenomena of liquid drop impact on solid and liquid surfaces*. *Fluid Dynamics Research*, vol. 12, pages 61–93, 1993. (Cited on page 7.)
- [Rein 2002] M. Rein. *Interactions between drops and hot surfaces*. In *Drop-Surface Interactions*, pages 185–217. Springer, 2002. (Cited on page 9.)
- [Richard 2000] D. Richard and D. Quéré. *Bouncing water drops*. *Europhysics Letters*, vol. 50, page 769, 2000. (Cited on page 9.)
- [Richard 2002] D. Richard, C. Clanet and D. Quéré. *Contact time of a bouncing drop*. *Nature*, vol. 417, page 811, 2002. (Cited on pages 9, 11, 71 and 79.)
- [Rillaerts 1982] E. Rillaerts and P. Joos. *Rate of demicellization from the dynamic surface tensions of micellar solutions*. *The Journal of Physical Chemistry*, vol. 311, pages 3471–3478, 1982. (Cited on page 52.)
- [Rioboo 2001] R. Rioboo, C. Tropea and M. Marengo. *Outcomes from a drop impact on solid surfaces*. *Atomization and Sprays*, vol. 11, 2001. (Cited on pages 6, 7, 73 and 85.)
- [Roisman 2009] I. V. Roisman. *Inertia dominated drop collisions. II. An analytical solution of the Navier–Stokes equations for a spreading viscous film*. *Physics of Fluids*, vol. 21, page 052104, 2009. (Cited on pages 8 and 53.)

- [Rothstein 2003] J. P. Rothstein. *Transient extensional rheology of wormlike micelle solutions*. Journal of Rheology, vol. 47, pages 1227–1247, 2003. (Cited on pages 2, 16, 107 and 113.)
- [Rozhkov] A. Rozhkov, B. Prunet-Foch and M. Vignes-Adler. *Impact of drops of surfactant solutions on small targets*. In Proceedings of the Royal Society of London A: Mathematical, Physical and Engineering Sciences, volume 466. (Cited on page 52.)
- [Rozhkov 2002] A. Rozhkov, B. Prunet-Foch and M. Vignes-Adler. *Impact of water drops on small targets*. Physics of Fluids, vol. 14, pages 3485–3501, 2002. (Cited on pages 8 and 36.)
- [Rozhkov 2003] A. Rozhkov, B. Prunet-Foch and M. Vignes-Adler. *Impact of drops of polymer solutions on small targets*. Physics of Fluids, vol. 15, no. 7, pages 2006–2019, 2003. (Cited on page 97.)
- [Rozhkov 2004] A. Rozhkov, B. Prunet-Foch and M. Vignes-Adler. *Dynamics of a liquid lamella resulting from the impact of a water drop on a small target*. In Proceedings of the Royal Society of London A: Mathematical, Physical and Engineering Sciences, volume 460, pages 2681–2704. The Royal Society, 2004. (Cited on pages 8 and 9.)
- [Saffman 1958] P. G. Saffman and G. Taylor. *The penetration of a fluid into a porous medium or Hele-Shaw cell containing a more viscous liquid*. In Proceedings of the Royal Society of London A: Mathematical, Physical and Engineering Sciences, volume 245, pages 312–329. The Royal Society, 1958. (Cited on page 15.)
- [Saulnier 2004] F. Saulnier, T. Ondarçuhu, A. Aradian and E. Raphael. *Adhesion between a viscoelastic material and a solid surface*. Macromolecules, vol. 37, pages 1067–1075, 2004. (Cited on pages 18, 60 and 111.)
- [Savart 1833] F. Savart. *Mémoire sur la constitution des veines liquides lancées par des orifices circulaires en mince paroi*. Annales de Chimie et de Physique, vol. 53, page 1833, 1833. (Cited on page 8.)
- [Scheller 1995] Brian L Scheller and Douglas W Bousfield. *Newtonian drop impact with a solid surface*. AIChE Journal, vol. 41, pages 1357–1367, 1995. (Cited on page 8.)
- [Shabbir 2016] A. Shabbir, Q. Huang, Q. Chen, R. H. Colby, N. J. Alvarez and O. Hassager. *Brittle fracture in associative polymers: the case of ionomer melts*. Soft Matter, vol. 4, pages 1166–1169, 2016. (Cited on pages 18 and 33.)
- [Sheely 1932] M. L. Sheely. *Glycerol Viscosity Tables*. Industrial & Engineering Chemistry, vol. 24, pages 1060–1064, 1932. (Cited on page 26.)

- [Skrzeszewska 2010] P. J. Skrzyszewska, J. Sprakel, F. A. de Wolf, R. Fokkink, Martien A. Cohen S. and J. van der Gucht. *Fracture and Self-Healing in a Well-Defined Self-Assembled Polymer Network*. *Macromolecules*, vol. 43, pages 3542–3548, 2010. (Cited on page 14.)
- [Smith 2010] M. I. Smith and V. Bertola. *Effect of polymer additives on the wetting of impacting droplets*. *Physical Review Letters*, vol. 104, page 154502, 2010. (Cited on page 98.)
- [Smith 2014] J. S. Smith M. I. and Sharp. *Origin of contact line forces during the retraction of dilute polymer solution drops*. *Langmuir*, vol. 30, pages 5455–5459, 2014. (Cited on page 98.)
- [Tabuteau 2008] H. Tabuteau, S. Mora, L. Ramos, G. Porte and C. Ligoure. *Ductility versus Brittleness in Self-Assembled Transient Networks*. *Progress of Theoretical Physics Supplement*, vol. 175, pages 47–53, 2008. (Cited on page 98.)
- [Tabuteau 2009] H. Tabuteau, S. Mora, G. Porte, M. Abkarian and C. Ligoure. *Microscopic mechanisms of the brittleness of viscoelastic fluids*. *Physical Review Letters*, vol. 102, pages 1–4, 2009. (Cited on pages 13, 14, 17, 46, 61, 98 and 105.)
- [Tabuteau 2011] H. Tabuteau, S. Mora, M. Ciccotti, C.-Y. Hui and C. Ligoure. *Propagation of a brittle fracture in a viscoelastic fluid*. *Soft Matter*, vol. 7, page 9474, 2011. (Cited on pages 17, 46, 60, 110 and 112.)
- [Tanaka 2003] Y. Tanaka, Y. Yamazaki and K. Okumura. *Bouncing gel balls: impact of soft gels onto rigid surface*. *Europhysics Letters*, vol. 63, page 7, 2003. (Cited on pages 12, 68, 71 and 79.)
- [Tanaka 2005] Y. Tanaka. *Impact of gel balls beyond the Hertzian regime*. *The European Physical Journal E - Soft Matter*, vol. 18, pages 95–103, 2005. (Cited on pages 12, 68 and 79.)
- [Thompson 2007] J. C. Thompson and J. P. Rothstein. *The atomization of viscoelastic fluids in flat-fan and hollow-cone spray nozzles*. *Journal of Non-Newtonian Fluid Mechanics*, vol. 147, pages 11–22, 2007. (Cited on page 98.)
- [Thoroddsen 2008] S. T. Thoroddsen, T. G. Etoh and K. Takehara. *High-speed imaging of drops and bubbles*. *Annual Review of Fluid Mechanics*, vol. 40, pages 257–285, 2008. (Cited on page 6.)
- [Tixier 2010] T. Tixier, H. Tabuteau, A. Carrière, L. Ramos and C. Ligoure. *Transition from “brittle” to “ductile” rheological behavior by tuning the morphology of self-assembled networks*. *Soft Matter*, vol. 6, pages 2699–2707, 2010. (Cited on pages 23, 46 and 48.)

- [Tran 2012] T. Tran, H. J. J. Staat, A. Prosperetti, C. Sun and D. Lohse. *Drop impact on superheated surfaces*. Physical Review Letters, vol. 108, pages 1–5, 2012. (Cited on pages 9, 11, 66 and 78.)
- [Tripathi 2006] A. Tripathi, K. C. Tam and G. H. McKinley. *Rheology and dynamics of associative polymers in shear and extension: theory and experiments*. Macromolecules, vol. 39, pages 1981–1999, 2006. (Cited on pages 2, 15, 16 and 105.)
- [Tsai 2011] P. Tsai, M. H. W. Hendrix, R. R. M. Dijkstra, L. Shui and D. Lohse. *Microscopic structure influencing macroscopic splash at high Weber number*. Soft Matter, vol. 7, pages 11325–11333, 2011. (Cited on page 11.)
- [Vernay 2015a] C. Vernay. *Destabilization of liquid sheets of dilute emulsions*. Theses, Université de Montpellier, October 2015. (Cited on page 38.)
- [Vernay 2015b] C. Vernay, L. Ramos and C. Ligoure. *Bursting of Dilute Emulsion-Based Liquid Sheets Driven by a Marangoni Effect*. Physical Review Letters, vol. 115, pages 2–6, 2015. (Cited on page 53.)
- [Vernay 2015c] C. Vernay, L. Ramos and C. Ligoure. *Free radially expanding liquid sheet in air: time-and space-resolved measurement of the thickness field*. Journal of Fluid Mechanics, vol. 764, pages 428–444, 2015. (Cited on pages 8, 52, 53, 91 and 96.)
- [Villermaux 2011] E. Villermaux and B. Bossa. *Drop fragmentation on impact*. Journal of Fluid Mechanics, vol. 668, pages 412–435, 2011. (Cited on pages 8, 36, 52 and 53.)
- [Villermaux 2013] E. Villermaux, V. Pistre and H. Lhuissier. *The viscous Savart sheet*. Journal of Fluid Mechanics, vol. 730, page 607, 2013. (Cited on page 53.)
- [Vlad 1999] D. H. Vlad, J. Ignes-Mullol and J. V. Maher. *Velocity-jump instabilities in Hele-Shaw flow of associating polymer solutions*. Physical Review E, vol. 60, page 4423, 1999. (Cited on page 15.)
- [Wachters 1966] L. H. J. Wachters and N. A. J. Westerling. *The heat transfer from a hot wall to impinging water drops in the spheroidal state*. Chemical Engineering Science, vol. 21, pages 1047–1056, 1966. (Cited on page 11.)
- [Walker 1996] L. M. Walker, P. Moldenaers and J. F. Berret. *Macroscopic response of wormlike micelles to elongational flow*. Langmuir, vol. 12, pages 6309–6314, 1996. (Cited on page 113.)
- [Worthington 1908] A. M. Worthington. *A Study of Splashes*. Longmans, Green and Co, London, 1908. (Cited on pages 1 and 6.)

-
- [Yarin 2006] A.L. Yarin. *Drop Impact Dynamics: Splashing, Spreading, Receding, Bouncing...* Annual Review of Fluid Mechanics, vol. 38, pages 159–192, 2006. (Cited on pages 1, 6 and 53.)
- [Zang 2013] D. Zang, X. Wang, X. Geng, Y. Zhang and Y. Chen. *Impact dynamics of droplets with silica nanoparticles and polymer additives*. Soft Matter, vol. 9, pages 394–400, 2013. (Cited on page 98.)
- [Zhao 1993] H. Zhao and J. V. Maher. *Associating-Polymer Effects in a Hele-Shaw Experiment*. Physical Review E, vol. 47, pages 4278–4283, 1993. (Cited on pages 15 and 16.)

Drops, beads and filaments of gels under extreme deformations

Abstract: In this thesis, we investigate the behavior of various gels subjected to extreme mechanical stresses. Two kinds of gels have been explored: self-assembled transient gels and permanently crosslinked gels. Two different techniques are used to impose large extensional deformations. In one class of experiments, we study the dynamics of freely expanding sheets produced by impacting a drop or bead on solid surfaces in minimal dissipation conditions. This can be achieved either by impacting the drop or bead on a small solid target or on repellent surfaces. Upon impact, the drop or bead is transformed into a thin sheet that expands and retracts due to elasticity. The drops comprise of Newtonian viscous fluids with a zero shear viscosity η_0 in the range 1 – 1000 mPa.s, viscoelastic fluids whose linear viscoelastic behavior can be accounted by Maxwell model with a characteristic elastic modulus G_0 in the range 2 – 600 Pa and relaxation time τ in the range 1 – 400 ms and the polymeric gel beads whose elastic modulus lies in the range 10 – 700 Pa.

In the case of sheets produced by impacting a drop on a small solid target, we show that for viscoelastic fluids with τ smaller than the typical lifetime of the sheet ($\tau_{\text{life}} \sim 10$ ms), the dynamics of viscoelastic sheets is similar to that of Newtonian viscous liquids with equal zero-shear viscosity. The maximal expansion of the sheet, d_{max} , decreases with $\eta_0 = G_0\tau$ and can be quantitatively accounted by a simple model based on an energy balance between inertia, surface tension and viscous shear dissipation on the solid target. By using a semi-empirical approach, we quantitatively account for the dependence of maximum spreading of the sheet with the sample viscosity and show that the dissipation on the small target can be accounted by measuring an effective velocity of the expanding sheet at short time scale. On the other hand, when $\tau > \tau_{\text{life}}$ the behavior differs drastically. The sheet expansion is strongly enhanced as compared to that of viscous samples with comparable zero-shear viscosity.

We show that the shear dissipation can be substantially eliminated by performing drop impact experiments on a solid surface covered with a thin layer of liquid nitrogen, thanks to inverse Leidenfrost effect. We performed experiments using elastic beads of various elastic moduli, liquid drops of various surface tensions and viscoelastic fluids with $\tau > \tau_{\text{life}}$. The experiments reveal a universal scaling behavior of the maximum expansion with the impact velocity and the dynamics of the system mimics the dynamics of a conventional spring-mass system. Furthermore, we show that in the case of viscoelastic or Newtonian viscous drops impacting the solid target, similar scaling can be used once the viscous dissipation is accounted by replacing the impact velocity with the effective velocity that can be measured. Another fascinating behavior observed in the case of viscoelastic fluids with $\tau > \tau_{\text{life}}$ is a heterogeneous expansion of the sheet with the occurrence of cracks, revealing the elastic nature of the viscoelastic fluid.

In another class of experiments, we study the fracture of reversible double transient networks by coupling extensional rheology to fast imaging of the stretching filament. We provide a state diagram that delineates the regime of fracture without necking of the filament from the regime where no fracture or break-up has been observed. We show that filaments fracture when stretched at a rate larger than the inverse of the slowest relaxation time of the networks. We quantitatively demonstrate that dissipation processes are not relevant in our experimental conditions and that, depending on the density of nodes in the networks, fracture occurs in the linear viscoelastic regime or in a non-linear regime preceded by a considerable strain hardening. In addition, analysis of the crack opening profiles indicates deviations from a parabolic shape close to the crack tip for weakly connected networks. We demonstrate a direct correlation between the amplitude of the deviation from the parabolic shape and the amount of non-linear viscoelasticity.

Keywords: drop impact, liquid sheet, maximal expansion, viscoelastic fluids, Newtonian fluids, elastic solids, elasto-capillarity, filament stretching, fracture, extensional rheometry

Gouttes, perles et filaments de gel sous déformations extrêmes

Résumé: Nous étudions le comportement de gels soumis à des contraintes mécaniques extrêmes. Deux types de gels (transitoires auto-assemblés et réticulés permanents) et deux techniques pour imposer de grandes déformations extensionnelles sont explorés.

D'une part, nous étudions la déformation biaxiale de nappes libres produites par impact d'une goutte ou perle sur une surface solide dans des conditions de dissipation énergétique minimisée, réalisée par impact soit sur une petite cible solide, soit sur une surface répulsive. Lors de l'impact, la goutte ou perle est transformée en une nappe mince qui s'étend puis se rétracte sous l'action de forces de rappel élastiques. Les gouttes sont constituées de fluides Newtoniens de viscosité η_0 entre 1 et 1000 mPa.s, et de fluides viscoélastiques de Maxwell avec un module élastique de cisaillement G_0 entre 2 et 600 Pa et un temps de relaxation τ entre 1 et 400 ms. Les perles sont constituées de gels polymériques réticulés avec un module élastique de cisaillement entre 10 et 700 Pa. Lors de l'impact d'une goutte sur une petite cible solide, nous montrons que, pour les fluides viscoélastiques avec τ inférieur à la durée de vie typique de la nappe ($\tau_{\text{life}} \sim 10$ ms), la dynamique de la nappe est similaire à celle d'un liquide visqueux Newtonien de même viscosité. L'expansion maximale de la nappe, d_{max} , décroît avec $\eta_0 = G_0\tau$ et peut être reproduite par un modèle simple basé sur un bilan énergétique entre l'énergie cinétique de la goutte à l'impact, l'énergie de surface et la dissipation visqueuse de cisaillement. Grâce à une approche semi-empirique, nous reproduisons quantitativement la dépendance de d_{max} avec la viscosité de l'échantillon et montrons que la dissipation sur la petite cible peut être prise en compte en mesurant une vitesse effective de la nappe aux temps courts, en sortie de cible. Par contre, lorsque $\tau > \tau_{\text{life}}$, le comportement diffère drastiquement et l'expansion des nappes augmente fortement par rapport à celle d'échantillons visqueux de viscosité comparable. En outre, nous montrons que la dissipation due au cisaillement peut être sensiblement éliminée en utilisant comme surface d'impact une surface solide recouverte d'une mince couche d'azote liquide, grâce à un effet de Leidenfrost inverse. Des expériences conduites avec des perles élastiques ultra molles de module élastique variable, des gouttes liquides de tension superficielle variable et des fluides de Maxwell avec un module de cisaillement très faible et $\tau > \tau_{\text{life}}$, révèlent un comportement universel pour l'expansion maximale de la nappe et la durée d'expansion avec la vitesse d'impact. Nous démontrons que la dynamique d'expansion de la nappe peut être simplement modélisée par la dynamique d'un oscillateur harmonique linéaire unidimensionnel. En outre, nous montrons que, dans le cas de gouttes visqueuses qui impactent une petite cible solide, une description similaire peut être utilisée une fois que la dissipation visqueuse est prise en compte en remplaçant la vitesse d'impact par la vitesse effective de la nappe que nous mesurons. Un autre comportement fascinant des fluides viscoélastiques avec $\tau > \tau_{\text{life}}$ est une expansion hétérogène de la nappe avec l'apparition d'instabilités de type fissures, associées à la nature élastique du fluide.

D'autre part, nous étudions la déformation uniaxiale et la fracture de filaments de doubles réseaux transitoires en couplant rhéométrie extensionnelle et imagerie rapide des filaments étirés. Nous établissons un diagramme d'état qui sépare les régimes de fracture et d'amincissement progressif continu du filament. Les filaments se fracturent lorsqu'ils sont étirés à un taux supérieur à l'inverse du temps de relaxation du plus lent des deux réseaux. Nous démontrons quantitativement que les processus de dissipation ne sont pas pertinents dans nos conditions expérimentales, et que, suivant la densité des nœuds dans les réseaux, la rupture se produit dans un régime viscoélastique linéaire, ou non-linéaire et précédé d'une augmentation considérable de la viscosité extensionnelle. L'analyse des profils d'ouverture des fissures indique des écarts par rapport à une forme parabolique de la pointe de fissure, caractéristique d'une fracture fragile en régime linéaire, pour des réseaux faiblement connectés. Nous montrons une corrélation directe entre l'amplitude de la déviation par rapport à la forme parabolique et le caractère non linéaire de la déformation viscoélastique.

Mots-clés: nappe liquide, impact de goutte, expansion maximale, fluides viscoélastiques, fluides Newtoniens, solides élastiques, élasto-capillarité, étirage de filaments, fracture, rhéométrie extensionnelle